DIAGNOSIS OF MULTI-STAGE FRACTURE STIMULATION IN HORIZONTAL WELLS BY DOWNHOLE TEMPERATURE MEASUREMENTS

A Dissertation

by

JINGYUAN CUI

Submitted to the Office of Graduate and Professional Studies of
Texas A&M University
in partial fulfillment of the requirements for the degree of

DOCTOR OF PHILOSOPHY

Chair of Committee,	Ding Zhu
Committee Members,	A. Daniel Hill
	Eduardo Gildin
	Zhengdong. Cheng
Head of Department,	A. Daniel Hill

December 2015

Major Subject: Petroleum Engineering

ABSTRACT

Fractured well performance diagnosis for a multiple-stage fractured horizontal well is critical to understand and improve fracture stimulation design. Temperature distribution data (by production logging tools or fiber-optic sensors) is one of the valuable information for performance diagnosis. However, until today quantitative interpretation of dynamic temperature data is still challenging and requires in-depth mathematical modeling of heat and mass transfer during production in a complex flow system.

The interpretation models developed to translate temperature data to flow conditions can be fully numerical-based simulations or analytical/semi-analytical approaches. With reasonable assumptions analytical/semi-analytical models are more suitable for real-time field applications. This dissertation presents the applications of using a coupled semi-analytical fracture model and a wellbore model to predict the temperature and pressure behavior in multiple-fractured horizontal wells in unconventional reservoirs during production. The thermal model calculated heat transfer in the fracture/reservoir/wellbore system considering subtle temperature changes caused by the Joule-Thomson cooling effect. The results showed that the wellbore fluid temperature behavior is sensitive to the flow condition, and can be used to estimate fracture initiation points, number of created fractures and flow profile along the horizontal wellbore.

This dissertation discusses the characteristics of transient temperature behaviors corresponding to different wellbore constraints, and also the fracture volume which influence the flow rate/temperature distribution along a fractured horizontal wellbore. The

temperature drop when gas entering the wellbore is more obvious at the toe and is weaken towards the heel with the uniform inflow rate distribution due to the fluid mixing inside the wellbore. Field cases are presented to illustrate the application of using the temperature model to understand the fracture/flow distribution. The estimation of flow rate distribution from the temperature model is compared to the interpretation of flow by production logging tools (PLT) and commercial software. The flow profile from the temperature model presents consistent trend with PLT measurement. It is more sensitive to the fluid entries (fracture locations) and less sensitive to the influence of flow regime inside the wellbore when compared with the interpretation from array production logging tools.

The fast marching method (FMM) is presented in this study to get the thermal map near hydraulic/natural fractures. This method solves the front tracking problems efficiently. By doing so, we can consider a heterogeneity formation with fractures, and also complex fracture geometry compared with analytical solution. It is also superior in visibility of stimulated reservoir volume (SRV) and in computational efficiency compared to finite difference simulation.

DEDICATION

To my parents, Weigang Cui and Qiulan Wen, for their encouragement, support and love.

ACKNOWLEDGEMENTS

I would like to express my sincere gratitude to my committee chair and advisor, Dr. Ding Zhu, for offering me the opportunity to study in TAMU, for her encouragement and patience throughout all my study. Also, I would like to give special thanks to Dr. A. Daniel Hill for his advice and motivation during this work. They teach me not only the technical skills and insight into research, but also the rigorous and positive attitude that I get benefit for the entire life.

I would like to thank Dr. Eduardo Gildin for being one of my committee members. His class on numerical simulation and his personal advice have been very helpful for the theoretical part of the study.

I would also like to thank Dr. Zhengdong Cheng for being my committee member and for his valuable comments. I have learned a lot during his course in transport phenomenon.

I thank Nozomu Yoshida, for sharing his opinions and discussions during this work.

I thank my friends and colleagues for the good time in Texas A&M University.

NOMENCLATURE

c_t	Total compressibility, 1/Psi [1/pa]
$\hat{C}_p$	Specific heat capacity, J/ (kg-K)
f	Friction factor, dimensionless
g	Gravity acceleration, m/s^2
H	Enthalpy, J/kg
K_T	Thermal conductivity, W/m/K
K_{JT}	Joule-Thomson coefficient, K/Pa
k	Reservoir permeability, md [m^2]
k_{app}	Apparent Darcy permeability, md [m^2]
k_f	Fracture permeability, md [m^2]
k_{mr}	Minimum permeability relative to Darcy, md [m^2]
p_i	Initial pressure, psi [pa]
p_{wf}	Wellbore pressure, psi [pa]
q	Surface flow rate, Mscf/d [m^3/s]
R	Wellbore inner radius, ft [m]
r_w	Wellbore radius, ft [m]
t	Time, day [s]
U	Internal energy, J/ kg

v	Velocity vector, m/s
x	Vertical coordinate parallel to transverse fracture
x_f	Fracture half length, ft [m]
y	Horizontal coordinate parallel to horizontal wellbore in fracture model
z	Horizontal coordinate parallel to horizontal wellbore in wellbore model

Greek

β	Thermal expansion coefficient, 1/K
ϕ	Porosity, fraction
γ	Pipe open ration, fraction
μ	Fluid viscosity, cp [Pa-s]
ρ	Density, kg/m^3

Superscripts

D	Dimensionless
I	Inflow
nd	Non-Darcy

TABLE OF CONTENTS

Page

LIST OF FIGURES

Page

LIST OF TABLES

Page

1 INTRODUCTION

1.1 Background

Downhole temperature measurements including permanent fiber-optic sensors and production logging tools (PLT) are increasingly applied in the field for hydraulically fractured well diagnosis in recent years. Although temperature is not the direct driving force in reservoir, the different thermal properties of fluids and the flow paths of fluids carry useful information to the wellbore. This information can be used to locate fractures or fluid entries, identify fluid types, predict flow rate distribution, and even further reduce the uncertainty of fracture/reservoir properties.

The dominated cause of temperature changes in the reservoir/fracture/wellbore system is the Joule-Thomson expansion of flowing fluid due to pressure drawdown. Besides, the flow velocity as well as thermal properties of fluid and rocks would affect measured temperature at the wellbore. For fractured horizontal wells in unconventional reservoirs, the transient temperature behavior during production is not clearly understood because the flow path in such a system is much more complicated than the conventional fractured vertical wells or horizontal wells without multiple fractures.

To monitor well performance, downhole permanent sensors or production logging tools are used to measure temperature and pressure as functions of time and location in the well system. Translate these measurements into flow distribution is invaluable for fracture treatment and well performance diagnosis. Unfortunately because of the complexity involved in the problem, full-scale simulation of the problem is not practical to be used in the field for real-time application because of the expensive computation involved.

Quantitative but efficient models with analytical/semi-analytical solutions can help to understand the mechanism of heat transfer in tight reservoirs and explore the potential usage of temperature measurements during long-term production period. It is under this motivation that this study conducted a systematic investigation on downhole temperature behavior in multi-stage fractured horizontal wells.

1.2 Literature Review

1.2.1 Hydraulic Fracture Diagnostic Technologies

Hydraulic fracturing is the key to satisfy the economic success of field development in shale reservoirs. Diagnosis of fracture efficiency is critical for the fracturing treatment evaluation and future improvement. There are many available tools that help us to determine important fracture properties such as fracture orientation, fracture height, fracture conductivity and the effective length. Each tool would have its advantage in some aspects and weakness in others.

Fracture diagnostics can be broken into two main groups: direct and indirect diagnostics. The indirect methods contain fracture modeling, well testing and production data analysis, while direct measurements are further subdivided into near wellbore and far field (Barree, R.D. et al, 2002).

For indirect diagnosis by fracture modeling, extensive inputs are usually required, such as permeability, closure stress and fluid saturation which are not always available. The reasonable data assumptions have to be made in order to be applied as diagnostic tools. Sensitivity studies should be done and the model need to be carefully calibrated. Post-frac well production analysis and well testing are also been applied to provide effective fracture

length. The effective fracture length is less than the created or proppant length, and this discrepancy causes incorrect constrain or calibration of models in the past. All the indirect measurements respond to primary variables in the system that actually control the measured data, finding the strong correlation between primary variables and the measured data is critical for reliable interpretation.

The direct, far-field techniques are fracture mapping tools, microseismic and tiltmeters. These diagnostic techniques are conducted from offset wellbores or from the surface during the fracture treatment and generally provide information about fracture growth and orientation. The main limitation of these techniques is that they map the total extent of hydraulic fracture growth but provide no information about the effective propped fracture length or conductivity. In addition, the resolution of these techniques decreases with increasing distance from the fracture. The following two paragraphs give a brief summary of these two technologies.

Microseismic fracture mapping: The image of the fracture generated is based on the detection of induced microseisms or micro-earthquakes caused by the change in stress and pore pressure associated with hydraulic fracturing. The microseisms are considered to be a result of shear slippage or tensile deformation that occurs along pre-existing planes of weakness (i.e. natural fractures, joints, etc.). The location of these microseismic events is obtained with a downhole receiver array of geophones positioned at the depth of the hydraulic fracture treatment in one or more offset wells. The data is gathered and processed with a surface data-acquisition system, and the microseismic events are located with techniques based on compressional and shear wave arrivals to provide time-dependent images of fracture growth and geometry. Several uncertainties associated with

microseismic fracture mapping have limited its application. The main limitation of this method is that microseisms are not just points of failure at the fracture tip; they can be either shear or tensile events that occur around the hydraulic fracture along natural fractures, bedding and other plane of weakness. Moreover, detection of microseismic events is a function of the fracture treatment (i.e. pumping rate), reservoir properties and also distance to location of the offset wells.

Surface and Downhole Tiltmeter: The principle of tiltmeter fracture mapping is that a created hydraulic fracture results in a characteristic deformation pattern of the rock surrounding the fracture. By measuring the induced deformation of the formation at several locations (surface or downhole), the fracture orientation and geometry can be estimated. Surface tiltmeters are positioned in an array surrounding the treatment well and analysis of the results provides a measurement of the fracture azimuth, dip, depth-to-fracture center, and total fracture volume. Because surface tiltmeters are typically very far from the created fracture, they cannot precisely resolve fracture length and height. Downhole tiltmeter mapping is based on the same concept as surface tiltmeter mapping, but instead of being at the surface, the tiltmeters are positioned by wireline in one or more offset wellbores at the depth of the hydraulic fracture and significantly more sensitive to fracture dimensions. The measured tilt is used to determine fracture height, length, and width. Tiltmeter mapping suffers from a non-uniqueness solution which always exists in inverse problems. This becomes more severe when no information about fracture initiation is available. When a long horizontal well completed with an uncemented liner or openhole is fractured, the number of created hydraulic fractures is unknown, as well as specific fracture orientations, dimensions, and locations. The mapping problem then often has more degrees of freedom

than the number of measurements and it becomes impossible to get reliable information about any individual fracture.

There are some other tools that can be deployed into the wellbore and usually log a physical property in the near-wellbore region. The major limitation of these methods is that they can only provide information about the fracture not far from the wellbore and their main application is to identify the locations where fluid and/or proppant exit the wellbore. The following two paragraphs introduce radioactive tracer and production logging tools.

Radioactive Tracer: Radioactive tracers have a long history of use in the oil industry. For fracture diagnostics purpose, they can be added to the stimulation fluid and proppant, and after the treatment, radioactivity in the near-wellbore region can be measured by running a gamma-ray log. Multiple isotopes can be used to help define the placement of pad fluid and various proppant stages. In vertical wells, radioactive tracers provide limited information about fracture height, but in deviated and horizontal wells it is difficult to obtain useful information about the fracture geometry. The method also depends on the completion, and any leakage between isolation packages will bring wrong information to the diagnosis.

Production Logging: Noise log uses sound that is created by fluid entry into the wellbore to identify fluid entry points. Spinner surveys combine multiple sensors, such as flow meter (spinner), temperature, pressure, fluid density, capacitance, and gamma ray, to allow a full evaluation of the amount and type of fluid being produced into the wellbore from each set of open perforations. This method can be used to identify the perforations that were fractured and their contribution to production. However, production logs are difficult and expensive to run in horizontal wells.

Considering the capabilities and limitations of the above near-wellbore techniques, industry have been trying to apply distributed temperature sensing (DTS) and distributed acoustic sensing (DAS) for real-time monitoring during injection and production. The advantage is that the system generally do not have interfere with flow, having more flexibility for deployment in restricted downhole environments compared to conventional logging tools, and can be used for short-term as well as permanent monitoring of dynamic data.

Distributed Acoustic Sensing (DAS) offers many advantages over traditional methods such as gauges, geophones and logging tools. The same fiber can be used for both DTS and DAS, thus operational cost is reduced. DAS can be used for zonal injection/production allocation, detecting leaks, and tracking fluid transport in the wellbore. This technology applies to field scale for qualitative analysis, quantitative interpretation is also highly demanded to connect flow rate with acoustic signal. There is also an issue with large data volumes that are associated to DAS need to be processed. With proper processing, the value of DAS can be achieved by integrated with other sources of data.

Table 1.1 shows the summary of the different methods and the certainty about fracture properties.

Table 1.1– Fracture diagnostic tools with measurement certainty

Group	Diagnostic	Ability to Estimate							
		Initiation Location	Length	Height	Width	Azimuth	Dip	Volume	Conductivity
Indirect	Net Pressure Analysis								
	Well Testing								
	Production Analysis								
Direct, near wellbore	Radioactive Tracers								
	Temperature Logging								
	Production Logging								
	Distributed Temperature Sensor								
	Distributed Acoustic Sensor								
	Borehole Image Logging								
	Downhole Video								
	Caliper Logging								
Direct, Far Field	Surface Tilt Mapping								
	DH Offset Tilt Mapping								
	Microseismic Mapping								
	Treatment Well Tiltmeters								

	Will Determine
	May Determine
	Can Not Determine

The near-wellbore methods can capture the detailed phenomena within a few feet thus we know what happened at fracture contact area within the perforated intervals. Take **Fig. 1.1** as an example, for direct, near wellbore diagnosis by a temperature/spinner survey we can identify the zones that do not produce. The track on the left shows there is no flow contribution from upper interval. A refrac was performed in upper section and the well productivity increased by 40%. In a case of fracturing, fracture height can be determined only for longitudinal fracture. On the other side, far-field technologies such as microseismic mapping and surface/downhole tiltmeter mapping, can provide large-scale views of fracture dimensions in hundreds feet deep into the reservoir.

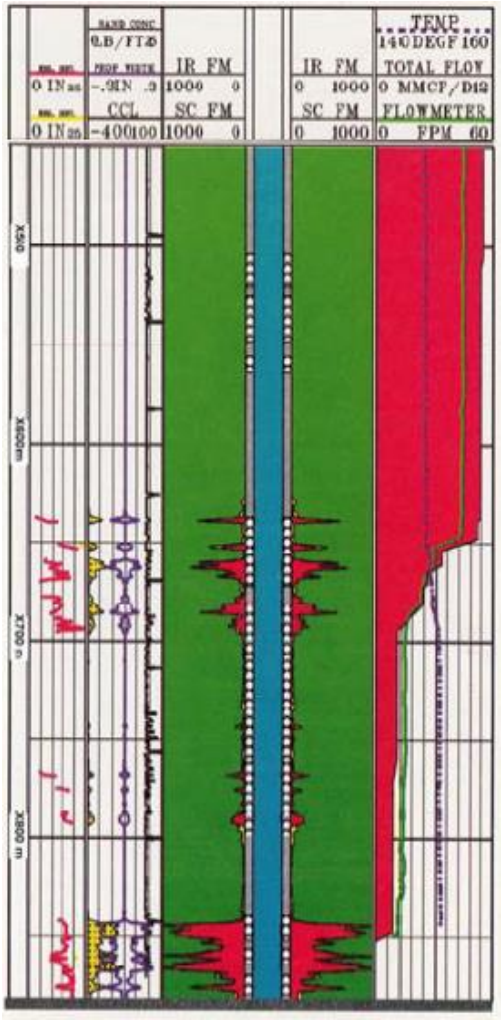

Fig. 1.1– Lack of production from unpropped perforated top intervals (Barree, 2002).

A better way to do fracture diagnostics is to integrate different technologies. For example, temperature logging can pin-point the fluid entry point and determine the efficiency of perforations along the wellbore. This could help the modeling process, and we could also use the fracture half-length estimated from microseismic data to reduce the uncertainty of the numerical modeling.

1.2.2 Downhole Temperature Measurements

Fiber optic sensors and production logging tools are the common methods to assess flow profile and near-wellbore information by measuring temperature distribution downhole.

Temperature logging has been used as to evaluate well performance for over 50 years. Since the temperature is affected by material outside the casing, temperature logging is sensitive to not only the borehole but also the formation and the casing-formation annulus. Usually temperature logging could be used to evaluate well characteristics by identifying anomalous temperature changes. It can be used to locate cement tops (Peacock, D.R., 1965), detect casing leaks and fluid movement behind casing, estimate fracturing fluid volume being injected (Arthur, A., et al. 2013), interpret fracture height (Davis, E.R., et al. 1997) and detect gas/oil entry from productive intervals.

Temperature instruments are made with the elements with resistance, typically wire coils. The element connecting a bridge circuitry or a constant-current circuit with the voltage that responses proportional to temperature. The voltage signal will convert to frequency signal and transmit to the surface, then the surface instrument converts the signal. Temperature log is usually run in a string with other tools like spinner flowmeter and radioactive tracer. When production log runs upwards, the temperature anomalies would be smeared over great distances, which reduces the log resolution (Hill, 1990).

Fiber optic distributed temperature sensor (DTS) is a relatively recent technology in oil and gas industry. It provides continuous real-time distributed temperature profiles with high resolution and accuracy over the duration of monitoring periods without any intervention. Fiber optic cables can be deployed in several configurations in a wellbore,

more importantly, across perforated intervals. If DTS is deployed outside the casing and the cement, then the measured temperature would reflect more accurate information about the reservoir since it is less influenced by the wellbore mixture flow.

The details about DTS mechanism and deployment methods have been described thoroughly in recent published papers (Glasbergen. et al. 2009, Holley. et al. 2014). Optical fiber would transmit laser pulses multiple times per second and an optical receiver detects the reflected light signal. This back-scattered light is caused by the interaction of the transmitted laser pulse and the fiber molecules in the cable. The frequency response for a back-scattered signal is shown is **Fig. 1.2**. The amplitudes of the Raman Stokes and anti-Stokes signals are collected, while one is weakly dependent on temperature and the other is strongly affected by temperature. The relative intensities between Stokes and anti-Stokes determine the temperature at where the back-scattering happens. The more laser pulses transmitted, the better resolution could be obtained for the temperature measurements.

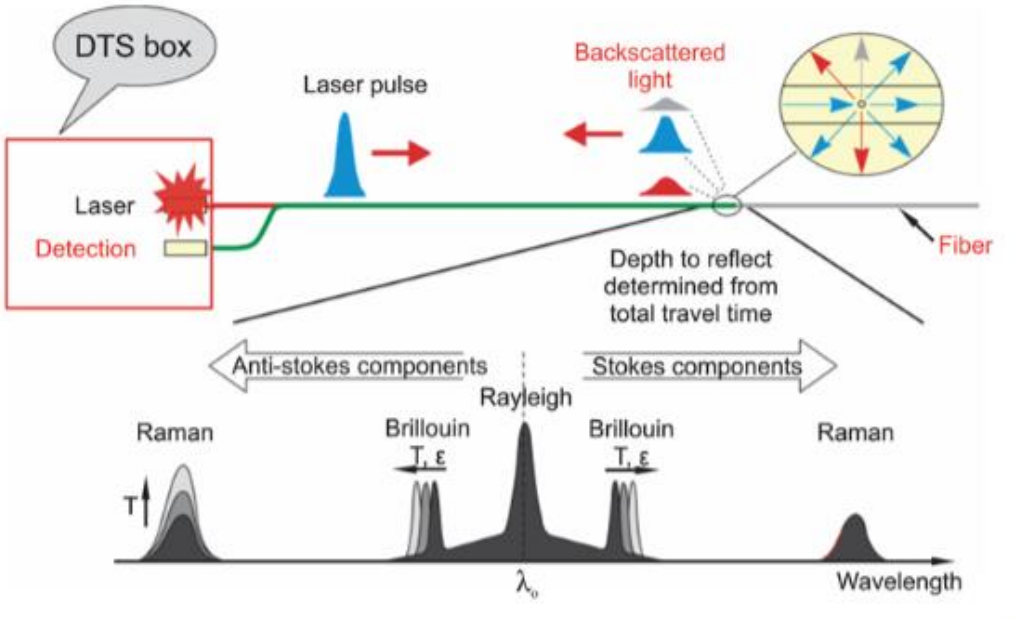

Fig. 1.2– DTS operating principle (Holley, 2014).

In this study, the temperature data from production logging tools will be used to estimate the flow rate distribution and the fracture efficiency along a horizontal wellbore.

1.2.3 Thermal Modeling in Wellbore and Reservoir

With the field applications of downhole temperature measurement technology, the theoretical investigations have been developed.

One of the earliest works on temperature prediction was done by Ramey (1962). Ramey's model assumes steady state heat transfer in a wellbore, while the heat conduction to the earth is a transient process, and solved by the line source method. The author presented several gas/water injection examples and showed good agreement on the matching results with measured wellbore temperature. Jacques H. (2004) compared a rigorous solution by numerical simulation with Ramey's approximate one and pointed out that Ramey's model would overestimate the temperature in early transient period.

Sagar et al. (1991) developed a two-phase model based on Ramey's heat transfer mechanism and took wellbore inclination into consideration. The authors also calculated the Joule-Thomson heating or cooling effect and kinetic energy terms by pressure changes in wellbore.

Hasan and Kabir (1991) considered the heat transfer at the formation/wellbore interface by Fourier Law of heat conduction. A transient formation heat transfer model was presented which assumed a gradual changed heat flow from or to a wellbore.

Yoshioka et al. (2005 and 2007) presented a multiphase steady state thermal model to detect the water/gas entry location along a horizontal well. In this study, a 1-D analytical reservoir thermal model was developed and coupled with simplified single phase liquid or

gas wellbore model. The wellbore inclination and damage zone were also considered. Based on the steady state temperature behavior analysis, Sui et al. (2008) emphasized the importance of transient behavior and estimated multilayer formation properties in a single phase vertical well, which included formation permeability, damage permeability and radius.

Li (2009) used the streamline reservoir simulator to obtain transient pressure behavior and coupled with a two-phase thermal model to identify water/gas entry intervals, and to estimate corresponding flow rate. Muradov and Davies (2011) discussed the derivation of asymptotic analytical solution for transient temperature changes and analyzed the transient temperature behavior when flow rate changed during well testing.

Even through numerical simulation has flexibility to handle complex reservoir conditions, computation becomes challenging when coupling reservoir models with wellbore models, because of the effect of wellbore trajectory and wellbore thermal-/hydro-dynamics. Field applications of these models still remains challenging.

Compared to other types of well systems, fractured horizontal wells have different flow pattern which results in a more complex temperature behavior. The dominated cause of temperature changes in such a reservoir/fracture/wellbore system is the Joule-Thomson expansion of flowing fluid due to reservoir drawdown.

App (2013) emphasized the impact of permeability on sandface flowing temperatures by determining the ratio of heat transfer by convection to conduction within a reservoir. This ratio is known as Peclet number.

$$P_e = -\frac{uL}{\alpha} \tag{1.1}$$

where L is the characteristic length, u is the local flow velocity, and α is the thermal diffusivity. By considering a steady state radical flow from reservoir to wellbore, the author derived the dimensionless wellbore temperature solution as

$$T_{wD} = \frac{T_w - T_i}{T_i} = \frac{JT_D}{P_e \ln r_{eD}} \left(r_{eD}^{-Pe} - 1 \right) + JT_D \tag{1.2}$$

where T_w denotes wellbore temperature, T_i denotes reservoir initial temperature, r_{eD} and p_e are dimensionless reservoir boundary (r_e/r_w) and boundary pressure. JT_D is dimensionless Joule-Thomson coefficient defined as below.

$$JT_D = -\frac{\mu_{JT} \Delta P}{T_i} = -\frac{\beta T - 1}{\rho \hat{C}_p T_i} \Delta p \tag{1.3}$$

where β is thermal expansion coefficient, ρ is density and $\hat{C}_p$ is specific heat capacity.

Figure 1.3 illustrates the relative impact of permeability on wellbore temperature for oil reservoir. The 'JT' curve represents JT_D in **Eq. 1.3**, which is the energy generated by Joule-Thomson expansion of the reservoir fluid based on a certain pressure drawdown. The 'convection/conduction' ratio (Peclet number) curve represents the amount of energy transferred because of conduction. As the Peclet number is low referring conduction dominates over convection when fluid velocity is low in reservoir. This results a diminishing temperature change so that the total temperature change 'total ΔT 'is close to zero at low permeability.

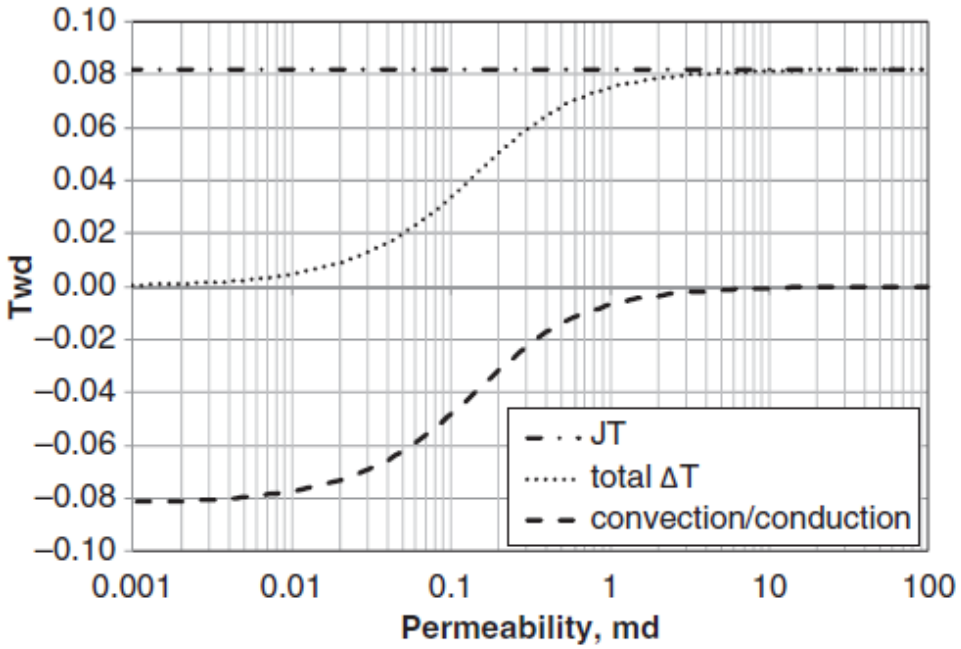

Fig. 1.3– Factors contributing to total ΔT in oil reservoir (App, 2013).

For low permeability reservoirs, such as shale and tight sand formations, the Peclet number is small and the temperature change in formation is less than 0.1℉. The considerable temperature change only happens in a small vicinity around the fractures. Thus fracture scale should have a detectable influence on temperature acquiring at the wellbore.

1.3 Problem Description

The rapid development of downhole temperature measurement technology in recent years enables us to obtain reliable temperature data during both fracturing treatment and later production periods. The previous studies demonstrated the potential of using mathematical models to understand the thermal behavior of fluids in a reservoir and

wellbore system, thus regress upon fluid type, flow rate, and certain reservoir parameters including longitudinal fracture height, layered reservoir permeability and damage skin.

For multi-stage fractured horizontal well in unconventional reservoir, the pressure transient period may last years for production wells, and for most of the time, the flow pattern in fractured reservoir is bilinear or elliptic flow which is quite different from the radical flow directly from the reservoir to the wellbore in conventional reservoir. Because of this, the thermal behavior need to be studied carefully in order to capture the unique characteristic of fractured unconventional reservoir.

Previous studies focus on the transient temperature behavior by flow rate constraint at the wellbore within a relatively short time, which is not suitable for long-term production in unconventional reservoirs. The flow rate constraint condition provides reservoir information about skin factor near wellbore because of the corresponding pressure transient behavior, but for fractured horizontal wells, it is not practical to fix a production rate of each stage. On the contrary, the goal is to estimate the flow rate distribution from each stage of fracture along the wellbore by downhole temperature interpretation.

For this reason, it is urgently desired to have a quantitative interpretation of dynamic temperature data with appropriate boundary constraint to obtain a better understanding of well performance and to diagnosis the efficiency of hydraulic fractures in tight reservoirs.

1.4 Objectives

In this dissertation, Section 1 introduces the research background by reviewing the literature of hydraulic fracture diagnosis method, downhole temperature measurements and thermal modeling. The objectives of this research are proposed.

Section 2 presents the mathematical modeling to describe the transient fracture/formation flow and thermal behavior. The semi-analytical solution separates the complex problem into parts which is important to the mechanism of heat transfer in porous media. The solution procedure summarizes how to couple the fracture/formation model with the wellbore model and the steps to run the program. Model validation compares the semi-analytical solution with numerical simulation by finite difference results for the fracture/formation flow model, and then compares the wellbore arriving temperature with a fully numerical simulator to verify the model.

Section 3 focuses on the results and discussions of synthetic examples. The first example uses constant flow rate constraint to simulate early-time production, followed by a constant bottomhole pressure constraint example to simulate long-term production and analyze the transient behavior corresponding to flow rate decline. Key parameters are studied to test their impact on temperature at the wellbore.

Section 4 applies the developed semi-analytical model to the field data and demonstrate the possibility of using temperature data to diagnose fractured well performance during production. We estimate flow rate distribution along wellbore, and compare this flow profile with the PLT measurements (array tools). The study shows a promising application of using temperature data to interpret the performance of multi-stage fractured wells.

Section 5 uses a new simulation approach, Fast Marching Method (FMM), to predict temperature behavior in hydraulic fractured heterogeneous reservoirs with/without natural fractures. This new approach is superior in visibility and has computational efficiency for unconventional reservoirs. Further study is highly demanded on this topic.

Section 6 summarizes the work and makes some recommendations for future work.

In summary, the objectives of the research are:

(1) To establish a formation/fracture/wellbore coupled model to describe the mass and energy transfer in multi-stage fractured horizontal wells during gas production.

(2) To understand the transient temperature behavior under different production constraints, including constant flow rate and constant bottomhole pressure. To conduct the sensitivity study of key parameters, such as fracture conductivity and fracture half-length, on transient temperature behavior.

(3) To apply field data to the model and estimate flow rate distribution along horizontal wellbore, therefore to evaluate the success of hydraulic fracture treatment of each stage. To compare the flow rate distribution results with array tools interpretation and commercial software, comment the advantage and disadvantage of the temperature interpretation method.

(4) To build up the thermal modeling by fast marching method. To investigate the feasibility of using such a method for heterogeneous reservoir with hydraulic/nature fractures.

2 MODEL DEVELOPMENT

2.1 Introduction

This section presents the fracture and formation flow/thermal model, and couples the models with a single phase 1D wellbore model to predict temperature behavior along the wellbore and in the reservoir.

The temperature interpretation model contains four sections: the wellbore flow and thermal model, the fracture and formation flow and thermal model. The arriving pressure and temperature at the inner boundary of fracture/formation model are used as input data to the wellbore model. This model can be applied to single phase oil/gas wells.

The wellbore model simulates the transient fluid behavior considering sectional inflow from outside. The model assumes instantaneous equilibrium at any time and locations, which ignores the mixing effect of upstream fluid with inflow from fracture. The wellbore thermal model considers the heat convection caused by the inflow from fractures, the heat conduction between the wellbore and the formation at non-communication sections, and the Joule-Thomson effect that happens inside the wellbore due to fluid expansion.

The fracture/formation model assumes linear flow inside formation and fracture which is a reasonable assumption for shale/tight reservoirs. For the thermal model in fracture/formation, an infinite fracture conductivity case with constant flow rate is conducted by a semi-analytical approach of operator splitting method, and finite conductivity case can be solved numerically by finite difference method. The semi-analytical solution could be used to separate different mechanisms thus help the

understanding of the influence individually. It can also been used to validate the numerical model.

All of the equations are discretized in space and time, and coupled to be solved semi-analytically or numerically to get the temperature distribution along wellbore and inside reservoir. The following sections present the model description.

2.2 Wellbore Transient Model

The wellbore model calculates pressure, temperature and fluid velocity distribution along a wellbore for single phase gas or liquid flow. The model was developed based on the conservation of mass, momentum and energy (Yoshioka et al. 2007). Transient behavior of fluid flow is considered in the calculation. **Fig. 2.1** shows the gridding system used in the wellbore model. The fluid flow from a fracture merging with the upstream fluid inside the wellbore, and then flow towards the heel. A transient model is used instead of a steady state model to better describe the temperature behavior.

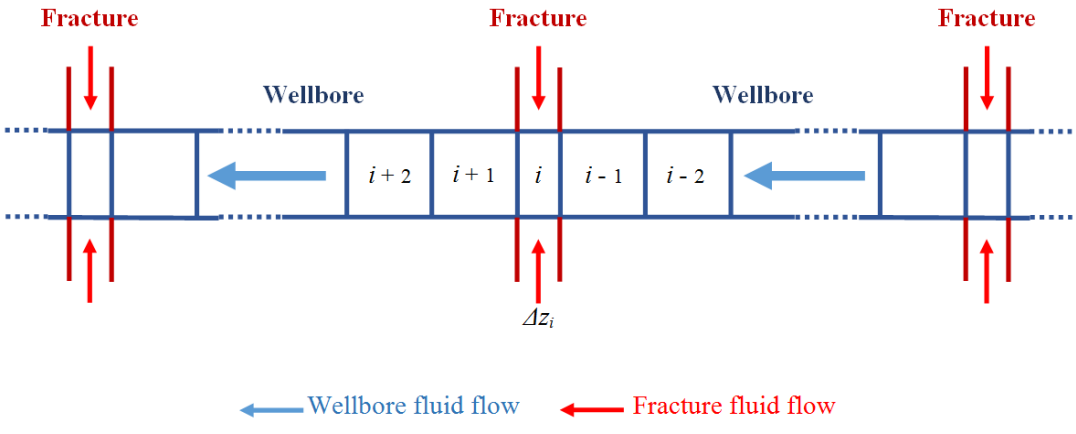

Fig. 2.1– Schematic of wellbore model system.

2.2.1 Wellbore Mass and Momentum Balance Equation

The mass balance equation states:

$$\frac{\partial \rho}{\partial t} = \frac{2\gamma \rho_I v_I}{R} - \frac{\partial}{\partial z}(\rho v) \tag{2.1}$$

Based on the momentum balance, we have the equation:

$$\frac{\partial p}{\partial z} = -\frac{\rho f v^2}{R} - \frac{\partial}{\partial z}(\rho v^2) - \rho g \sin\theta - \frac{\partial(\rho v)}{\partial t} \tag{2.2}$$

where in the above equations, p, T and v are pressure, temperature and velocity of the fluid flowing inside the wellbore, ρ_I and v_I are density and velocity of inflow fluid from fractures. R is wellbore inner radius, f is friction factor and t is time. θ is the wellbore inclination angle. When the well starts producing, the pressure at the heel is set to a target bottomhole flowing pressure or a constant flow rate from fractures is defined. The pipe open ratio γ is defined as the ratio of the opening area of the pipe to the total surface area of the pipe. We solve the above equations numerically. The gridding is based on the location of the fractures. In the grids that contain fractures, γ equals to 1, otherwise γ equals to 0.

2.2.2 Wellbore Energy Balance Equation

The wellbore thermal model describes the transient temperature behavior inside wellbore. This is a 1D model. When apply to multiphase flow situation, the model simply uses volumetric-averaged properties and ignores the interaction between phases.

Considering the general energy balance equation, we have

$$\left\{\begin{array}{c}\text{Rate of}\\ \text{increase of}\\ \text{energy}\end{array}\right\}=\left\{\begin{array}{c}\text{Rate of}\\ \text{energy in}\end{array}\right\}-\left\{\begin{array}{c}\text{Rate of}\\ \text{energy out}\end{array}\right\}+\left\{\begin{array}{c}\text{Rate of work}\\ \text{done on system}\\ \text{by external forces}\end{array}\right\}+\left\{\begin{array}{c}\text{Rate of}\\ \text{energy}\\ \text{production}\end{array}\right\} \tag{2.3}$$

The combined energy flux vector is defined as (Bird et al., 2002)

$$\mathbf{e}=\left(\frac{1}{2}\rho v^2+\rho\hat{U}\right)\mathbf{v}+\left[\boldsymbol{\pi}\cdot\mathbf{v}\right]+\mathbf{q} \tag{2.4}$$

where **e** is the sum of the convective energy flux, the rate of doing work (per unit area) by molecular mechanisms, and the rate of transporting heat (per unit area) by molecular mechanisms. The total molecular stress tensor $\boldsymbol{\pi}$ is split into two components and is expressed as $\boldsymbol{\pi}=p\boldsymbol{\delta}+\boldsymbol{\tau}$, so that $\left[\boldsymbol{\pi}\cdot\mathbf{v}\right]=p\mathbf{v}+\left[\boldsymbol{\tau}\cdot\mathbf{v}\right]$. Then **Eq. 2.4** is written in the form

$$\mathbf{e}=\left(\frac{1}{2}\rho v^2+\rho\hat{H}\right)\mathbf{v}+\left[\boldsymbol{\tau}\cdot\mathbf{v}\right]+\mathbf{q} \tag{2.5}$$

The rate of increase of energy over the differential volume element $\pi R^2\Delta z$ is

$$\left\{\begin{array}{c}\text{Rate of}\\ \text{increase of}\\ \text{energy}\end{array}\right\}=\pi R^2\Delta z\frac{\partial}{\partial t}\left(\frac{1}{2}\rho v^2+\rho\hat{U}\right) \tag{2.6}$$

where $\frac{1}{2}\rho v^2$ is the kinetic energy per unit volume and $\rho\hat{U}$ is the internal energy per unit volume.

The rate of energy in is

$$\left\{\begin{array}{c}\text{Rate of}\\ \text{energy in}\end{array}\right\}=2\pi R\Delta z\left(e_r\right)_{r=R}+\pi R^2\left(e_z\right)_z \tag{2.7}$$

where e_r and e_z are the combined energy flux in the radial direction and the axial direction respectively.

The rate of energy out is

$$\left\{\begin{array}{c}\text{Rate of}\\ \text{energy out}\end{array}\right\} = \pi R^2 \left(e_z\right)_{z+\Delta z} \tag{2.8}$$

Because the rate of work done by external force arises from gravity force, it is written as

$$\left\{\begin{array}{c}\text{Rate of work}\\ \text{done on system}\\ \text{by external forces}\end{array}\right\} = -\pi R^2 \Delta z \rho v g \sin\theta \tag{2.9}$$

The energy production in the system is assumed to be zero. Substituting **Eq. 2.6**, **2.7**, **2.8** and **2.9** into **Eq. 2.3**, and taking $\Delta z \rightarrow 0$, we have

$$\frac{\partial}{\partial t}\left(\frac{1}{2}\rho v^2 + \rho\hat{U}\right) = \frac{2\left(e_r\right)_{r=R}}{R} - \frac{\partial\left(e_z\right)}{\partial z} - \rho v g \sin\theta \tag{2.10}$$

where the radial combined energy flux at the wall is

$$\left(e_r\right)_{r=R} = \left(\frac{1}{2}\rho_I {v_I}^2 + \rho_I \hat{H}_I\right) v_I - \left(\tau_{rz} v_z\right)_{r=R} - \left(\tau_{rr} v_r\right)_{r=R} + q_I \tag{2.11}$$

The combined energy flux in the axial direction is

$$e_z = \left(\frac{1}{2}\rho v^2 + \rho\hat{H}\right) v_z - \tau_{zz} v_z - \tau_{zr} v_r + q_z \tag{2.12}$$

Since $v_z = 0$ at $r = R$, in **Eq. 2.11**, we have

$$\left(\tau_{rz} v_z\right)_{r=R} = 0 \tag{2.13}$$

The definition of stress is expressed as

$$\tau_{rr} = 2\mu\frac{\partial v_r}{\partial r} - \frac{2}{3}\mu\left(\frac{1}{r}\frac{\partial}{\partial r}(rv_r) + \frac{\partial v_z}{\partial z}\right) = 2\mu\frac{\partial v_r}{\partial r} - \frac{2}{3}\mu\left(\frac{\partial v_r}{\partial r} + \frac{v_r}{r} + \frac{\partial v_z}{\partial z}\right) \tag{2.14}$$

At $r = R$, we have

$$\left.\frac{\partial v_r}{\partial r}\right|_{r=R} = 0 \tag{2.15}$$

$$\left.\frac{\partial v_z}{\partial z}\right|_{r=R} = 0 \tag{2.16}$$

Then **Eq. 2.14** becomes

$$\tau_{rr} = -\frac{2}{3}\mu\frac{v_r}{r} \tag{2.17}$$

Substituting **Eqs. 2.13** and **2.17** into **Eq. 2.11**, we have

$$(e_r)_{r=R} = \left(\frac{1}{2}\rho_I {v_I}^2 + \rho_I \hat{H}_I\right)v_I + \frac{2}{3}\mu\frac{v_I}{R} + q_I \tag{2.18}$$

Similarly, $v_r = 0$, and the heat conduction in z direction can be neglected, so $q_z = 0$. **Eq. 2.12** becomes

$$e_z = \left(\frac{1}{2}\rho v^2 + \rho\hat{H}\right)v_z - \tau_{zz}v_z = \left(\frac{1}{2}\rho v^2 + \rho\hat{H}\right)v - \frac{4}{3}\mu\frac{\partial v}{\partial z}v \tag{2.19}$$

Considering that there is only heat convection occurs in the open area of pipe, and only heat conduction occurs in the covered area of pipe. We use the pipe open ratio γ, and **Eq. 2.18** is written as

$$(e_r)_{r=R} = \gamma\left[\left(\frac{1}{2}\rho_I v_I^2 + \rho_I \hat{H}_I\right)v_I + \frac{2}{3}\mu\frac{v_I^2}{R}\right] + (1-\gamma)q_I \tag{2.20}$$

Substituting **Eqs. 2.19** and **2.20** into **Eq. 2.10** and rearranging it, we have

$$\frac{\partial}{\partial t}\left(\rho\hat{U}\right)=\frac{2\gamma}{R}\rho_I\hat{H}_I v_I+\frac{2(1-\gamma)}{R}q_I-\frac{\partial}{\partial z}\left(\rho\hat{H}v\right)-\rho v g\sin\theta+E_{KE}+E_{VS} \quad (2.21)$$

where E_{KE} is the kinetic energy term, and E_{VS} is the viscous shear term, and they have the following expressions

$$E_{KE}=\frac{2\gamma}{R}\left(\frac{1}{2}\rho_I v_I^2\right)v_I-\frac{\partial}{\partial z}\left[\left(\frac{1}{2}\rho v^2\right)v\right]-\frac{\partial}{\partial t}\left(\frac{1}{2}\rho v^2\right) \quad (2.22)$$

$$E_{VS}=\frac{2\gamma}{R}\left(\frac{2}{3}\mu\frac{v_I^2}{R}\right)+\frac{4}{3}\frac{\partial}{\partial z}\left(\mu\frac{\partial v}{\partial z}v\right) \quad (2.23)$$

Expanding the left-hand side of **Eq. 2.21**, we have

$$\frac{\partial}{\partial t}\left(\rho\hat{U}\right)=\rho\frac{\partial\hat{U}}{\partial t}+\hat{U}\frac{\partial\rho}{\partial t} \quad (2.24)$$

The internal energy $\hat{U}$ can be expressed as

$$\hat{U}=\hat{H}-\frac{p}{\rho} \quad (2.25)$$

Substituting **Eq. 2.25** into **Eq. 2.24** gives

$$\frac{\partial}{\partial t}\left(\rho\hat{U}\right)==\rho\frac{\partial\hat{H}}{\partial t}-\frac{\partial p}{\partial t}+\hat{H}\frac{\partial\rho}{\partial t} \quad (2.26)$$

Substituting the above equation and the mass balance equation **2.1** into **Eq. 2.21**

$$\begin{aligned}&\rho\frac{\partial\hat{H}}{\partial t}-\frac{\partial p}{\partial t}+\hat{H}\left[\frac{2\gamma\rho_I v_I}{R}-\frac{\partial}{\partial x}(\rho v)\right]\\&=\frac{2\gamma}{R}\rho_I\hat{H}_I v_I+\frac{2(1-\gamma)}{R}q_I-\frac{\partial}{\partial z}\left(\rho\hat{H}v\right)-\rho v g\sin\theta+E_{KE}+E_{VS}\end{aligned} \quad (2.27)$$

Rearranging the above equation, we have

$$\begin{aligned}\rho\frac{\partial\hat{H}}{\partial t}-\frac{\partial p}{\partial t}=&\frac{2\gamma}{R}\rho_I v_I\left(\hat{H}_I-\hat{H}\right)+\frac{2(1-\gamma)}{R}q_I-\rho v\frac{\partial\hat{H}}{\partial z}\\&-\rho v g\sin\theta+E_{KE}+E_{VS}\end{aligned} \quad (2.28)$$

The definition of enthalpy is

$$d\hat{H} = \left(\frac{\partial \hat{H}}{\partial T}\right)_p dT + \left(\frac{\partial \hat{H}}{\partial p}\right)_T dp = \hat{C}_p dT + \frac{1}{\rho}(1-\beta T)dp \tag{2.29}$$

where β is the thermal expansion coefficient. The first term in the left-hand side and the third term on the right-hand side of **Eq. 2.28** can be written as

$$\frac{\partial \hat{H}}{\partial t} = \hat{C}_p \frac{\partial T}{\partial t} + \frac{1}{\rho}(1-\beta T)\frac{\partial p}{\partial t} \tag{2.30}$$

$$\frac{\partial \hat{H}}{\partial z} = \hat{C}_p \frac{\partial T}{\partial z} + \frac{1}{\rho}(1-\beta T)\frac{\partial p}{\partial z} \tag{2.31}$$

In order to calculate the enthalpy difference, we take the integration of **Eq. 2.29** so the enthalpy difference is

$$\hat{H}_I - \hat{H} = \int_T^{T_I} \hat{C}_p dT + \int_p^{p_I} \frac{1}{\rho}(1-\beta T)dp \tag{2.32}$$

Assuming that the heat capacity is constant, and the inflow pressure is the same as the wellbore pressure, the enthalpy difference can be simplified as

$$\hat{H}_I - \hat{H} = \hat{C}_p(T_I - T) \tag{2.33}$$

Substituting **Eqs. 2.30**, **2.31** and **2.33** into **Eq. 2.28**, and dividing by $\rho v \hat{C}_p$ in both side, we obtain

$$\begin{aligned}\frac{1}{v}\frac{\partial T}{\partial t} - \frac{\beta T}{\rho v \hat{C}_p}\frac{\partial p}{\partial t} = \frac{2\gamma}{R}\frac{\rho_I v_I}{\rho v}(T_I - T) + \frac{2(1-\gamma)}{R\rho v \hat{C}_p}q_I - \frac{\partial T}{\partial z} \\ - \frac{(1-\beta T)}{\rho \hat{C}_p}\frac{\partial p}{\partial z} - \frac{g\sin\theta}{\hat{C}_p} + \frac{(E_{KE} + E_{VS})}{\rho \hat{C}_p}\end{aligned} \tag{2.34}$$

Here the Joule-Thomson effect coefficient is defines as

$$K_{JT} = \frac{\beta T - 1}{\rho \hat{C}_p} \tag{2.35}$$

The heat conduction between the wellbore and the formation is expressed as

$$q_I = U_T\left(T_I - T\right) \tag{2.36}$$

where U_T is the overall heat transfer coefficient depends on the wellbore structure and thermal properties of the materials.

Substituting **Eqs. 2.35** and **2.36** into **Eq. 2.34**, neglecting the kinetic energy term and the viscous shear term, the wellbore energy balance equation can be written as

$$\begin{aligned} &\frac{1}{v}\frac{\partial T}{\partial t} - \frac{\beta T}{\rho v \hat{C}_p}\frac{\partial p}{\partial t} \\ &= \frac{2\gamma}{R}\frac{\rho_I v_I}{\rho v}\left(T_I - T\right) + \frac{2\left(1-\gamma\right)}{R\rho v \hat{C}_p}U_T\left(T_I - T\right) - \frac{\partial T}{\partial z} + K_{JT}\frac{\partial p}{\partial z} - \frac{g\sin\theta}{\hat{C}_p} \end{aligned} \tag{2.37}$$

Initially, the temperature in the entire system is the geothermal temperature, or this temperature can be calculated by a thermal model for warmback after fracturing period. For horizontal wells, geothermal temperature is an important input data for modeling; we also can calculate initial temperature T_i along the well using well trajectory data. The shut-in temperature can also be used as geothermal temperature if it is available. In order to identify the subtle measured temperature variation, thermal models must account for all the subtle thermal effects including Joule-Thomson expansion and thermal conduction between wellbore and formation.

The solution of the mass, momentum and energy equations provides the temperature and pressure distribution based on a given flow rate and fluid inflow temperature at any time and location along the wellbore.

2.3 Fracture/Formation Model

2.3.1 Fracture/Formation Flow Model

A semi-analytical tri-linear model developed by Lee and Brockenbrough (1986) was adopted for reservoir flow problem. **Fig. 2.2** shows the geometry of the fracture and the flow pattern in reservoir. The domain is divided into three distinct parts, the fracture, the inner formation that directly conjuncts with the fracture, and the outer formation that connects with the inner formation. Modification is made to improve the model by considering different permeability in the inner and outer formation. This method solves the equations in Laplace domain, and then convert to real space by using numerical inversion of Laplace transform (Stehfest, 1970).

The model uses the following assumptions:

- All transverse hydraulic fractures have finite conductivity ($0 < F_{CD} < \infty$).
- Fracture height is equal to formation thickness.
- Only hydraulic fractures contribute production.
- Reservoir is rectangular-shape. Both inner formation and outer formation are considered homogeneous but they could have two different permeability respectively.
- Single oil or gas phase can be applied to the model. For gas phase, pseudo-pressure concept is adopted.

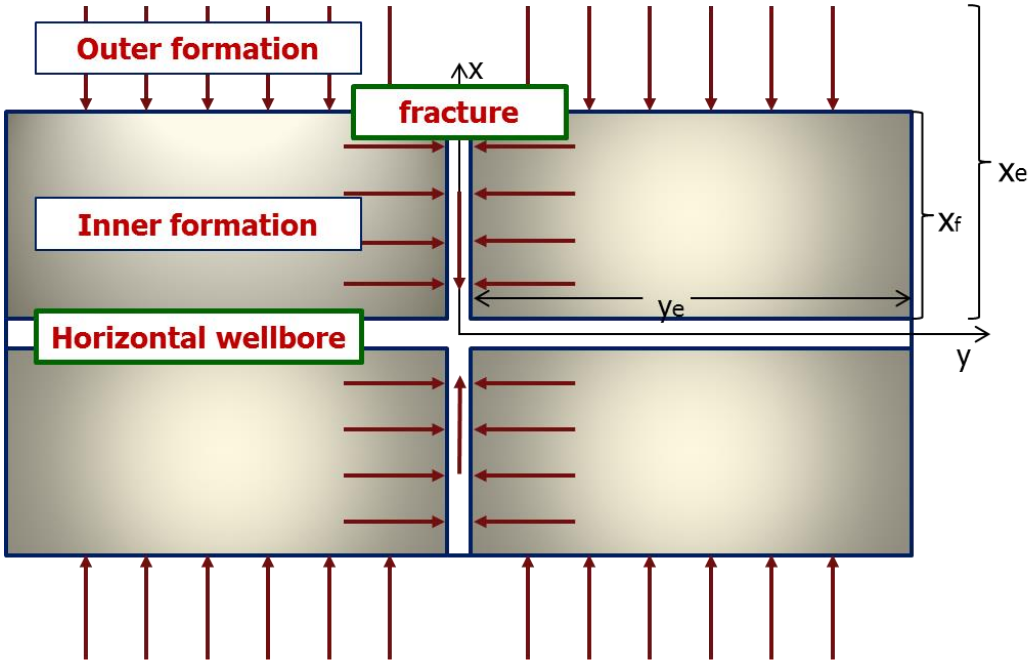

Fig. 2.2– Tri-linear fracture/formation model.

For convenience, the solution is derived in terms of dimensionless variables. The definition of the dimensionless variables are shown below.

For constant flow rate constraint in SI unit:

$$p_D = \frac{2\pi kh}{qB\mu}\left(p_i - p\right) \text{ for oil} \tag{2.38}$$

$$p_D = \frac{kh\left(\frac{T_{sc}}{p_{sc}}\right)}{4\pi qT}\left(m(p_i) - m(p)\right) \text{ for gas} \tag{2.39}$$

where $m(p)$ is the pseudo-pressure defined by

$$m(p) = 2\int_{p_o}^{p} \frac{p}{\mu Z}\, dp \tag{2.40}$$

Expressing the flow rate in Mscf/d, reconciling others usual field units, we have the expression which we are familiar with

$$p_D = \frac{kh}{141.2qB\mu}(p_i - p) \text{ for oil} \tag{2.41}$$

$$p_D = \frac{kh}{1424qT}(m(p_i) - m(p)) \text{ for gas} \tag{2.42}$$

For constant bottomhole pressure constraint:

$$p_D = \frac{p_i - p}{p_i - p_{wf}} \text{ for oil} \tag{2.43}$$

$$p_D = \frac{m(p_i) - m(p)}{m(p_i) - m(p_{wf})} \text{ for gas} \tag{2.44}$$

The dimensionless time is defined in SI unit as

$$t_D = \frac{kt}{\phi\mu c_t x_f^2} = \frac{\eta t}{x_f^2} \tag{2.45}$$

where $\eta = \frac{k}{\phi\mu c_t}$

Dimensionless distances in the *x* and *y* directions are defined respectively as follows

$$x_D = \frac{x}{x_f} \tag{2.46}$$

$$y_D = \frac{y}{y_e} \tag{2.47}$$

where x_f is fracture half-length and y_e is the outer boundary perpendicular to the fracture.

The fracture conductivity is defined as

$$F_{CD} = \frac{k_f w}{k x_f} \tag{2.48}$$

The diffusivity ratios are also defined as

$$\eta_{FD} = \frac{\eta_F}{\eta} \tag{2.49}$$

$$\eta_{OD} = \frac{\eta_O}{\eta} \tag{2.50}$$

where η is the diffusivity of the inner formation, η_F and η_O are the diffusivities of the hydraulic fracture and outer formation, respectively given by

$$\eta_F = \frac{k_F}{(\phi c_t)_F \mu} \tag{2.51}$$

$$\eta_O = \frac{k_O}{(\phi c_t)_O \mu} \tag{2.52}$$

where the subscript *F* refers to the properties of hydraulic fracture, and *O* refers to the properties of outer formation.

Because of symmetry, only a quadrant of the flow domain is considered. Assuming that the linear flow exists in the reservoir and fracture system, the flow equation with dimensionless variables in outer, inner formation and fracture are given separately.

In outer formation, the diffusion equation is

$$\frac{\partial^2 p_{OD}}{\partial x_D^2} = \frac{1}{\eta_{OD}} \frac{\partial p_{OD}}{\partial t_D} \tag{2.53}$$

In inner formation, we have

$$\frac{\partial^2 p_{ID}}{\partial y_D^2} + \frac{k_O}{k} \frac{\partial p_{OD}}{\partial x_D}\bigg|_{x_D=1} = \frac{\partial p_{ID}}{\partial t_D} \tag{2.54}$$

In fracture, the expression is

$$\frac{\partial^2 p_{FD}}{\partial x_D^2} + \frac{2}{F_{CD}} \frac{\partial p_{ID}}{\partial y_D}\bigg|_{y_D=0} = \frac{1}{\eta_{FD}} \frac{\partial p_{FD}}{\partial t_D} \tag{2.55}$$

The detailed derivation, boundary conditions and solutions of the flow equations in each part are attached in Appendix B. Based on the continuity of flux at the boundaries of each part, we can connect each part and solve the pressure distribution in the whole domain.

Since non-Darcy flow effect could have an impact on the reduction of propped fracture conductivity, here we use minimum permeability plateau as derived by R.D. Barree et al. (2004) to describe the non-Darcy effect inside the fracture.

The familiar Forchheimer equation is commonly shown as

$$\frac{\partial p}{\partial L} = \frac{\mu v}{k_f} + \beta \rho v^2 \tag{2.56}$$

The second term in **Eq. 2.56** can be neglected when the fluid velocity is low. However, for high velocity flow this term becomes more important, especially for low viscosity fluids, like gas. The effective permeability can be derived from the above equation as

$$\frac{\mu v}{k_a} = \frac{\mu v}{k_f} + \beta \rho v^2 = \frac{\mu v}{k_f}\left(1 + \frac{\beta k_f \rho v}{\mu}\right) \tag{2.57}$$

The second term in the right-hand-side denominator describes a Reynolds number for porous media flow as

$$N_{\mathrm{Re}} = \frac{\beta k_f \rho v}{\mu} \tag{2.58}$$

Where β is inertial flow parameter in atm-sec^2/g.

After imposing a minimum permeability plateau, the final form of the equation becomes

$$k_a = k_f \left(k_{mr} + \frac{1 - k_{mr}}{1 + \frac{\beta k_f \rho v}{\mu}} \right) \tag{2.59}$$

This equation provides additional flexibility when the linear Forchheimer plot of $1/k_a$ versus $\rho v/\mu$ has large derivations and the apparent value of β is not constant. When k_{mr}=0, the equation is the exact representation of Forchheimer equation.

The original fracture permeability is used at first to calculate the flow rate from fracture and the pressure distribution, then compare the original permeability with the effective one. If the difference is beyond tolerance, replace the original permeability by effective one and do the calculation again. The iteration stops until the difference between those two permeability is tolerable small.

2.3.2 Fracture/Formation Thermal Model

The transient thermal model in porous media is derived from the general energy balance equation (Bird et al., 2002), the equation of change for internal energy is:

$$\frac{\partial}{\partial t}\rho\hat{U} = -\nabla\cdot\left(\rho\hat{U}\mathbf{v}\right) - p\nabla\cdot\mathbf{v} - \left(\boldsymbol{\tau}:\nabla\mathbf{v}\right) - \nabla\cdot\mathbf{q} \tag{2.60}$$

The left-hand-side of the above equation represents the accumulation rate of internal energy per unit volume; the first term in the right-hand-side represents the net rate of internal energy addition per unit volume by convection; the second term represents the reversible rate of internal energy increase per unit volume by compression; the third term represents the irreversible rate of internal energy increase per unit volume by viscous dissipation. The last term in the right-hand-side represents the rate of internal energy addition per unit volume by heat conduction.

When Fourier's law is used, and assuming that the thermal conductivity is constant in formation, the heat conduction term is presented as

$$\mathbf{q} = -K_T\nabla T \tag{2.61}$$

The bulk internal energy of fluid saturated porous media has been averaged as:

$$\rho\hat{U} = \phi\rho_f U_f + (1-\phi)\rho_r \hat{U}_r \tag{2.62}$$

where the subscript "*f*" represents fluid and "*r*" represents rock or proppant inside formation and fracture. For simplicity, the subscript "*f*" will be omitted in the following part.

For fluid flow in porous media, the term $-(\boldsymbol{\tau}:\nabla\mathbf{v})$ can be replaced by $-(\mathbf{v}\cdot\nabla p)$ (Al-Hadhrami et al., 2003). Substituting **Eq. 2.61** and **Eq. 2.62** into **Eq. 2.60**, we have

$$\frac{\partial}{\partial t}\left[\phi\rho U + (1-\phi)\rho_r \hat{U}_r\right] = -\nabla\cdot\left(\rho\hat{U}\mathbf{v}\right) - p(\nabla\cdot\mathbf{v}) - \mathbf{v}\cdot\nabla p + K_T\nabla^2 T \tag{2.63}$$

The definition of enthalpy is

$$\hat{H} = \hat{U} + p/\rho \tag{2.64}$$

Substituting **Eq. 2.64** into **Eq. 2.63**, the equation becomes:

$$\frac{\partial}{\partial t}\left[\phi\rho\hat{H} - \phi p + (1-\phi)\rho_r \hat{U}_r\right] = -\nabla\cdot\left(\rho\hat{H}\mathbf{v}\right) + K_T\nabla^2 T \tag{2.65}$$

The expression of enthalpy can be derived by using thermodynamic equilibrium

$$d\hat{H} = \hat{C}_p dT + \frac{1}{\rho}(1-\beta T)dp \tag{2.66}$$

where $\hat{C}_p$ is the specific heat at constant pressure of the fluid and β is the coefficient of thermal expansion given by

$$\beta = -\frac{1}{\rho}\left(\frac{\partial\rho}{\partial T}\right) \tag{2.67}$$

Here assuming that the density of solid is constant, the internal energy of rock and proppant can be approximated by heat capacity and temperature change only, and neglecting the density change caused by pressure. The internal energy of solid can be written as

$$d\hat{U}_r \cong d\hat{H}_r = \hat{C}_{pr} dT_r \tag{2.68}$$

Substitute **Eq. 2.68** into **Eq. 2.65**

$$\begin{aligned} &\phi\rho \frac{\partial \hat{H}}{\partial t} + \hat{H} \frac{\partial(\rho\phi)}{\partial t} - \phi \frac{\partial p}{\partial t} + \rho_r \hat{C}_{pr}(1-\phi)\frac{\partial T_r}{\partial t} + T_r \frac{\partial}{\partial t}\left[\rho_r \hat{C}_{pr}(1-\phi)\right] \\ &= -\hat{H}\nabla \cdot \rho\mathbf{v} - \rho\mathbf{v} \cdot \nabla \hat{H} + K_T \nabla^2 T \end{aligned} \tag{2.69}$$

From mass balance equation of the fluid in porous media

$$\frac{\partial}{\partial t}(\rho\phi) = -\nabla \cdot \rho\mathbf{v} \tag{2.70}$$

From mass balance equation of formation rock or fracture proppant

$$\frac{\partial}{\partial t}\left[\rho_r(1-\phi)\right] = 0 \tag{2.71}$$

Thus **Eq. 2.69** can be written as

$$\phi\rho \frac{\partial \hat{H}}{\partial t} - \phi \frac{\partial p}{\partial t} + \rho_r \hat{C}_{pr}(1-\phi)\frac{\partial T_r}{\partial t} = -\rho\mathbf{v} \cdot \nabla \hat{H} + K_T \nabla^2 T \tag{2.72}$$

For compressible fluid in porous media, thermal expansion need to be considered. Substituting **Eq. 2.66** into the above equation, we have

$$\begin{aligned} &\phi\rho \hat{C}_p \frac{\partial T}{\partial t} - \phi\beta T \frac{\partial p}{\partial t} + \rho_r \hat{C}_{pr}(1-\phi)\frac{\partial T_r}{\partial t} \\ &= -\rho\mathbf{v} \cdot \hat{C}_p \nabla T + (\beta T - 1)\mathbf{v} \cdot \nabla p + K_T \nabla^2 T \end{aligned} \tag{2.73}$$

Defining the average heat capacity and density of fluid and rock as

$$\overline{\rho C_p} = \phi\rho C_p + (1-\phi)\rho_r C_{pr} \tag{2.74}$$

Assuming that the thermal equilibrium between the formation fluid and rock/proppant can be reached instantly, we have $T=T_r$. Note that for real gas flow, residual heat in the rock causes heat transfer from the rock to the gas. This causes the measured temperature may be higher than modeling result. Based on the equilibration assumption, we have

$$\overline{\rho\hat{C}_p}\frac{\partial T}{\partial t}-\phi\beta T\frac{\partial p}{\partial t}=-\rho\mathbf{v}\cdot\hat{C}_p\nabla T+(\beta T-1)\mathbf{v}\cdot\nabla p+K_T\nabla^2 T \tag{2.75}$$

Applying Darcy's law in porous media,

$$v=-\frac{k}{\mu}\nabla p \tag{2.76}$$

Then **Eq. 2.75** becomes

$$\overline{\rho\hat{C}_p}\frac{\partial T}{\partial t}-\phi\beta T\frac{\partial p}{\partial t}=\rho\frac{k}{\mu}\cdot\hat{C}_p\nabla p\nabla T-\frac{k}{\mu}(\beta T-1)\cdot(\nabla p)^2+K_T\nabla^2 T \tag{2.77}$$

In Cartesian coordinates, since the convective heat transfer dominates over conduction in the fracture, the conduction term along the fracture in x direction can be neglected. But in the formation, the conduction term should still be considered.

In fracture:

$$\overline{\rho\hat{C}_p}\frac{\partial T_f}{\partial t}-\phi\beta T_f\frac{\partial p}{\partial t}=\frac{k_f\rho\hat{C}_p}{\mu}\frac{\partial p}{\partial x}\frac{\partial T_f}{\partial x}-\frac{(\beta T_f-1)}{\mu}k_f\left(\frac{\partial p}{\partial x}\right)^2+K_T\frac{\partial^2 T_f}{\partial y^2} \tag{2.78}$$

In inner formation:

$$\overline{\rho\hat{C}_p}\frac{\partial T}{\partial t}-\phi\beta T\frac{\partial p}{\partial t}=\frac{k\rho\hat{C}_p}{\mu}\frac{\partial p}{\partial y}\frac{\partial T}{\partial y}-\frac{(\beta T-1)}{\mu}k\left(\frac{\partial p}{\partial y}\right)^2+K_T\left(\frac{\partial^2 T}{\partial x^2}+\frac{\partial^2 T}{\partial y^2}\right) \tag{2.79}$$

In outer formation:

$$\overline{\rho\hat{C}_p}\frac{\partial T}{\partial t}-\phi\beta T\frac{\partial p}{\partial t}=\frac{k\rho\hat{C}_p}{\mu}\frac{\partial p}{\partial x}\frac{\partial T}{\partial x}-\frac{(\beta T-1)}{\mu}k\left(\frac{\partial p}{\partial x}\right)^2+K_T\left(\frac{\partial^2 T}{\partial x^2}+\frac{\partial^2 T}{\partial y^2}\right) \tag{2.80}$$

The initial and boundary conditions are given below.

$$T=T_i \text{ at } t=0 \tag{2.81}$$

$$\left.\frac{\partial T}{\partial y}\right|_{y=y_e}=0 \text{ at } y=y_e \tag{2.82}$$

$$T=T_f \text{ at } y=0 \tag{2.83}$$

$$T = T_i \text{ at } x = x_e \tag{2.84}$$

$$-K_T \left.\frac{\partial T}{\partial x}\right|_{X=r_{wb}} = U_T\left(T_w - T\right) \text{ at } x = r_w \tag{2.85}$$

where T_f and T_w are the fluid temperature in the fracture and the wellbore, U_T is the overall heat transfer coefficient determined by the material property and the structure of wellbore. The fracture and formation thermal models are coupled by the continuity of temperature at the boundaries.

This 2D model ignores the pressure and thermal change happening in vertical direction. The initial temperature condition is geothermal temperature calculated according to the wellbore trajectory. The inner boundary considers heat exchange between the wellbore and the near-wellbore formation.

The above equations are solved for temperature and pressure profiles. As mentioned before, the pressure equations are solved by Laplace transform with a semi-analytical solution. The temperature equations are solved semi-analytically only for infinite fracture conductivity case, and the general case can be solved numerically. The semi-analytical approach can be used to validate the numerical work, also it could be used to separate different physical processes to evaluate the influence of each part.

2.3.3 Semi-analytical Approach for the Thermal Model

Operator splitting is a method to investigate complex models. The idea is to decouple a complex equation system into a sequence of simple tasks representing simple physical processes. Different sub-problems could be solved independently with different methods and this would affect the accuracy and stability of the overall results.

The operator splitting method is flexible to solve a partial differential equation contains convection, diffusion and 'forcing' terms (terms related to pressure gradient) since the decomposition would allow different solution techniques to the different physical processes. Obinna (2008) applied this method to solve the reservoir temperature model in 1D cylindrical coordinate system and test the method with field data to infer flow rate and estimate reservoir parameters.

In this study, it is feasible to apply this method to solve the formation thermal model. Starting with a simplified model in which we have the following assumptions:

- The fracture has infinite conductivity. There is no pressure difference along the fracture. The fluid flow coming from the formation is uniformly distributed along fracture.
- Linear flow in the inner formation. The outer formation fluid flow and temperature change can be neglected.
- Constant flow rate constraint at the wellbore.
- Darcy's law applies.

Solution of the Convection and 'Forcing' Equation

The convectional term (the first term in the right-hand side of **Eq. 2.75)** is caused by the fluid flow, which is a function of velocity and thermal properties of fluid and porous media. The 'forcing' term (the second terms in the left-hand side and the right-hand side of **Eq. 2.75)** contains the fluid expansion or compression and viscous dissipation, which 'generate' heat. For real gas case, Joule-Thomson effect is cooling at the reservoir condition. The expression for the convection and 'forcing' part of the inner formation model can be expressed as

$$\overline{\rho\hat{C}_p}\frac{\partial T}{\partial t}-\phi\beta T\frac{\partial p}{\partial t}=\frac{k\rho\hat{C}_p}{\mu}\frac{\partial p}{\partial y}\frac{\partial T}{\partial y}-\frac{(\beta T-1)}{\mu}k\left(\frac{\partial p}{\partial y}\right)^2 \tag{2.86}$$

Put the terms containing temperature on the left hand side and the others on the right-hand side, the above equation can be written as

$$\frac{\partial T}{\partial t}-\frac{k\rho\hat{C}_p}{\mu\overline{\rho\hat{C}_p}}\frac{\partial p}{\partial y}\frac{\partial T}{\partial y}=\frac{\phi\beta T}{\overline{\rho\hat{C}_p}}\frac{\partial p}{\partial t}-\frac{(\beta T-1)}{\mu\overline{\rho\hat{C}_p}}k\left(\frac{\partial p}{\partial y}\right)^2 \tag{2.87}$$

This convection and 'forcing' part can be solved using the Method of Characteristics. The characteristic curve can be described by defining the characteristic coordinates, a moving coordinate system, and the solution of the above equation can be obtained along the trajectories of the characteristic curves. The equation which describes the characteristic curve can be written as

$$\frac{dy}{dt}=-\frac{k\rho\hat{C}_p}{\mu\overline{\rho\hat{C}_p}}\frac{\partial p(t,y)}{\partial y}=\frac{\rho\hat{C}_p}{\overline{\rho\hat{C}_p}}v(t,y) \tag{2.88}$$

where $v(t,y)$ is the fluid velocity at time t and location y.

Since $v(t,y)=-q(t)/(4x_f h)$, where $q(t)$ is the flow rate,

$$\frac{dy}{dt}=\frac{\rho\hat{C}_p}{\overline{\rho\hat{C}_p}}v(t,y)=-\frac{\rho\hat{C}_p}{\overline{\rho\hat{C}_p}}\frac{q(t)}{4x_f h} \tag{2.89}$$

The integration of the above equation gives:

$$\int_{y_0}^{y}dy=-\int_0^t\frac{\rho\hat{C}_p}{\overline{\rho\hat{C}_p}}\frac{q(t)}{4x_f h}dt \tag{2.90}$$

$$y-y_0=-\int_0^t\frac{\rho\hat{C}_p}{\overline{\rho\hat{C}_p}}\frac{q(t)}{4x_f h}dt \tag{2.91}$$

For constant flow rate, the solution is

$$y = y_0 - \frac{\rho\hat{C}_p}{\overline{\rho\hat{C}_p}} \frac{q}{4x_f h} t \tag{2.92}$$

Setting $\xi = y_0$ and $\tau = t$ for the new coordinate system (τ, ξ), the characteristic curves of the heat convection equation can be written as

$$\xi = y + \frac{\rho\hat{C}_p}{\overline{\rho\hat{C}_p}} \frac{q}{4x_f h} \tau \tag{2.93}$$

Let $\tilde{T}(\tau, \xi) = T(t, y)$ for the purpose of getting temperature values on the characteristic curves, $\tilde{T}$ and T are the same function but on the two different coordinates system. **Eq. 2.87** in the new coordinates system can be written as

$$\frac{\partial \tilde{T}}{\partial \tau} = \left(\frac{\phi\beta}{\overline{\rho\hat{C}_p}} \frac{\partial p}{\partial t} - \frac{\beta k}{\mu \overline{\rho\hat{C}_p}} \left(\frac{\partial p}{\partial y} \right)^2 \right) \tilde{T}(\tau, \xi) + \frac{k}{\mu \overline{\rho\hat{C}_p}} \left(\frac{\partial p}{\partial y} \right)^2 \tag{2.94}$$

Group the parameters in the above equation, we have

$$\frac{\partial \tilde{T}}{\partial \tau} = M\tilde{T}(\tau, \xi) + G \tag{2.95}$$

where

$$M = \frac{\phi\beta}{\overline{\rho\hat{C}_p}} \frac{\partial p}{\partial t} - \frac{\beta k}{\mu \overline{\rho\hat{C}_p}} \left(\frac{\partial p}{\partial y} \right)^2 \tag{2.96}$$

$$G = \frac{k}{\mu \overline{\rho\hat{C}_p}} \left(\frac{\partial p}{\partial y} \right)^2 \tag{2.97}$$

Integrating factors are used for solving **Eq. 2.95**, we get

$$\frac{d}{d\tau} \left(\tilde{T} e^{\int -M d\tau} \right) = G(\tau, y(\tau)) e^{\int -M d\tau} \tag{2.98}$$

For the initial condition $\tilde{T}(\tau_0, \xi) = \tilde{T}_0$, and defining $F(\tau) = \int M d\tau$, then the equation becomes:

$$\tilde{T}e^{-F(\tau)} - \tilde{T}_0 e^{-F(0)} = \int_{\tau_0}^{\tau} G(s, y(s)) e^{-F(s)} ds \tag{2.99}$$

$$\tilde{T}(\tau, \xi) = \tilde{T}_0 e^{(F(\tau)-F(0))} + \int_{\tau_0}^{\tau} G\left(s, \xi - \frac{\rho\hat{C}_p}{\overline{\rho\hat{C}_p}} \frac{q}{4x_f h} s \right) e^{(F(\tau)-F(s))} ds \tag{2.100}$$

In terms of the original system variables, $\tilde{T}_0 = T_0\left(y + \frac{\rho\hat{C}_p}{\overline{\rho\hat{C}_p}} \frac{q}{4x_f h} t \right) = T_0$

$$T(t, y) = T_0 e^{(F(t)-F(0))} + \int_0^t G\left(s, y + \frac{\rho\hat{C}_p}{\overline{\rho\hat{C}_p}} \frac{q}{4x_f h}(t-s) \right) e^{(F(t)-F(s))} ds \tag{2.101}$$

where

$$F(t) = \int M dt = \int \left(\frac{\phi\beta}{\overline{\rho\hat{C}_p}} \frac{\partial p}{\partial t} - \frac{\beta k}{\mu \overline{\rho\hat{C}_p}} \left(\frac{\partial p}{\partial y} \right)^2 \right) dt \tag{2.102}$$

Also in this linear flow system, the relationship between velocity and flow rate is shown as

$$v = -\frac{k}{\mu}\frac{\partial p}{\partial y} = -\frac{q}{4x_f h} \tag{2.103}$$

Replace the velocity expression in *G* function

$$G = \frac{k}{\mu \overline{\rho\hat{C}_p}} \left(\frac{\partial p}{\partial y} \right)^2 = \frac{\mu}{k \overline{\rho\hat{C}_p}} \frac{q^2}{(4x_f h)^2} \tag{2.104}$$

So

$$\begin{aligned} &\int_0^t G\left(s, y + \frac{\rho\hat{C}_p}{\overline{\rho\hat{C}_p}} \frac{q}{4x_f h}(t-s) \right) e^{(F(t)-F(s))} ds \\ &= \int_0^t \frac{k}{\mu \overline{\rho\hat{C}_p}} \left(\frac{\partial p}{\partial y} \right)^2 e^{(F(t)-F(s))} ds = \int_0^t \frac{\mu}{k \overline{\rho\hat{C}_p}} \frac{q^2}{(4x_f h)^2} e^{(F(t)-F(s))} ds \end{aligned} \tag{2.105}$$

The final solution of the convection and ‘forcing’ equation is:

$$T_{conv}(t,y) = T_0 e^{(F(t)-F(0))} + \int_0^t \frac{\mu}{k\overline{\overline{\rho\hat{C}_p}}} \frac{q^2}{(4x_f h)^2} e^{(F(t)-F(s))} ds \tag{2.106}$$

Solution of the Conduction Equation

For the heat conduction part, since we assume that the temperature in the outer formation part would be the geothermal temperature, the heat conduction would also occur in the direction perpendicular to the flow direction. Here we derive a 2D conduction model. The diffusion equation is

$$\frac{\partial T}{\partial t} = K_T \nabla^2 T = K_T \left(\frac{\partial^2 T}{\partial y^2} + \frac{\partial^2 T}{\partial x^2} \right) \tag{2.107}$$

The initial condition is the temperature distribution obtained from convection and 'forcing' part.

$$T(x,y,0) = T_i(x,y) = F(x,y) \tag{2.108}$$

Boundary conditions are as follows:

$$\left. \frac{\partial T}{\partial x} \right|_{x=0} = 0 \tag{2.109}$$

$$\left. \frac{\partial T}{\partial x} \right|_{y=0} = 0 \tag{2.110}$$

$$T\big|_{x=x_f} = T_i \tag{2.111}$$

$$T\big|_{y=y_e} = T_i \tag{2.112}$$

By using the method of separate variables:

$$T(x,t) = \Gamma(t) X(x) Y(y) \tag{2.113}$$

$$\frac{1}{\alpha} \frac{d\Gamma/dt}{\Gamma} = \frac{d^2X/dx^2}{X} + \frac{d^2Y/dy^2}{Y} \tag{2.114}$$

Formulate the eigenvalue problems in x and y directions separately:

$$\frac{d^2X}{dx^2} + \mu^2 X = 0 \tag{2.115}$$

$$\left.\frac{\partial X}{\partial x}\right|_{x=0} = 0 \tag{2.116}$$

$$X\big|_{x=x_f} = T_i \tag{2.117}$$

The x- eigenfunctions are

$$X_m(x) = A_m \cos(\mu_m x) \tag{2.118}$$

where $\cos(\mu_m x_f) = 0$

In y- direction, it follows the same solution procedure.

$$\frac{d^2Y}{dy^2} + v^2 Y = 0 \tag{2.119}$$

$$\left.\frac{\partial Y}{\partial y}\right|_{y=0} = 0 \tag{2.120}$$

$$Y\big|_{y=y_e} = T_i \tag{2.121}$$

The y- eigenfunctions are

$$Y_n(y) = B_n \cos(v_n y) \tag{2.122}$$

where $\cos(v_n y_e) = 0$

Then for the transient term

$$\frac{d\Gamma}{dt} + \alpha\left(\mu_m^2 + v_n^2\right)\Gamma = 0 \tag{2.123}$$

$$\Gamma(t) = C_{mn} e^{-\left(\mu_m^2 + v_n^2\right)\alpha t} \tag{2.124}$$

The solution is expressed in a double-infinite series:

$$T_{cond}(x,y,t)=\sum_{m=1}^{\infty}\sum_{n=1}^{\infty}D_{mn}e^{-\left(\mu_m^2+v_n^2\right)\alpha t}\cos(\mu_m x)\cos(v_n y) \tag{2.125}$$

The initial condition is

$$F(x,y)=\sum_{m=1}^{\infty}\sum_{n=1}^{\infty}D_{mn}\cos(\mu_m x)\cos(v_n y) \tag{2.126}$$

After applying the orthogonality of the eigenfunctions, we could obtain

$$\begin{aligned} D_{mn} &= \frac{\int_{y=0}^{y_e}\int_{x=0}^{x_f}F(x,y)\cos(\mu_m x)\cos(v_n y)dxdy}{\left(\int_{x=0}^{x_f}\cos^2(\mu_m x)dx\right)\left(\int_{y=0}^{y_e}\cos^2(v_n y)dy\right)} \\ &= \frac{4}{x_f y_e}\int_{y=0}^{y_e}\int_{x=0}^{x_f}F(x,y)\cos(\mu_m x)\cos(v_n y)dxdy \end{aligned} \tag{2.127}$$

Combined Solution by Operator Splitting

Here operator splitting algorithm is used to combine the convection 'forcing' and conduction part and get the final solution of the energy balance equation in inner formation.

The solution procedure is shown in **Fig. 2.3**. At each time step, solve the hyperbolic convection part first to get the convective temperature distribution, and then use this temperature distribution as an initial condition to solve the diffusion part at the same time step. The procedure continues until the last time step.

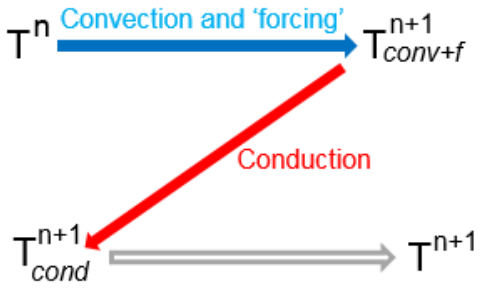

Fig. 2.3– Procedure of operator splitting to solve inner formation temperature.

For $t \in \left(t^n, t^{n+1}\right)$, the heat convection solution is

$$T_{conv}\left(t^{n+1}, y\right) = T_0 e^{\left(F\left(t^{n+1}\right) - F\left(t^n\right)\right)} + \int_0^{t^{n+1}} \frac{\mu}{k\rho\hat{C}_p} \frac{q^2}{\left(4x_f h\right)^2} e^{\left(F\left(t^{n+1}\right) - F(s)\right)} ds \qquad (2.128)$$

At the same time step, the diffusion part is solved as

$$T_{cond}\left(x, y, t^{n+1}\right) = \sum_{m=1}^{\infty}\sum_{n=1}^{\infty} D_{mn} e^{-\left(\mu_m^2 + v_n^2\right)\alpha\left(t^{n+1} - t^n\right)} \cos\left(\mu_m x\right)\cos\left(v_n y\right) \qquad (2.129)$$

For accuracy consideration, it is suggested to use relatively small steps for integration. On the other hand, stability consideration demands a moderate time interval. In this study we use one day as the time interval, and the space gridding is the same as finite difference method. For gas case, the fluid properties such as viscosity, density and heat capacity depend on both pressure and temperature, which will cause inaccuracy for the results. Since the temperature variation is in a relatively small range compared with initial reservoir temperature, this inaccuracy is acceptable in current study for the purpose of understanding. For the demand of higher level accuracy, fully numerical method is recommended.

2.4 Solution Procedure

After developing the wellbore and fracture model, we couple them together to solve the transient pressure and temperature distribution in fracture, formation, and along the wellbore. It should be noted that besides the equations we presented above, some fluid property correlations are also employed to close the equation system. To solve the coupled model, there are two major steps, which are shown as different sections in the following program flow chart **Fig. 2.4**.

First the initial pressure and temperature are given to the fracture, formation and wellbore uniformly. For further study of field cases, we can initialize the pressure and temperature fields by applying the distribution from fracture treatment and later warm back model, which would be continuous with the production period. At the n^{th} time step, we first solve the fracture/formation flow model, then the wellbore mass and momentum model to make sure the pressure is converged along wellbore with inflow from fracture. Then the fracture/formation energy balance would be solved. We assume constant overall heat transfer coefficient between wellbore and formation.

The arriving temperature at the intersection of fracture and wellbore is the inflow fluid temperature for wellbore model, and we can solve the 1D wellbore thermal model. Then we update the pressure and temperature fields and go to the next time step. For each time step, the fluid properties are calculated based on the pressure and temperature in the last time step.

For the fracture/formation flow model, we use the Laplace transform method and finite difference method to solve the wellbore flow model and two thermal models. Note that we only solve one quarter of the formation and consider the formation as symmetric at the two sides of fracture and wellbore. In order to better couple the fracture/formation model with the wellbore model, the gridding of all the models is the same along the horizontal wellbore direction so that the arriving pressure and temperature can be directly used without interpolation.

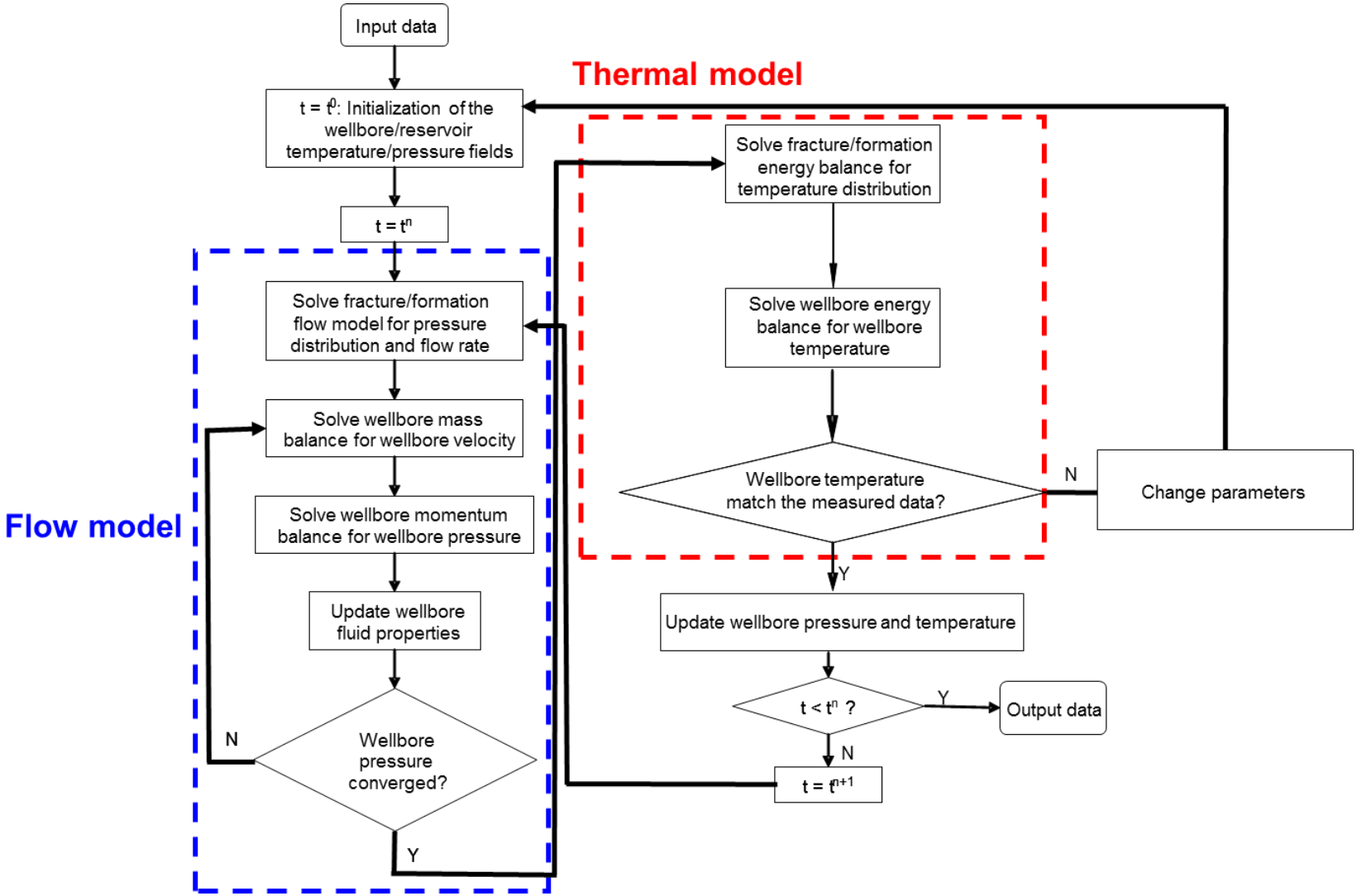

Fig. 2.4– Work flow of the solution procedure.

Non-Darcy function modifying permeability is a function of fluid velocity and it is calculated by iteration as **Fig. 2.5** shows.

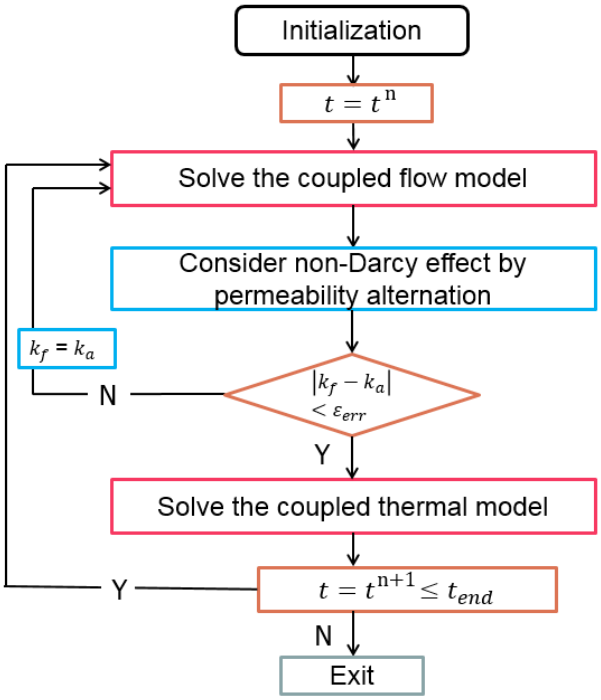

Fig. 2.5– Work flow considering Non-Darcy flow.

2.5 Model Validation

In this section, we will validate the fracture/formation and wellbore model. For the fracture/formation trilinear flow model, it has been validated by Lee and Brockenbrough (1986), and has a good production data matching comparing with published field data in shale reservoirs (Meyer, 2010). For the wellbore flow and thermal model, Yoshioka (2007) validated the model in the previous work. Here we mainly focus on the validation of the fracture/formation thermal model by comparing the semi-analytical solution with finite difference method results, and validate the computation with other models.

2.5.1 Compare Formation Thermal Model with Semi-Analytical Solution

The semi-analytical solution is a simplified method to solve the formation temperature for 1D linear flow in porous media. Here for the model validation, we assume an infinite fracture conductivity, so there is no pressure drop along the fracture, and the flow rate at the fracture interface is uniform. Since the outer formation has subtle contribution to the production, we only consider the linear flow from the inner formation to the fracture. The fracture geometry and the flow pattern in the inner formation are shown in **Fig. 2.6** and **Fig. 2.7**. **Table 2.1** lists the primary parameters in the calculation, and **Table 2.2** is the rock and fluid properties.

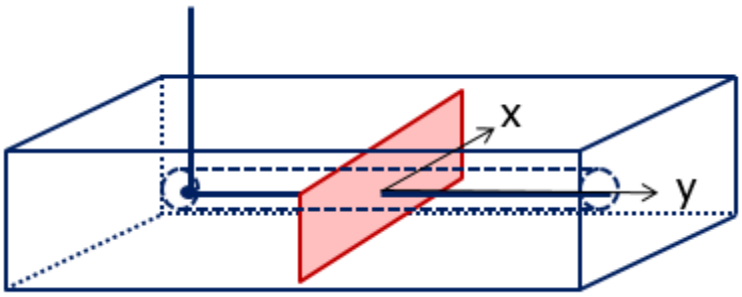

Fig. 2.6– Fracture geometry in 3D.

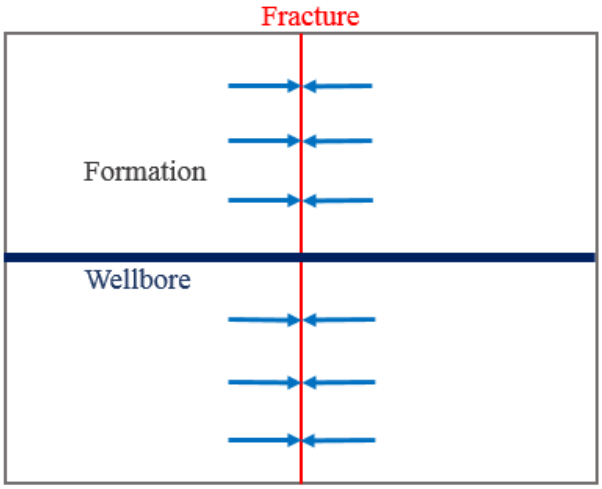

Fig. 2.7– Fracture geometry in 2D and the linear flow pattern in formation.

Table 2.1– Key parameters for comparison with semi-analytical solution.

Formation		Fracture	
Net Pay Thickness, ft	160	Fracture width, in	0.24
Permeability, nD	580	Fracture permeability, Darcy	1000
Porosity, %	5.0	Fracture porosity, %	0.2
Pore pressure, psi	5000	Fracture half-length, ft	300
Initial temperature, °F	238.37		
Reservoir compressibility, 1/psi	2.0E-04		

Table 2.2– Fluid and rock properties

Rock	Bulk density, lb/ft^3	148.57
	Compressibility, 1/psi	1.00E-06
	Thermal conductivity, Btu/(hr-ft-°F)	2.0
	Specific heat, Btu/(lb-°F)	0.202
Gas	Specific heat, Btu/(lb-°F)	0.735
	Molecular weight	16
	Thermal conductivity, Btu/(hr-ft-°F)	1.50E-04
	Critical pressure, psi	667.17
	Critical temperature, °F	-116.66

Figure 2.8 shows the arriving temperature at the fracture interface by constant flow rate constraint 200 Mscf/d/frac at the wellbore for 40 days. Since the fluid velocity does not change with time, the convection/conduction ratio keeps as a constant during the production, which means the heating provided by conduction is constant. The reason of the temperature decreasing is Joule-Thomson cooling effect for gas expansion as a result of the pressure decline. The finite difference result is in good agreement with semi-analytical solution.

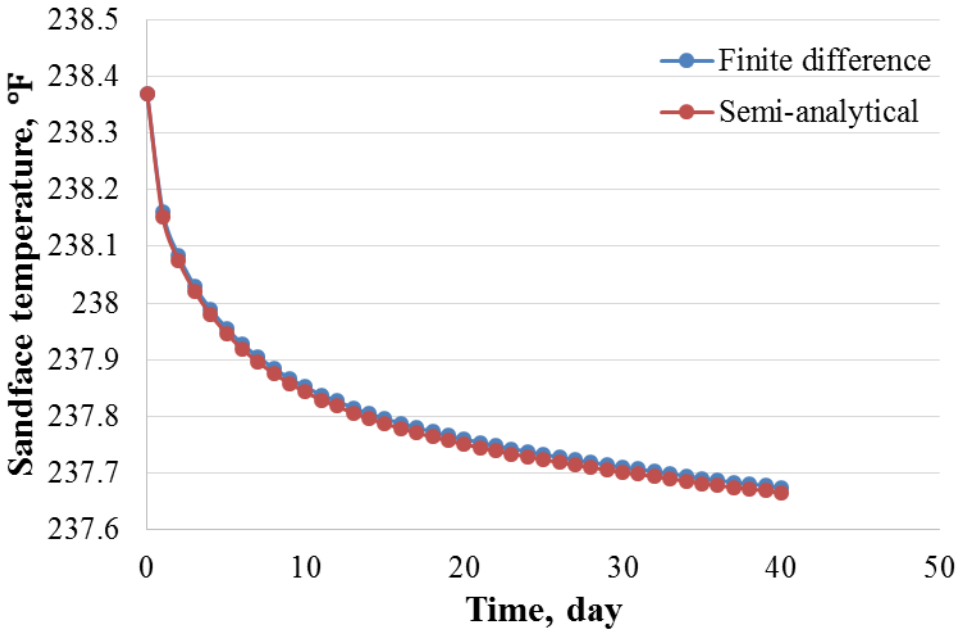

Fig. 2.8– Comparison of the arriving temperature at the fracture interface with semi-analytical solution.

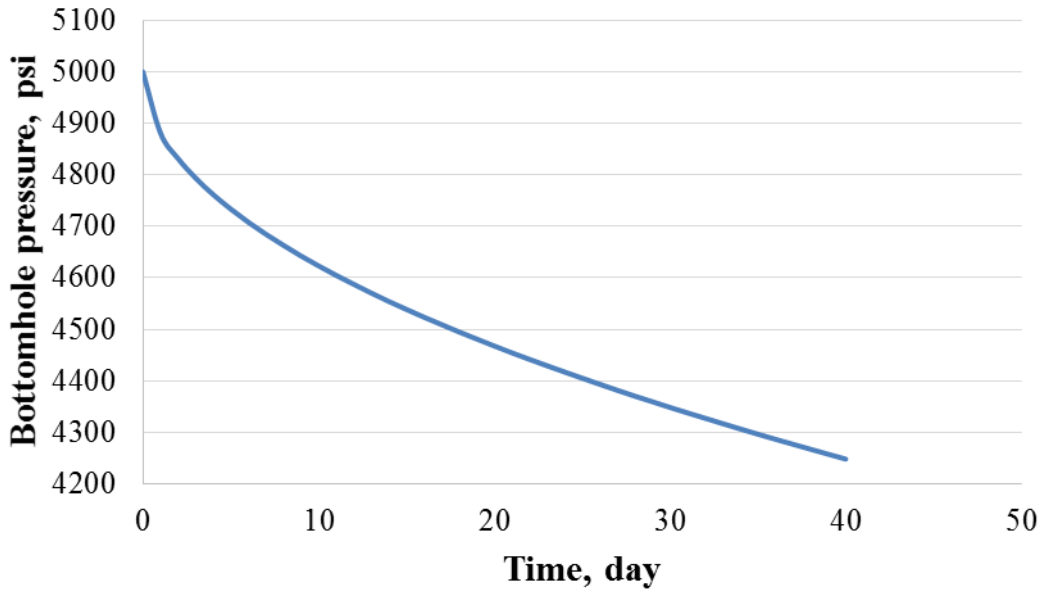

Fig. 2.9– Transient pressure behavior during constant flow rate production.

2.5.2 Compare Fracture/Formation Model with Fully Numerical Solution

To validate the established fracture/formation model, we compare the results with the fully numerical solutions by Yoshida (2014). In his previous model, he considers the radical flow caused by fluid convergence near the wellbore, by replacing that with linear flow pattern, we could compare our results under the same condition. **Fig. 2.10** shows the single fracture geometry.

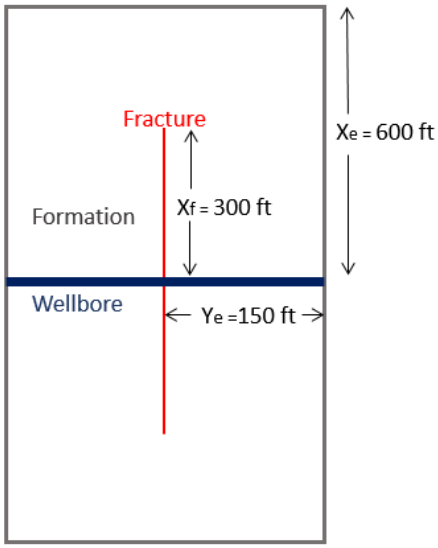

Fig. 2.10– Fracture geometry in numerical simulation.

Table 2.3–Key parameters for comparison with fully numerical simulation.

Formation		Fracture	
Net Pay Thickness, ft	160	Fracture width, in	0.24
Permeability, nD	580	Fracture permeability, Darcy	1
Porosity, %	4.2	Fracture porosity, %	0.2
Pore pressure, psi	4500	Fracture half-length, ft	300
Initial temperature, °F	238.37		
Reservoir compressibility, 1/psi	1.90E-04		
Bottomhole pressure, psi	2600		

For long-term production, we set the bottomhole pressure equal to 2600 psi as constant. **Table 2.3** lists the primary parameters used for the comparison with fully numerical model. The fracture conductivity is 20 md-ft so that the pressure change inside fracture need to be considered.

Figure 2.11 shows the comparison result of the pressure distribution along the fracture direction at different production days. The fracture half-length is 300 ft, from 300 ft to 600 ft is the outer formation. **Fig. 2.12** shows the flow rate history match. As the flow rate declines with time, the pressure gradient inside fracture becomes smaller and smaller. The pressure distribution inside the fracture is in good agreement with the fully numerical solution, but in the outer formation, the semi-analytical solution disperses faster than the numerical solution because it is linear flow pattern in semi-analytical method while radical flow convergence is considered at fracture tip in numerical simulation. Since the outer formation pressure behavior has relative small influence on the arriving temperature at the wellbore, this difference is acceptable.

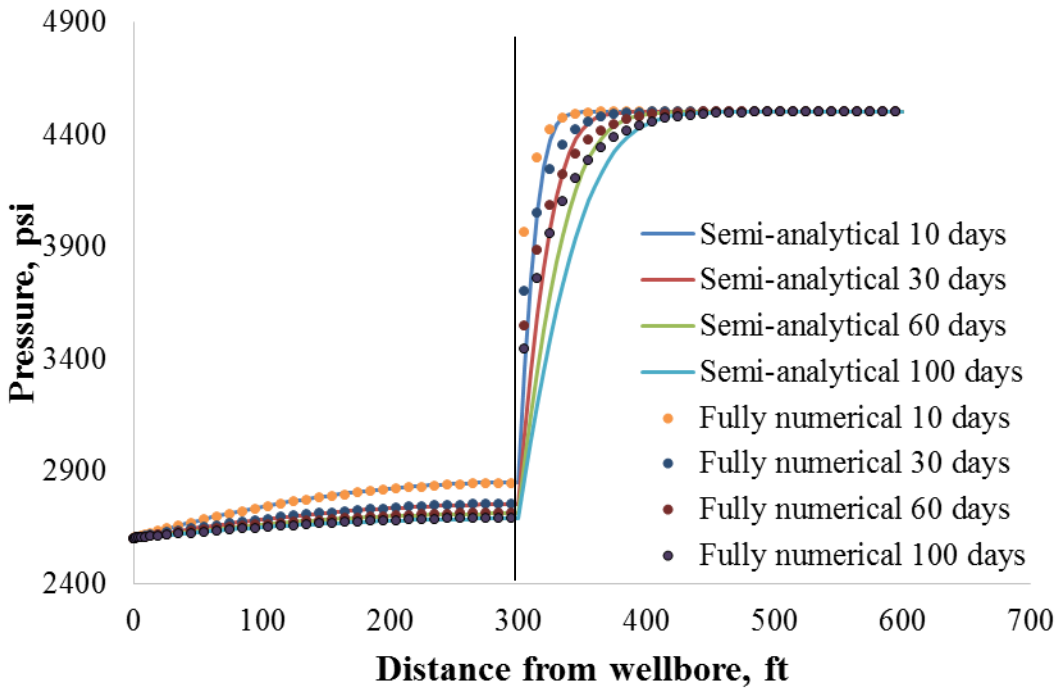

Fig. 2.11– Comparison of pressure distribution along fracture direction.

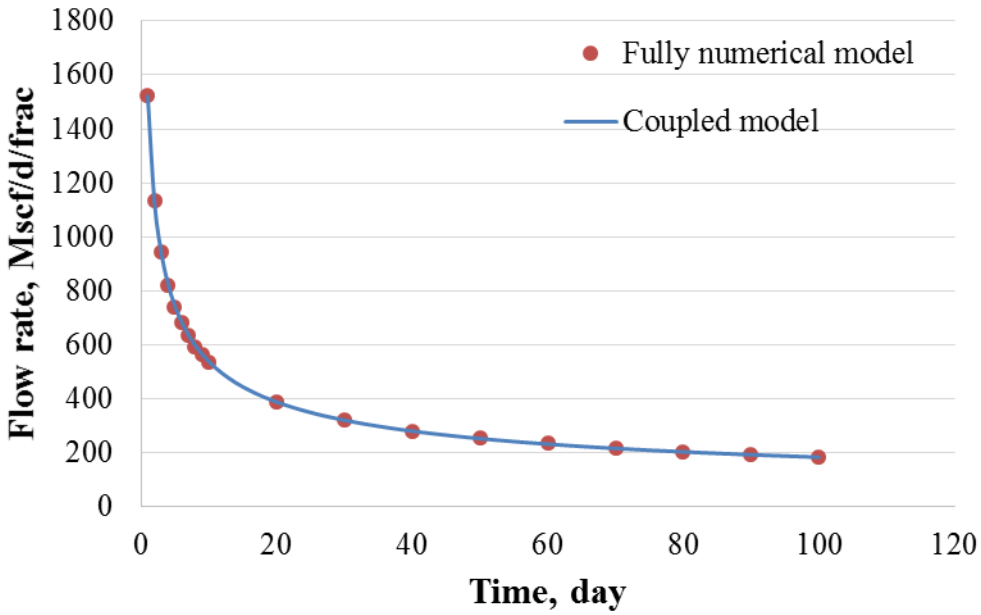

Fig. 2.12– Comparison of flow rate decline with production time.

Figure 2.13 compares the temperature distribution along the fracture direction at different production days. Since the porosity and fluid velocity is much larger in the fracture than the formation, the convection and Joule-Thomson cooling effect would dominate the heat transfer process in fracture. At the beginning of production, dramatic temperature drop happens inside fracture due to the large flow rate and pressure drop, then the temperature gradient becomes flatter as a result of flow rate decline.

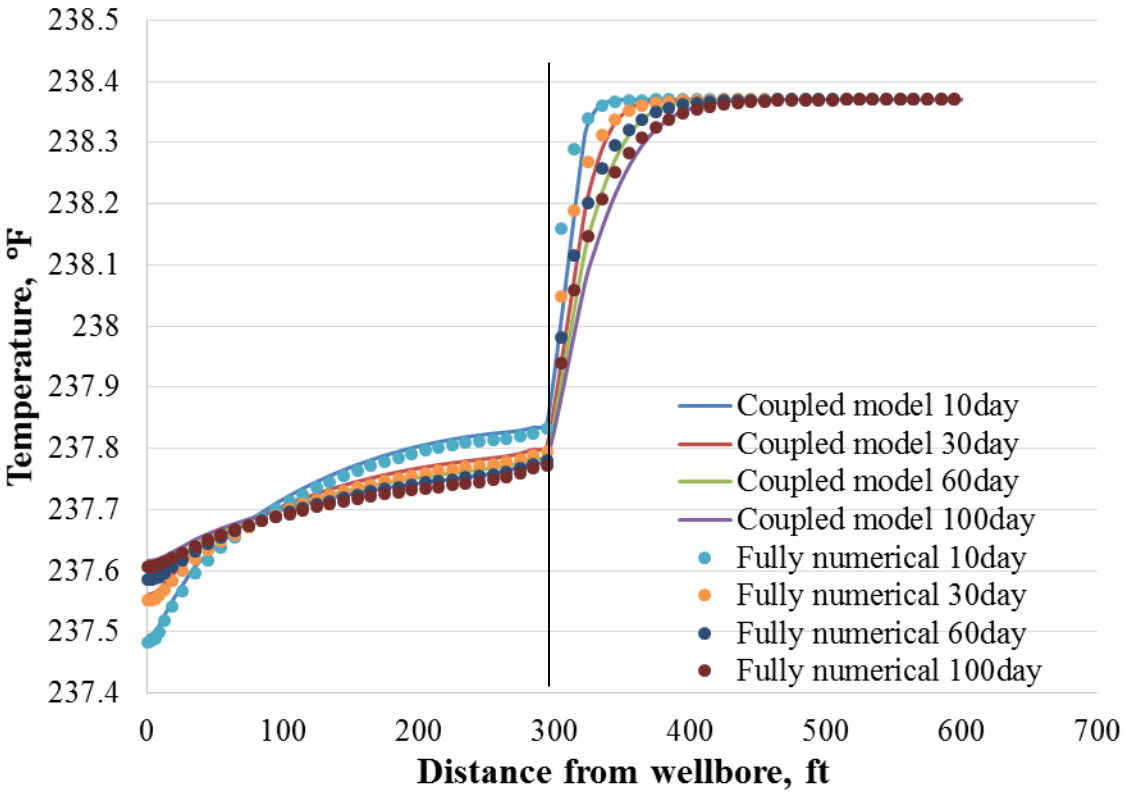

Fig. 2.13– Comparison of temperature distribution with production time.

2.5.3 Compare Wellbore Model with Hasan & Kabir Solution

For wells producing gas and liquid, the heat transfer between the wellbore and the formation at a given flow rate could be described by the general energy balance as the following. **Fig. 2.14** illustrates the control volume in wellbore.

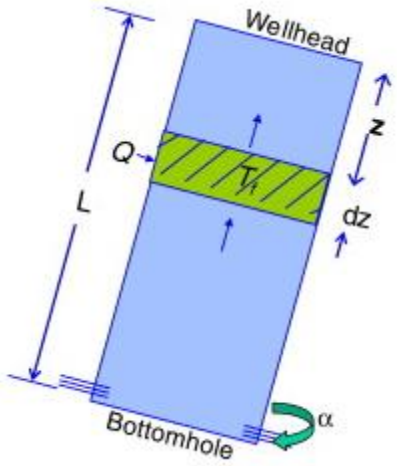

Fig. 2.14– Energy balance for wellbore fluid.

For the production well, the energy balance equation first presented by Ramey (1962) can be written as

$$\frac{dH}{dz}+\frac{g\sin\alpha}{Jg_c}+\frac{v}{Jg_c}\frac{dv}{dz}=-\frac{Q}{w} \tag{2.130}$$

where g_c and J are unit conversion factors, w is the mass flow rate of fluid, α is the inclined angle of the tubing to the horizontal direction and z is positive in the downward direction. H is fluid enthalpy and Q is heat rate. Inside the control volume of the length dz, the first term in the left-hand-side of **Eq. 2.130** represents the heat transfer by convection, the second and third term represent potential and kinetic energies separately. The right-hand-side term is heat conduction from formation to the element.

The assumptions in the wellbore energy balance model are:

- Single- or two- phase system.
- There is no heat transfer caused by phase change, such as evaporation/condensation.
- The solution and mixing phenomena are negligible.

For the steady state, single phase gas solution at low pressure, the expression presented by Hasan and Kabir (1994) can be written as:

$$T_f = T_{ei} + \frac{1 - e^{(z-L)L_R}}{L_R}\left(g_G \sin\alpha - \frac{g\sin\alpha}{c_p J g_c}\right) \tag{2.131}$$

where L_R is the relaxation distance parameter, which is given by

$$L_R = \frac{2\pi}{c_p w}\left(\frac{1}{\frac{1}{r_{to}U_{to}} + \frac{T_D}{k_e}}\right) \tag{2.132}$$

$$t_D = \frac{k_e t}{\rho_e c_e r_w^2} \tag{2.133}$$

$$T_D = \ln\left[e^{-0.2t_D} + \left(1.5 - 0.3719e^{-t_D}\right)\sqrt{t_D}\right] \tag{2.134}$$

In **Eq. 2.132**, U_{to} is the overall heat transfer coefficient which can be considered as a constant or calculated according to the wellbore structure under steady state, r_{to} is outside radius of tubing, k_e is thermal conductivity of formation, and T_D is dimensionless temperature in terms of dimensionless time t_D. ρ_e and c_e are formation density and heat capacity.

Considering a vertical wellbore, and the gas flow rate into the wellbore at 4000 m is 2.0 MMscf/d. We use both our transient wellbore model and the Hasan & Kabir model to calculate the fluid temperature along the wellbore. Compared with Hasan & Kabir model, our wellbore thermal model contains the Joule-Thomson effect inside wellbore. In order to compare the results under the same condition, here we neglect the term considering Joule-Thomson effect and run the wellbore model for 100 days to approximate a steady state solution. The parameters used in the comparison are listed in **Table 2.4**.

Table 2.4– Key parameters for comparison with Hasan & Kabir model.

Bottomhole pressure, psi	3000
Formation thermal conductivity, Btu/(hr-ft-°F)	2.15
Cement thermal conductivity, Btu/(hr-ft-°F)	2
Heat capacity of gas, Btu/(lb-°F)	0.78
Formation thermal diffusivity, ft/sec2	0.04
g, ft/sec2	32.174
Geothermal gradient, °F /ft	0.015
Conversion factor J	778
Casing thermal conductivity, Btu/(hr-ft-°F)	26
Tubing thermal conductivity, Btu/(hr-ft-°F)	26
Tubing I.D, in	3.8
Tubing O.D, in	6
Cement O.D, in	12
Casing I.D, in	8.681
Casing O.D, in	9.625

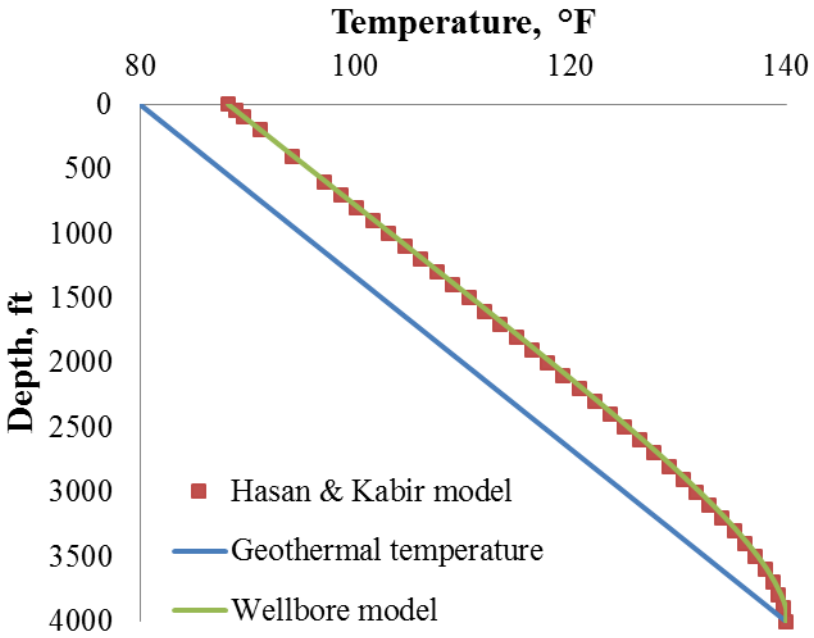

Fig. 2.15– Comparison of wellbore temperature with Hasan & Kabir model.

In **Fig. 2.15**, the blue line is the geothermal temperature, the red dots are Hasan & Kabir solution and the green line is the solution after 100 days from transient wellbore model. For constant flow rate, the wellbore temperature can be considered as steady state after 100 days. The transient model has good agreement with Hasan & Kabir Model. The difference between geothermal temperature and wellbore fluid temperature is getting bigger upwards to the surface.

2.6 Section Summary

This Section introduces the methodology for the modeling, which includes a trilinear flow model and a thermal model in porous media, and balance equations in wellbore. The semi-analytical solution of the transient formation thermal model is developed for the understanding of the heat transfer process while the finite difference solution could handle the general cases. The solution procedure explains how to couple the wellbore model with the fracture/formation model. The formation thermal model is validated by the comparison with the semi-analytical solution under constant production rate. The computation of the coupled formation/fracture model is validated by the comparison with a fully numerical simulation, and the wellbore model is validated by comparing with Hasan & Kabir solution.

3 RESULTS AND DISCUSSION*

This section focuses on the result analysis based on the model, highlighting the transient temperature behavior under constant flow rate and constant bottomhole pressure constraints, the influence of non-uniform fractures on gas production rate distribution and the temperature behavior along the horizontal wellbore during long-term production.

3.1 Introduction

The transient temperature behavior is determined by the production rate history, the pressure drawdown in the reservoir, and the thermal properties of fluid and formation. Many parameters are presented in the model formulation, and the uncertainties of their values is challenging for further analysis and application in field. Among these variables, some variables can be estimated within an acceptable certainty range by other tools. For example, we could obtain formation porosity by well logging, formation permeability and thermal conductivity by laboratory core test, and height of the pay zone by geological methods. The primary purpose of this study is to interpret flow profile from temperature data, thus diagnose the efficiency of each hydraulic fracture stage. Besides, we try to evaluate the influence of key parameters on flow rate and measured temperature at the wellbore. This work may help us to reduce the uncertainties of the parameters when combined with other testing methods. Here we run both constant flow rate and constant

* Reproduced with permission from "Diagnosis of Multiple Fracture Stimulation in Horizontal Wells by Downhole Temperature Measurements" by J. Cui, and D. Zhu. Paper IPTC 17700 presented at the International Petroleum Technology Conference in Doha, Qatar, 20-22 January. Copyright 2014 by the International Petroleum Technology Conference.

bottomhole pressure cases to analyze the transient thermal behavior and key parameters, such as fracture half-length and conductivity.

3.2 Constant Flow Rate Cases

For fractured horizontal wells, the field usually conduct constant bottomhole pressure at the wellbore during long-term period production. At the very beginning, it takes days or even months to let the fracturing fluid flow back, and then gas production will start and be stabilized. The bottomhole pressure decreases gradually to the designated value during this period. Before the production begins, if the shut-in time is short, the fracturing fluid remaining in the fracture and the near-by formation would still be cooler than the reservoir temperature, thus the warmback or flowback process influences the initial temperature distribution for modeling. Here we assume that the shut in time is long enough so that it is geothermal temperature in reservoir, and we use a constant flow rate condition for the modeling to mimic the beginning production.

The geometry of fracture we set is as **Fig. 2.10** shows. The constant flow rate for single fracture is 150 Mscf/day. Considering 16 identical fractures along a 4800 ft long horizontal section of the well, the total production rate would be 2.4 MMscf/day, which is reasonable at the beginning of the production in shale reservoir like Marcellus Shale (Meyer, 2010). The production time is 40 days. **Table 3.1** lists the key parameters in simulation.

Table 3.1– Key parameters for constant flow rate production.

Formation		Fracture	
Net Pay Thickness (ft)	160	Fracture width (in)	0.24
Permeability (nD)	580	Fracture permeability (Darcy)	1
Porosity (%)	5	Fracture porosity (%)	20
Pore pressure (psi)	4400	Total compressibility (1/psi)	1.6E-04
Temperature (°F)	238.37	Conductivity (md-ft)	20
Reservoir compressibility (1/psi)	1.6E-04	Fracture half-length (ft)	300
Gas specific gravity	0.56		

First, we look at the arriving temperature from the fracture to the wellbore before mixing with the wellbore fluid. The simulation results are shown in **Fig. 3.1** and **Fig. 3.2**. For constant flow rate production, the pressure near the wellbore and fracture keeps decreasing. Mainly due to the Joule-Thomson cooling effect by gas expansion inside and near fractures, the arriving temperature has the similar trend with the bottomhole pressure behavior.

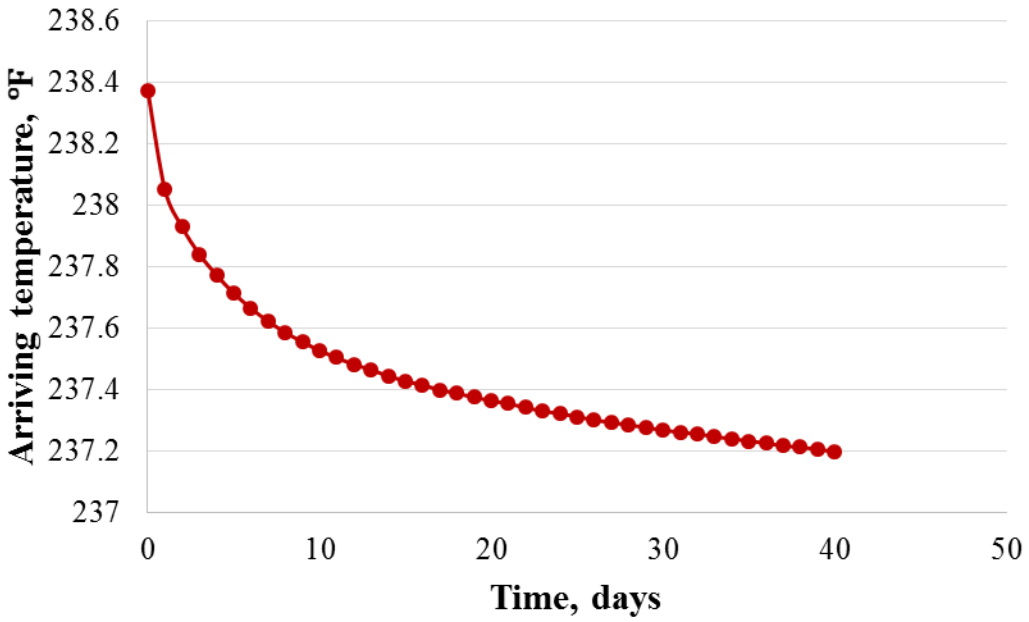

Fig. 3.1– Arriving temperature at wellbore with production time.

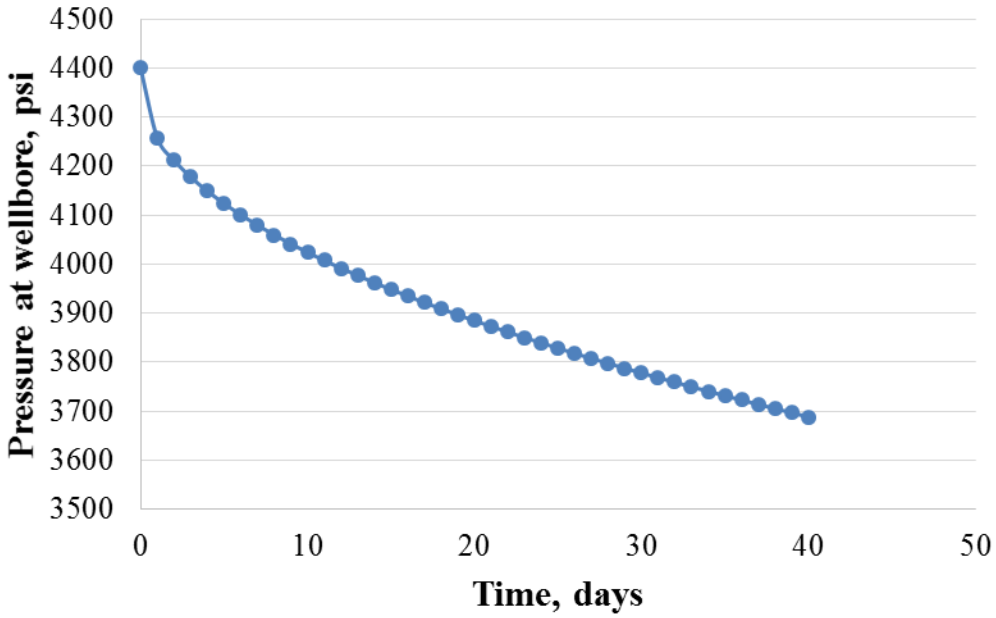

Fig. 3.2– Wellbore pressure with production time.

3.2.1 Uniform Fractures

Assuming that there are six identical hydraulic fractures along a wellbore section as **Fig. 3.3** shows. By coupling with the wellbore model, the fluid temperature inside wellbore is shown in **Fig. 3.4**. According to the energy balance equation in the wellbore, the fluid temperature is determined by the Joule-Thomson effect in wellbore due to the pressure gradient, the geothermal temperature, the conductive heat transfer between formation and wellbore, and the convective heat transfer by inflow. Since this synthetic case is a perfect horizontal well, the geothermal temperature is the same along the wellbore, also the pressure gradient in wellbore is subtle so that gas expansion is ignorable. The cooler inflow from fracture is the primary reason causing the wellbore fluid temperature has noticeable change. The heat conduction between formation and wellbore then warm the wellbore fluid gradually.

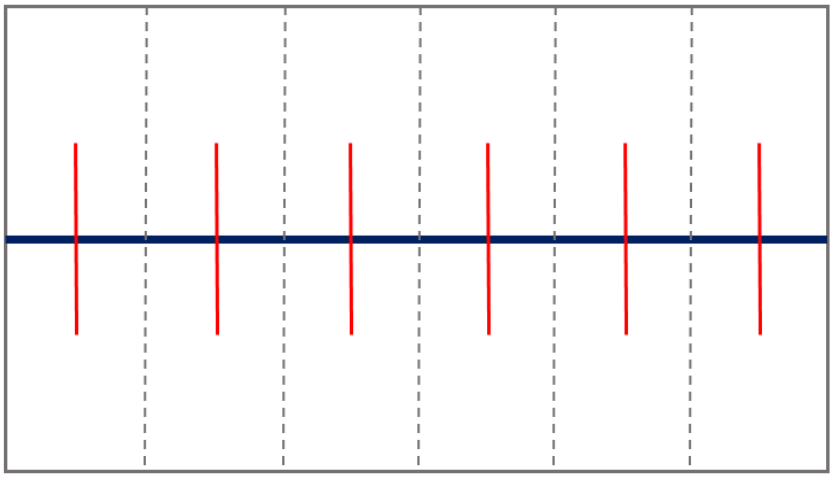

Fig. 3.3– Geometry of uniform fractures along the wellbore section.

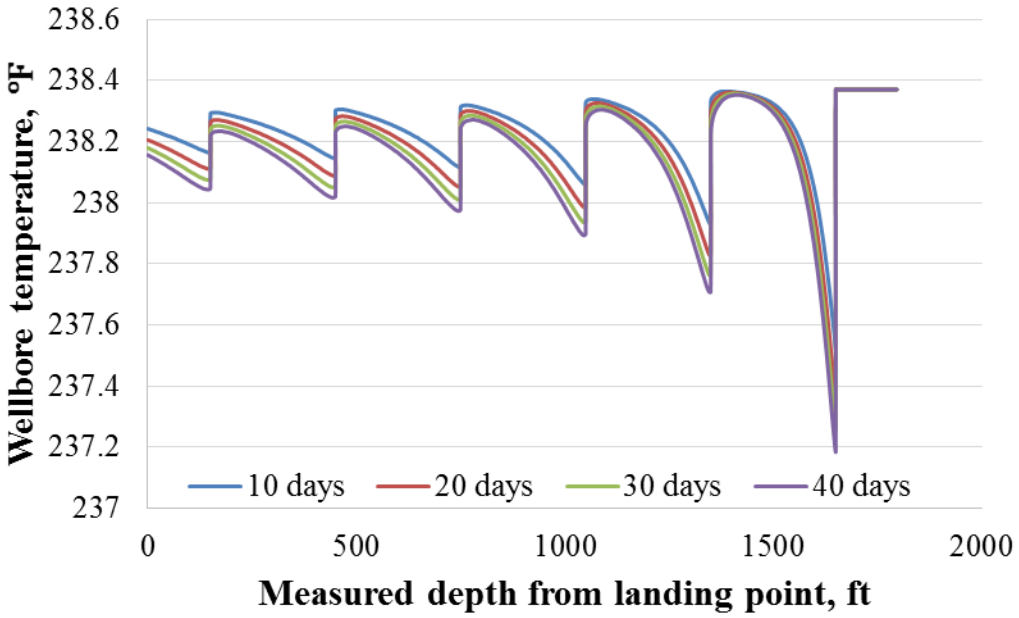

Fig. 3.4– Fluid temperature along the wellbore section.

The fluid flows from toe to heel (from right to left in **Fig. 3.5**). As the fluid flows towards the heel, there are inflow from fractures mixing with upstream wellbore fluid. For uniform fractures, the inflow temperature from each fracture is the same at the wellbore, the reason for the wellbore temperature behavior shown in **Fig. 3.4** is due to the mixture process at fracture locations. As the upstream wellbore fluid amount increases, the temperature change at fracture locations becomes less noticeable.

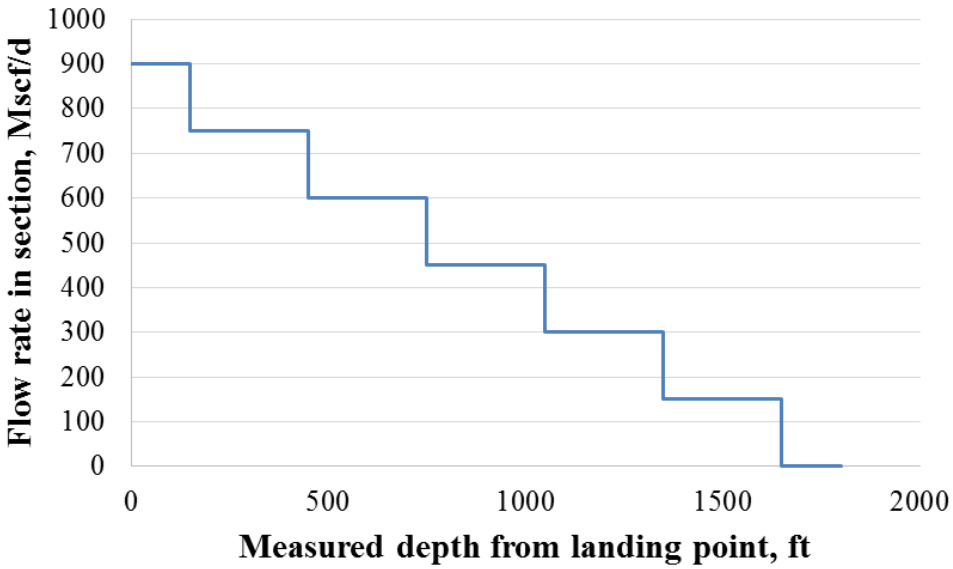

Fig. 3.5– Flow profile along the wellbore section.

3.2.2 Non-uniform Fractures

The 'effective' fracture half-length is critical for the development of unconventional gas reservoirs. Most commonly the created fracture length could extend hundreds feet long in shale reservoirs during fracturing treatment. The propped length is less than created length because the proppant cannot reach the tip of the fracture. The effective fracture length is even shorter than propped length because of gel damage. Here in our model, the fracture half-length means the effective length which contributes gas production. **Fig. 3.6** shows the fracture geometry with different fracture lengths along the horizontal section, and **Table 3.2** lists the values of fracture half-lengths. Note that the fracture numbering direction is from toe to heel, which is in the same direction as hydraulic fracture stage sequence.

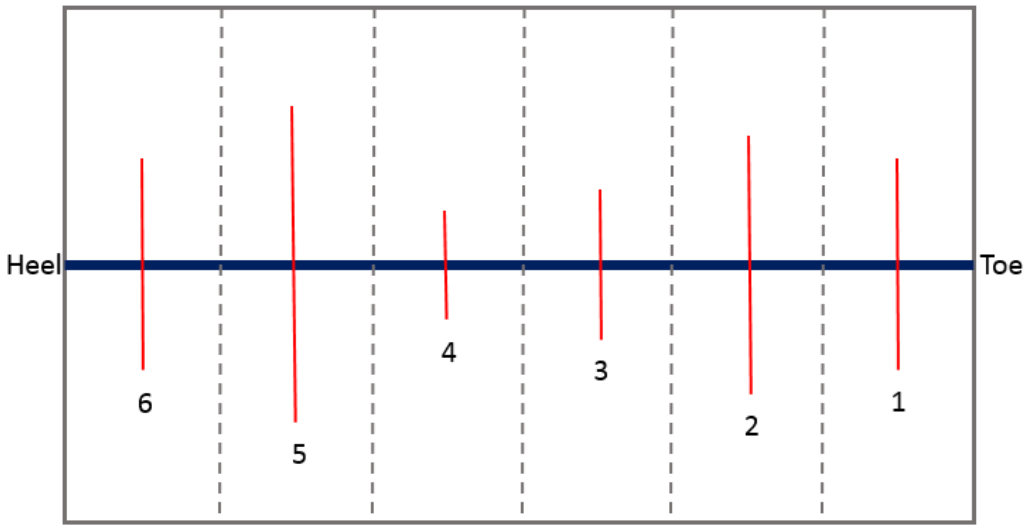

Fig. 3.6– Fracture geometry for non-uniform case.

Table 3.2– Different fracture half-lengths for non-uniform case.

Fracture number	Fracture half length, ft
1	200
2	250
3	150
4	100
5	300
6	200

For multi-stage fractured horizontal well, we could fix the total flow rate at the surface, but in order to obtain a continuous pressure distribution in horizontal wellbore, the flow rate of each fracture would still be different during the transient period as **Table 3.3** shows.

Table 3.3– Flow rate distribution for non-uniform fractures case.

Fracture number	Flow rate, Mscf/d/frac
1	151.5
2	184
3	117
4	82
5	214
6	151.5
Total	900

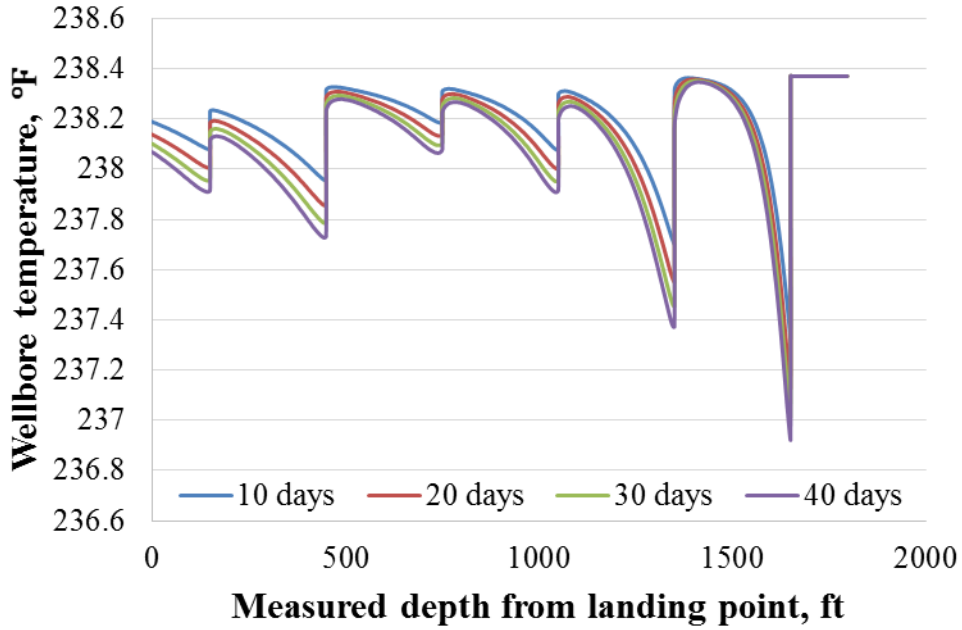

Fig. 3.7– Fluid temperature along the wellbore section.

Figure 3.7 shows the transient wellbore temperature for non-uniform fractures with the same total flow rate compared with the uniform fractures. At the fracture location which has the most production rate (the fifth fracture), the mixing temperature inside wellbore is influenced by warm upstream fluid, causing the temperature drop is less compared with the fracture at the toe (the first fracture). **Fig. 3.8** is the flow profile interpreted from non-uniform fractures.

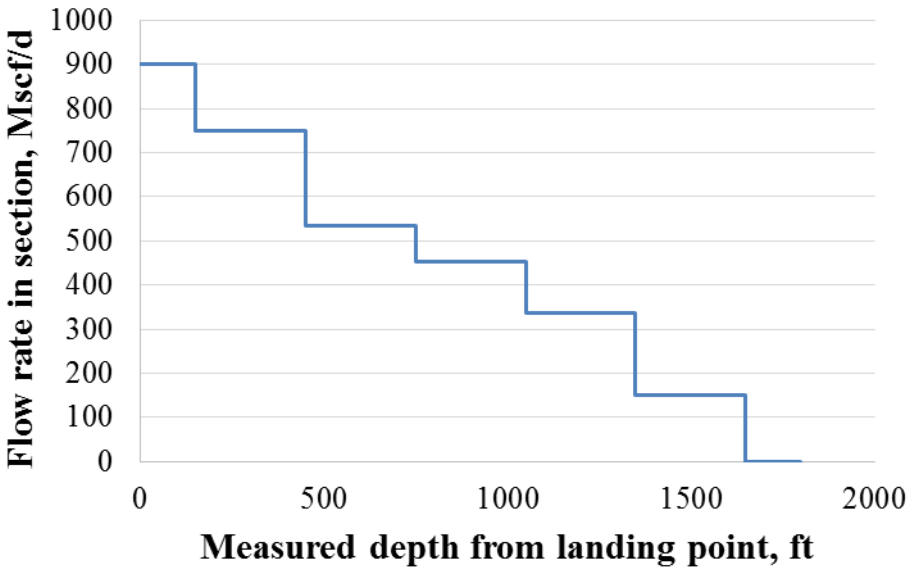

Fig. 3.8– Flow profile along the wellbore section.

3.2.3 Effect of Fracture Conductivity

The fracture conductivity is a key parameter which measures the transport capability of fractures. During the pressure transient period under the constant gas production, it will have an impact on the rate of pressure decline, thus influence the transient temperature behavior. **Fig. 3.9** and **Fig. 3.10** show the transient arriving temperature and the bottomhole pressure by varying the fracture conductivity from 10 to 1000 md-ft.

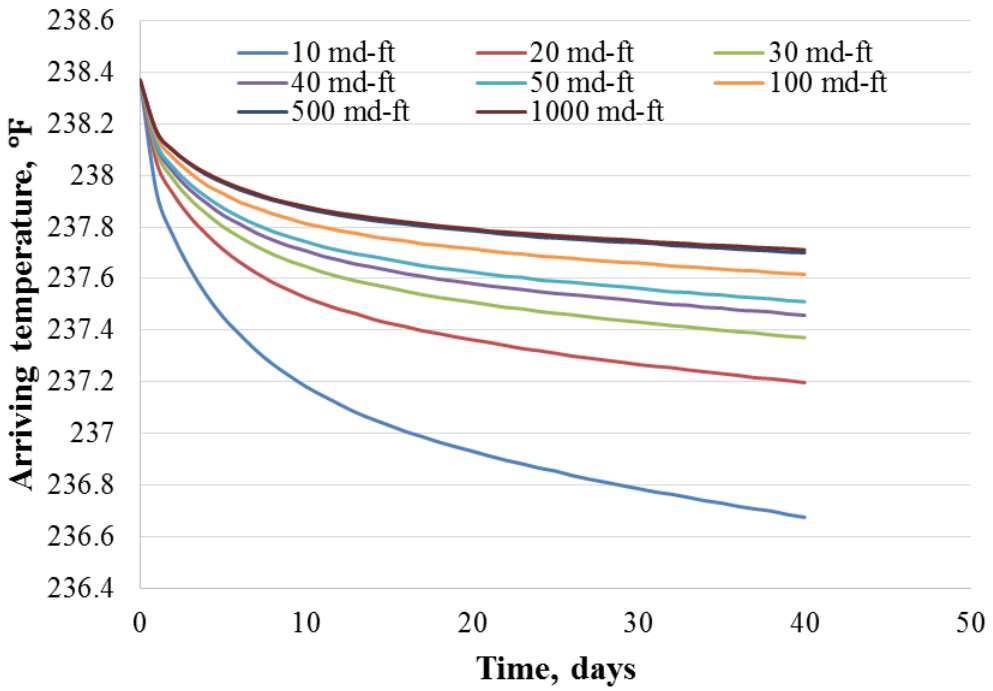

Fig. 3.9– Arriving temperature at wellbore with production time (different fracture conductivity).

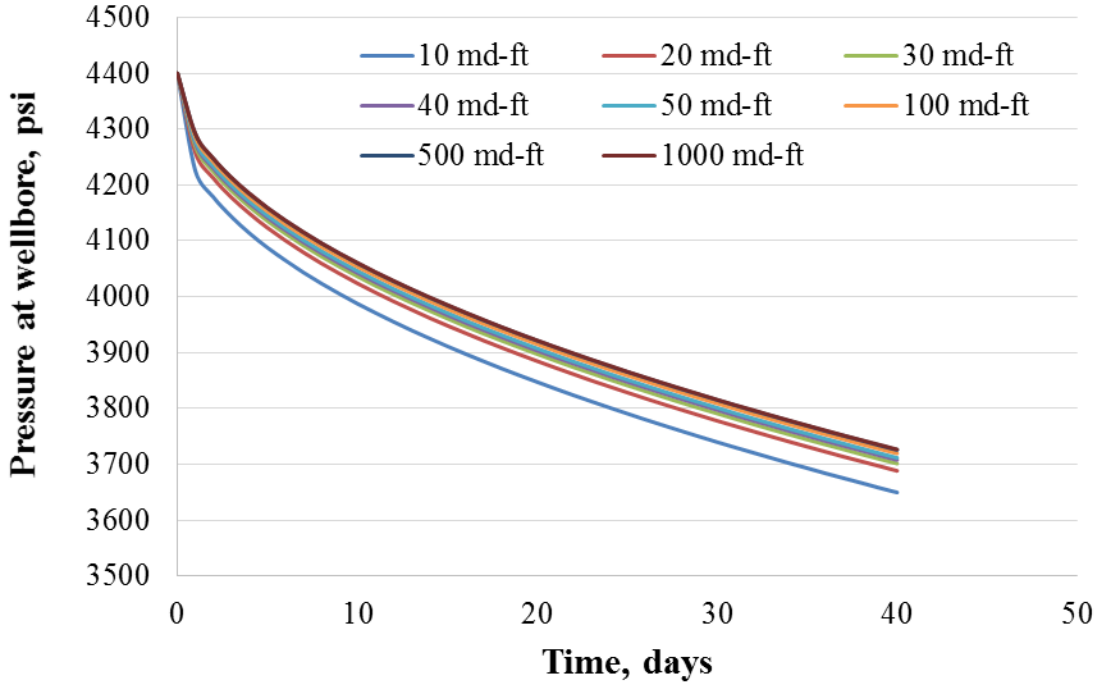

Fig. 3.10– Wellbore pressure with production time (different fracture conductivity).

As **Fig. 3.10** shows, with lower conductivity, the pressure decline is faster in order to produce the same. **Fig. 3.9** demonstrates the corresponding arriving temperature behavior that lower conductivity would lead to cooler temperature at the wellbore. When the conductivity is less than 50 md-ft, the temperature difference is easier to identify, since the fluid flow in fracture still have certain resistance which cannot be ignored.

3.3 Constant Bottomhole Pressure Cases

During long-term production period, the constant bottomhole pressure is the common constraint at the wellbore. The flow rate change history has a significant influence on the transient behavior of the arriving temperature. **Table 3.4** shows the key variables used. The reservoir initial pressure is 4400 psi and the bottomhole pressure is 2600 psi.

Table 3.4– Key parameters for constant bottomhole production.

Formation		Fracture	
Net Pay Thickness (ft)	160	Fracture width (in)	0.24
Permeability (nD)	580	Fracture permeability (Darcy)	1
Porosity (%)	5	Fracture porosity (%)	20
Pore pressure (psi)	4400	Total compressibility (1/psi)	2.0E-04
Temperature (°F)	238.37	Conductivity (md-ft)	20
Reservoir compressibility (1/psi)	2.0E-04	Fracture half-length (ft)	300
Gas specific gravity	0.56		
Bottomhole pressure (psi)	2600		

For constant bottomhole pressure, **Figs. 3.11** and **3.12** illustrate the arriving temperature at the wellbore and flow rate for single fracture with production time correspondingly. Because the flow rate declines with production time, the arriving

temperature increases gradually. As fluid velocity reduces, conductive heat transfer would warm the fluid quickly.

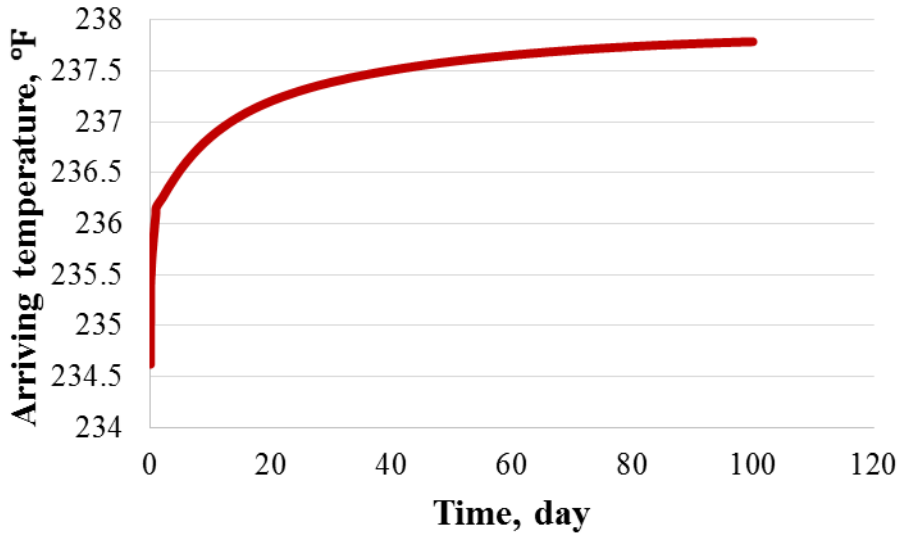

Fig 3.11– Arriving temperature at wellbore with production time.

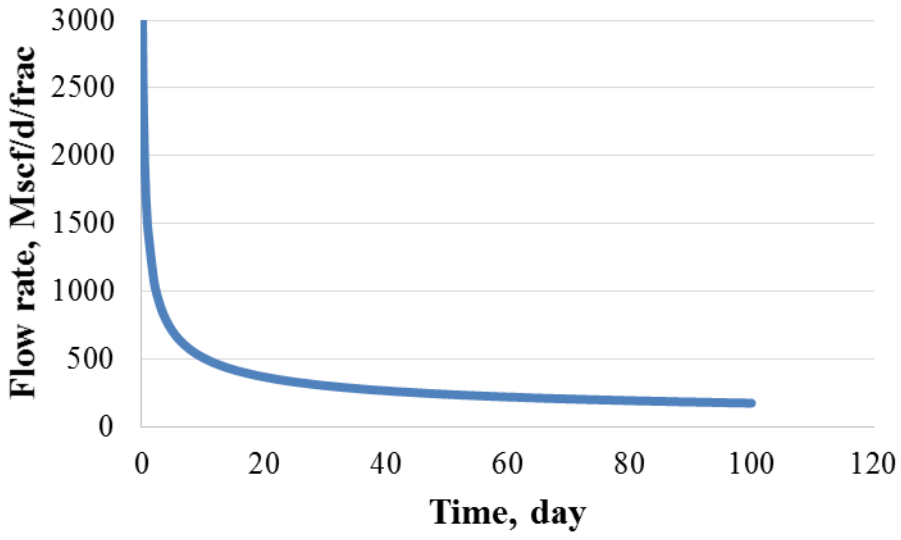

Fig 3.12– Flow rate of single fracture with production time.

The temperature and pressure distribution in the reservoir are shown in **Fig. 3.13** and **Fig. 3.14** separately. The pressure propagation in the tight gas reservoir is slow and the noticeable temperature change only happens near and inside the fracture. Thus the adoption of refined grid near the fracture is better than uniform grid in order to capture the transient temperature front.

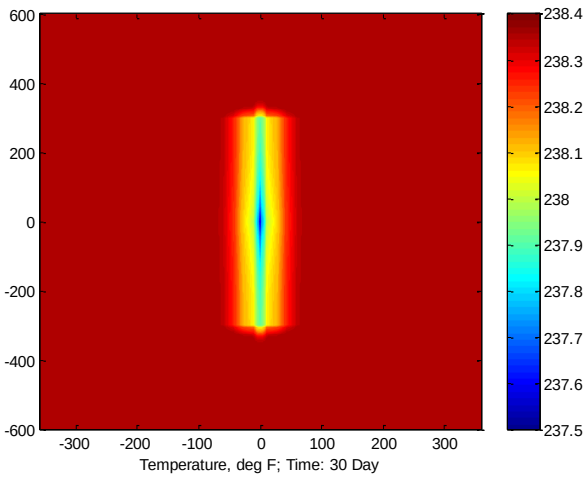

Fig. 3.13– Temperature distribution in reservoir of single fracture after 30 days.

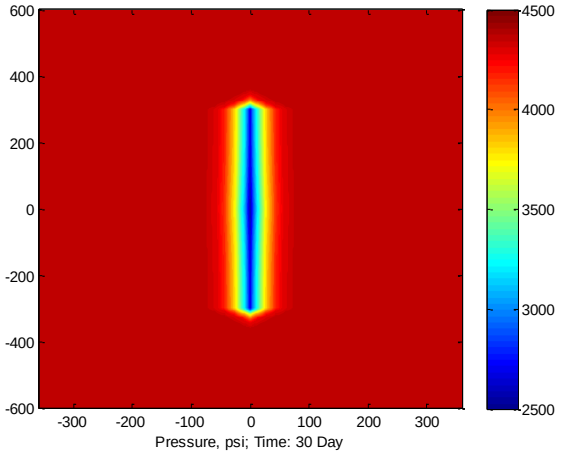

Fig. 3.14– Pressure distribution in reservoir of single fracture after 30 days.

3.3.1 Uniform Fractures

Coupling the fracture/formation thermal model with the wellbore model, the temperature distribution along the wellbore can be obtained based on the six uniform fractures case. The reservoir geometry and properties are the same with uniform case with constant flow rate, only the bottomhole pressure are settled at 2600 psi at the beginning of production.

Figure 3.15 illustrates the temperature curves in wellbore with different production days. The wellbore temperature increases gradually with production days, which is on the contrary comparing with the one under constant flow rate. For constant flow rate, the temperature is mainly determined by gas expansion due to pressure drawdown. For constant bottomhole pressure, both the pressure gradient and flow rate are changing near fractures, which causes difficulty for analysis. As mentioned in the literature review, for low permeability reservoir, even though the pressure drawdown is large, the temperature change in formation is subtle since heat conduction would dominate in the heat transfer process. Then the transient flow rate behavior would play the decisive role during production. As the flow rate declines with time as shown in **Fig. 3.16**, the wellbore temperature at the fracture locations would increase with production time.

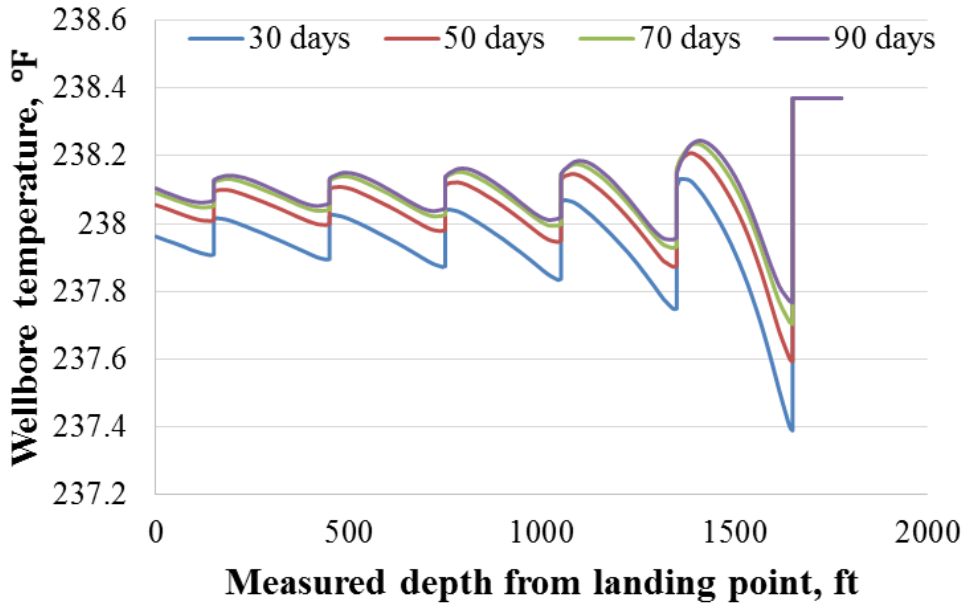

Fig 3.15– Temperature distribution along wellbore section.

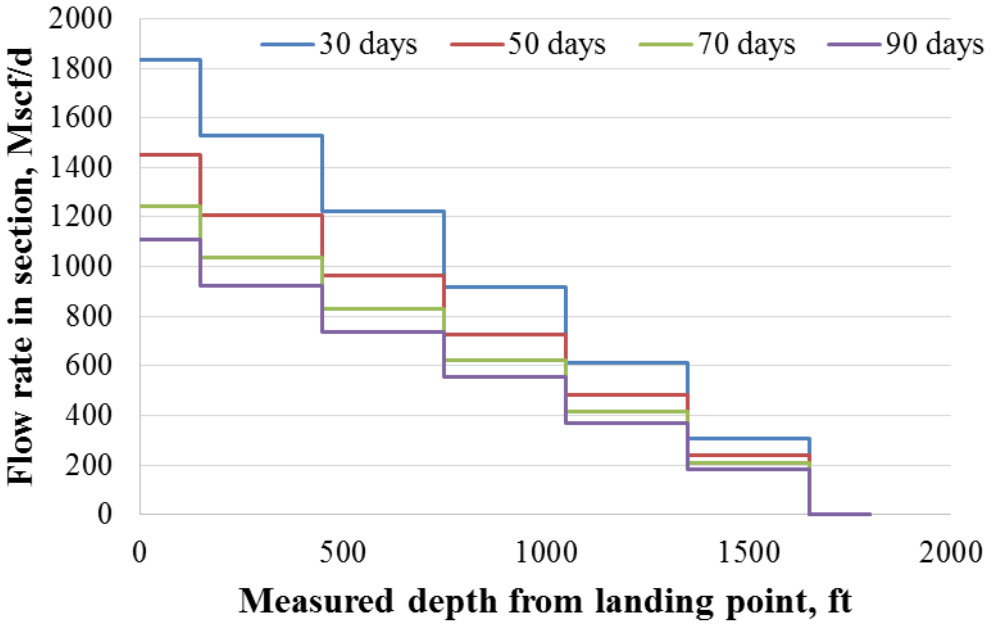

Fig 3.16– Flow rate distribution along wellbore section.

3.3.2 Non-uniform Fractures

By using the fracture half-lengths in **Table 3.2** and following the same fracture numbering in **Fig. 3.6**, we could obtain the transient wellbore temperature behavior and flow rate as shown in **Fig. 3.17** and **Fig. 3.18** for non-uniform fractures.

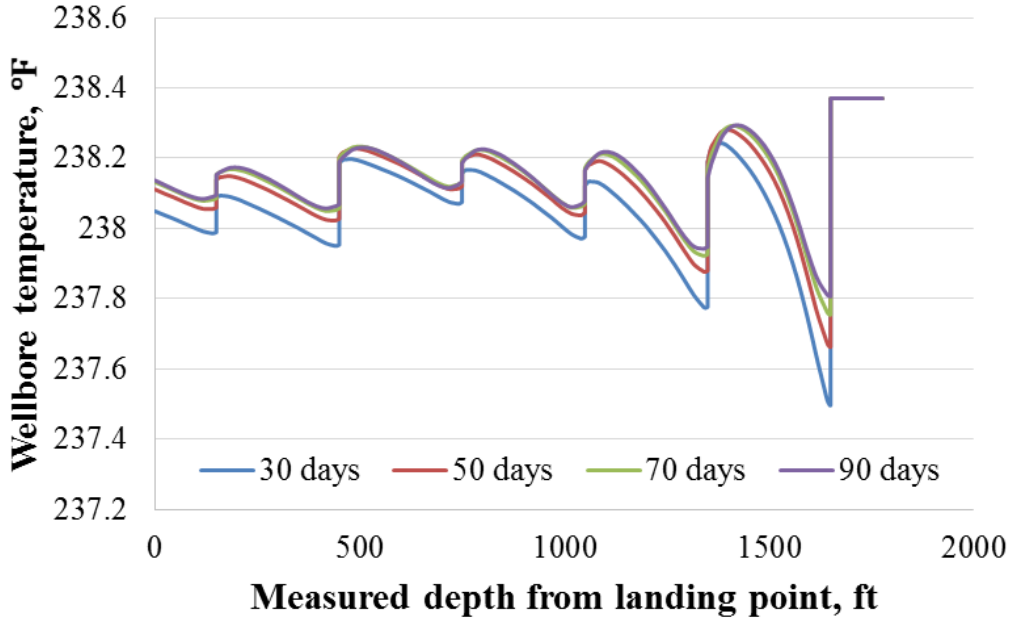

Fig 3.17– Temperature distribution along wellbore section.

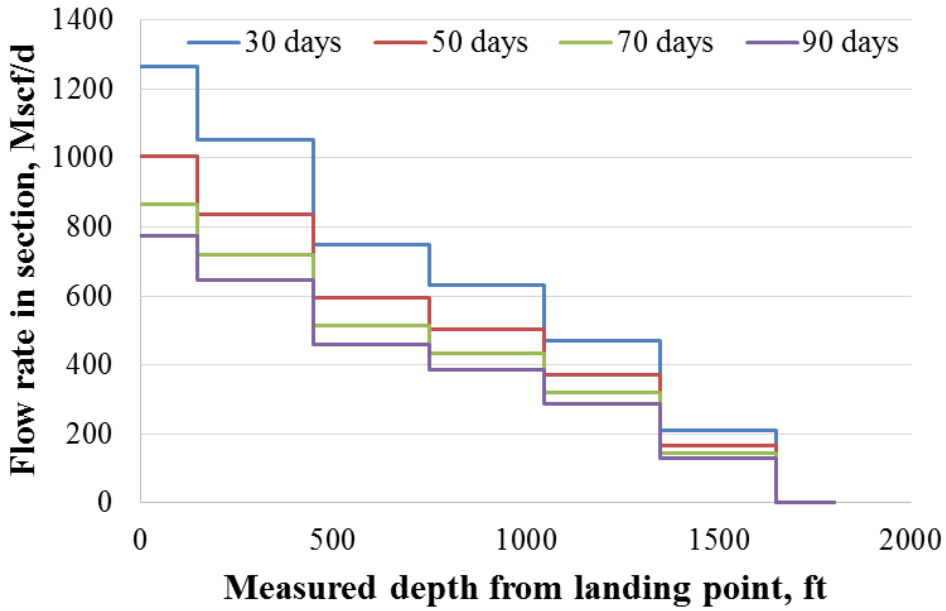

Fig 3.18– Flow rate distribution along wellbore section.

For the second and the fifth fractures, the half-lengths are longer than 200 ft and produce more, we cannot observe the most cooling effect at the fracture locations since the upstream fluid amount and temperature will warm the mixed wellbore temperature. The first and the last fracture half-lengths are equal to 200 ft, but the wellbore temperature drop is quite different. The temperature increase slope in no-inflow section due to heat conduction is relatively mild towards the heel because of fluid accumulation inside wellbore. The flow rate decline becomes slower with production days, thus the wellbore temperature curves at different time get closer to each other after 60 days' production.

3.3.3 Effect of Fracture Half-length

As the synthetic examples show, the fracture length shows a strong correlation with the flow rate thus influence the wellbore temperature. **Fig. 3.19** and **Fig. 3.20** show the

arriving temperature and the corresponding flow rate with different fracture half-lengths. With longer fracture length, the flow rate is higher, thus the arriving temperature is lower. The outer boundary condition will influence the trend of these two plots. Here we assume infinite no-flow outer reservoir boundary, the fracture half-length is close to a linear relationship with the flow rate.

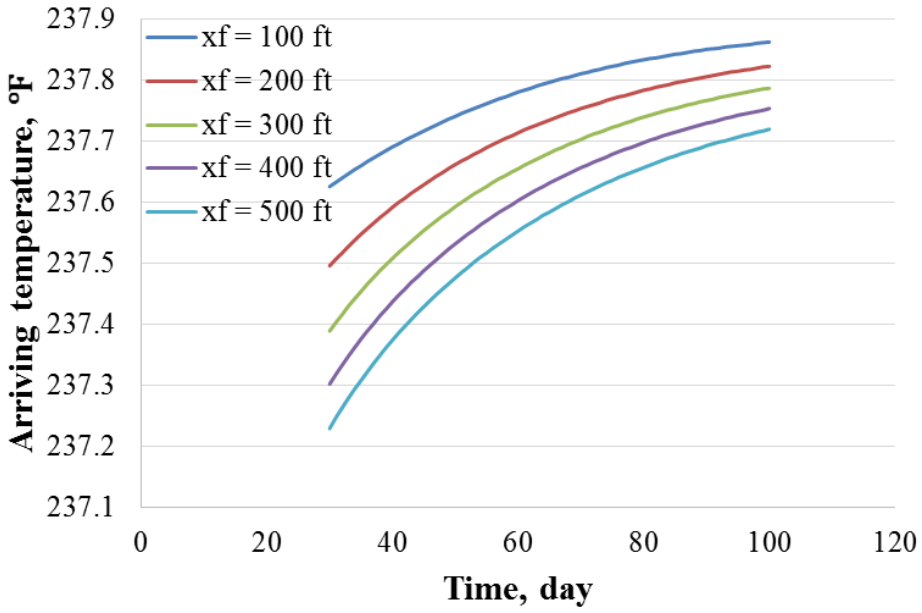

Fig. 3.19– Arriving temperature at wellbore with production time (different fracture half-lengths).

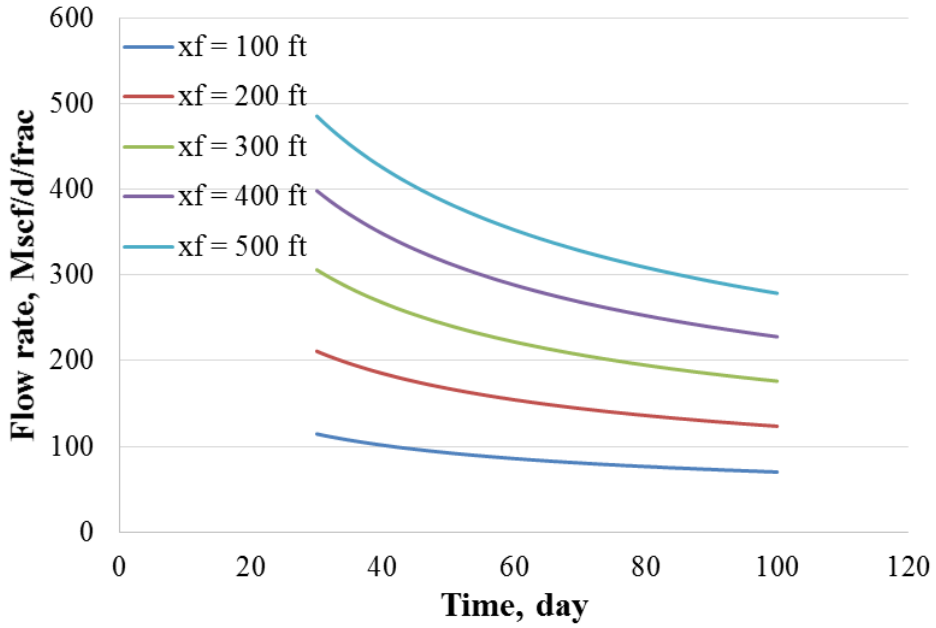

Fig. 3.20– Flow rate with production time (different fracture half-lengths).

3.3.4 Sensitivity Study

The objective of the sensitivity study is to quantify each parameters' sensitivity to the arriving temperature at the wellbore, thus identify the primary variables which have higher impact on the temperature change. First a base case is set up, then the variables are changed by a certain percentage to compare their influence on the arriving temperature. The variables for the base case and changes are given below in **Table 3.5**.

Table 3.5– Affecting parameters for sensitivity study under constant BHP.

Parameters	-75%	-50%	Base Case	50%	100%
Formation permeability, nD	150	300	600	900	1200
Fracture permeability, Darcy	0.25	0.5	1	1.5	2
Fracture half-length, ft	75	150	300	450	600
Fracture width, in	0.06	0.12	0.24	0.36	0.48
Fracture porosity, %	5	10	20	30	40
Formation porosity, %	1.25	2.5	5	7.5	10
Total compressibility, 1/psi	0.00004	0.00008	0.00016	0.0002	0.0003
Fluid heat capacity, Btu/(lb-°F)	0.1839	0.3678	0.7356	1.1035	1.4713
Rock heat capacity, Btu/(lb-°F)	0.0505	0.1010	0.2020	0.3030	0.4040
Gas specific gravity	-	-	0.56	0.672	0.784

Based on the sensitivity study, we can identify the primary variables which have significant influence on arriving temperature at the wellbore. **Fig. 3.21** shows the arriving temperature change after 30 days of production when the variables change 50% from the base case. From the plot we can identify that the formation porosity and heat capacity of rock have significant influence on the arriving temperature, following are formation permeability and fracture half-length. Among these parameters, we cannot change the formation properties, thus fracture half-length is the primary controllable variable that is important for the thermal behavior at the wellbore. **Figs. 3.22** and **3.23** plot the change of arriving temperature and flow rate corresponding to the change of variables.

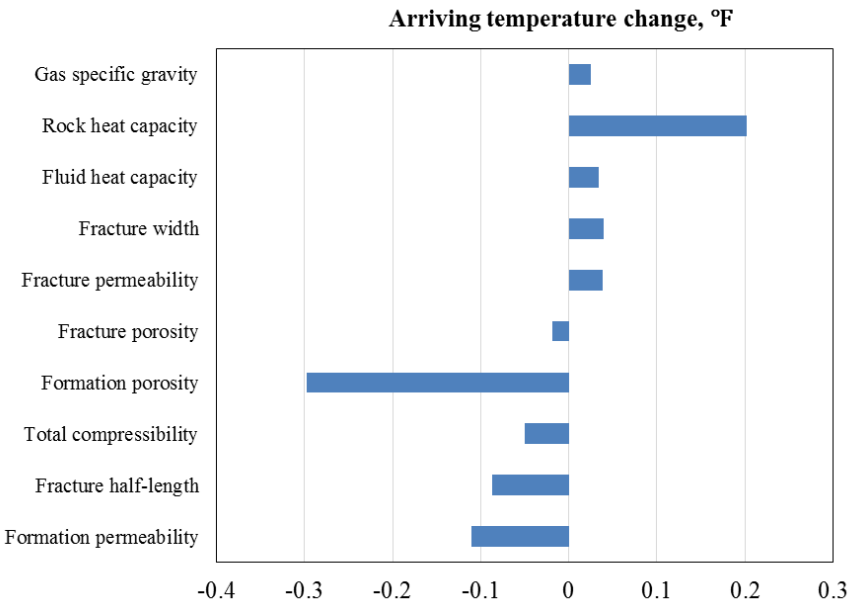

Fig. 3.21– Arriving temperature change when the affecting parameters increases 50% after 30 days of production.

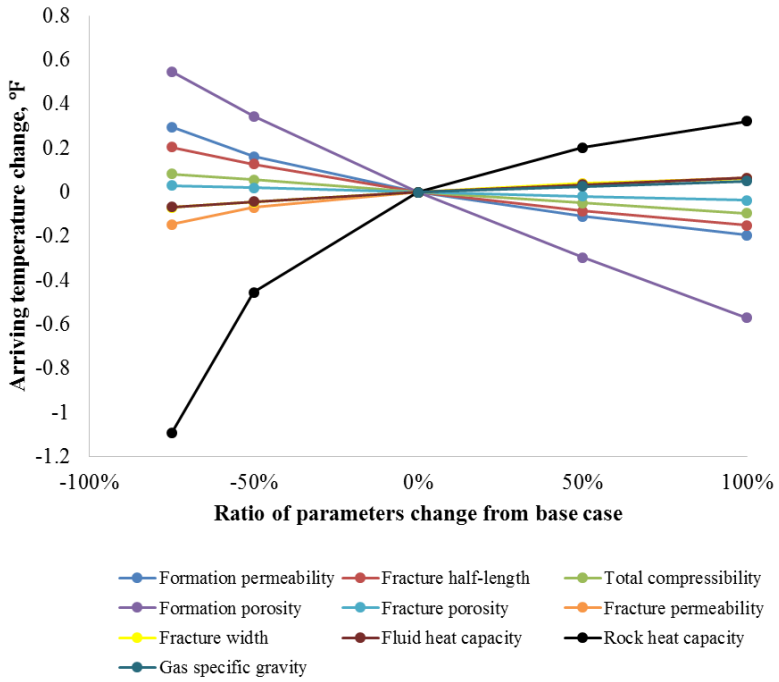

Fig. 3.22– Arriving temperature change after 30 days of production.

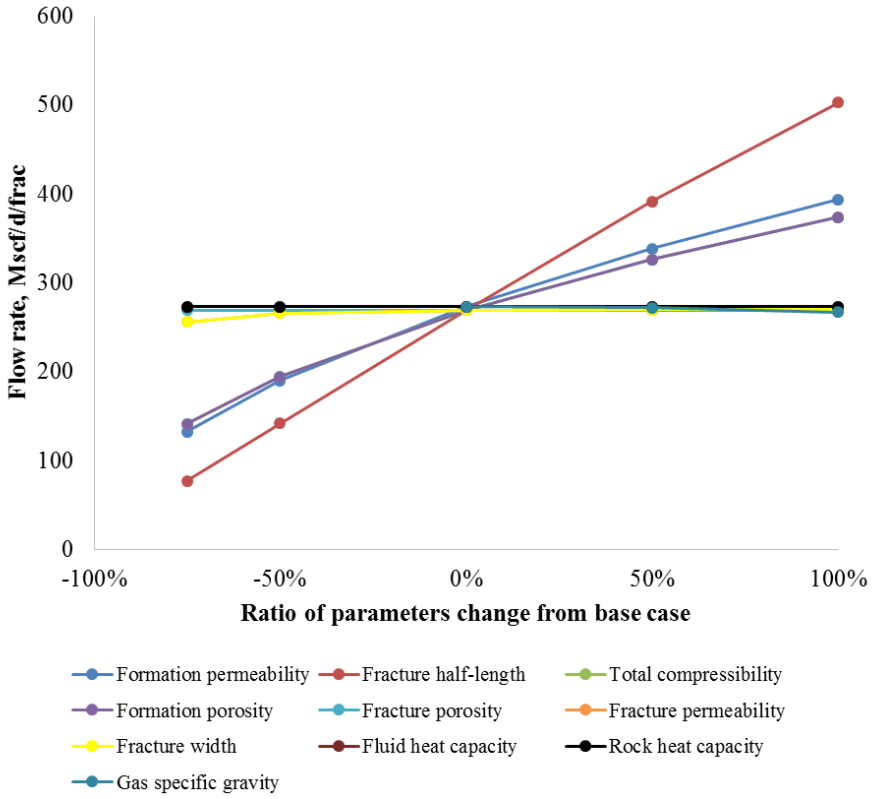

Fig. 3.23– Flow rate after 30 days of production.

3.4 Discussions

3.4.1 Fluid Mixture in Wellbore

The wellbore thermal model assumes instantaneous equilibrium in each small control volumes. The mixed temperature would be obtained right in the mixing control volume rather than after certain distance downstream. This causes the mismatch when we try to match a measured continuous wellbore temperature data. Fluid mixture is a complicate procedure inside wellbore since turbulence would happen. An analytical method was proposed by McKinley (Hill, 1990) that treats this problem as ‘black box’ and helps us understand the phenomenon.

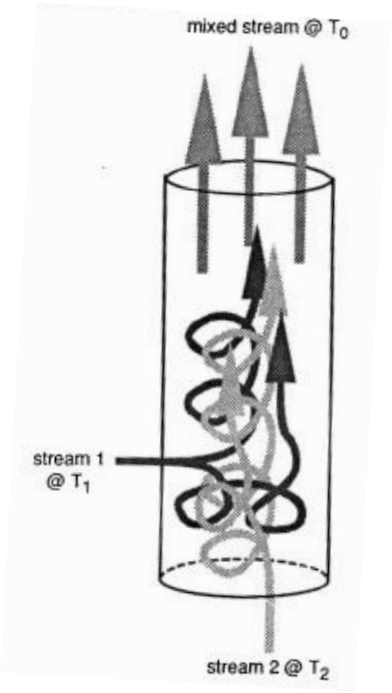

Fig 3.24– Mixing of two streams in a wellbore (Hill, 1990).

In **Fig. 3.24**, stream 1 is the inflow from the reservoir into the wellbore and stream 2 is the upstream fluid inside the wellbore, with the fluid temperature T_1 and T_2 separately. Appling the energy balance equation to the system, we have

$$w_1 C_{p1} T_1 + w_2 C_{p2} T_2 = (w_1 C_{p1} + w_2 C_{p2}) T_0 \tag{3.1}$$

where w_1 and w_2 are mass flow rates of stream 1 and 2, C_{p1} and C_{p2} are heat capacities of the two streams, and T_0 is mixed temperature. If the heat capacities of streams are similar, we could obtain

$$T_0 = \frac{w_1 T_1 + w_2 T_2}{w_1 + w_2} \tag{3.2}$$

Assuming that the temperature difference between stream 1 and 2 is T_2-T_1=ΔT. **Eq. 3.2** can be written as

$$T_0 = \frac{w_1(T_2 - \Delta T) + w_2 T_2}{w_1 + w_2} = T_2 - \frac{w_1}{w_1 + w_2}\Delta T \tag{3.3}$$

The mixed fluid temperature is determined not only by the inflow rate and temperature, but also the upstream flow rate and temperature. This is the reason that the temperature change when gas entering near the toe would be more obvious compared with the one near the heel. Taking the uniform fractures as an example as shown in **Fig. 3.3**, at the first fracture location near the toe, $w_1/(w_1+w_2)$ =1; at the sixth fracture location, $w_1/(w_1+w_2)$ =1/6. According to the mixing method, the wellbore fluid temperature change at the sixth fracture location is 1/6 of the temperature change at the first fracture location. This is consistent compared with the results calculated by the wellbore model as shown in **Fig. 3.4**. The temperature change at the first fracture location is 1.2˚F, while it is 0.2˚F at the sixth fracture location.

3.4.2 Inner Boundary Constraints

Based on the model we can estimate the flow profile along the wellbore at a certain production time, however, history matching is still difficult to implement. In synthetic cases, we assume that the geothermal temperature is the initial temperature in the reservoir and the wellbore. At the beginning of production, the pressure in the wellbore and fractures drop from the reservoir pressure to the bottomhole pressure within a very short time. Like mentioned before, this is not the reality for field case. The initial temperature is hard to determine for the modeling input since it demands a history matching considering the reservoir temperature change caused by fracturing treatment, flowback/warmback, and multi-rate production. This constant bottomhole pressure case only applies when the bottomhole pressure stabilized after certain production days. Taking Marcellus Shale for

example in **Fig 3.25**, the model can be applied after 90 days production when the bottomhole pressure stabilized around 550 psi. Before that we can use the principle of superposition to match the bottomhole pressure and gas production rate first, then use the thermal model to interpret the transient temperature behavior.

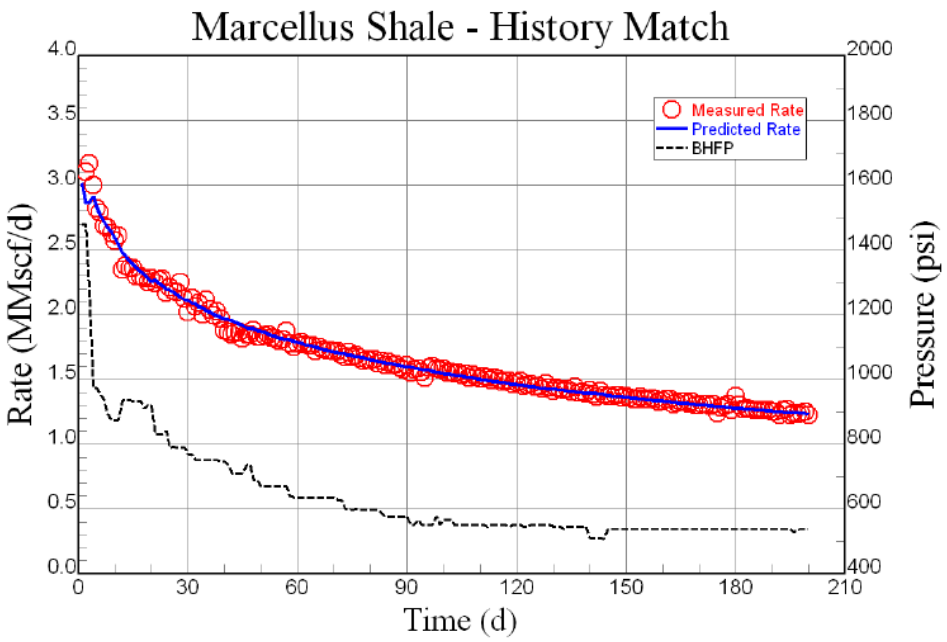

Fig 3.25– Marcellus Shale – History match of gas flow rate for multiple transverse fractures (Meyer, 2010).

3.5 Section Summary

In this Section, the synthetic examples help us to understand the transient wellbore temperature behavior under different inner boundary constraints. The constant flow rate case mainly explains the situation happens at the beginning of production, and the constant bottomhole pressure case applies after the bottomhole pressure stabilized during long-term production. Both homogeneous and heterogeneous fractures examples are illustrated to show how the pressure behavior and flow profile would affect the wellbore temperature distribution.

4 FIELD APPLICATION*

This Section presents the application of the established model to interpret flow profile based on temperature data acquired from two multi-stage fractured horizontal wells in Eagle Ford.

4.1 Introduction

We discussed the characteristics of transient temperature behaviors and flow rate distribution along a fractured horizontal wellbore in the synthetic examples in the previous section. The temperature decrease when gas entering the wellbore is typically strong at the toe and weak towards heel if the fractures are more evenly created along the wellbore due to the fluid mixture inside wellbore. Two field cases are presented to illustrate the application of using the temperature model to understand the fracture/flow distribution. The estimation of flow rate distribution from the temperature model is compared to the interpretation of flow by production logging tools. The field cases would have more complicate situations. The wellbore trajectory variation would have significant influence on the geothermal temperature thus affect the accuracy of wellbore fluid temperature interpretation. The trajectory can also cause the existence of water sump in lower sections which might mask the gas entries from the measured temperature data. By applying the simplified model and comparing with the measured data, we illustrate how the model

* Reproduced with permission from "Diagnosis of Multi-Stage Fracture Stimulation in Horizontal Wells by Downhole Temperature Measurements" by J. Cui, D. Zhu, and M. Jin. Paper SPE 170874 presented at the SPE Annual Technical Conference and Exhibition in Amsterdam, The Netherlands, 27-29 October. Copyright 2014 by the Society of Petroleum Engineers.

works for practical cases, what is the problem for model application, and most importantly, how much accuracy we could obtain, and how to improve that. The details are presented below.

4.2 Well EF-1

4.2.1 Well Information

Well EF-1 is a gas well producing 1600 Mscf/d after hydraulic fracture treatment. The water production is 160 stb/d and surface GOR is about 9000-10000 scf/stb. Since the well is producing under dew point pressure, there exists retrograde liquid inside the wellbore, which is less than 10% of total volume according to PVT data. The model neglects the heat transfer caused by phase change. Our goal is to interpret flow profile by matching the temperature. The flow profile is proportional to the fracture volume. To use the forward model, we need to have three dimensions of the fracture, not just the fracture volume. Since we are not ready to interpret the fracture geometry yet with the model, we assume the fracture height and width are constant, and only change the fracture length to yield a fracture volume that give the flow rate corresponding to the temperature behavior. Notice this fracture length is not the actual fracture half length, and it is just a dummy parameter to get the temperature match. In this way we can estimate the flow profile. Thus we call this fracture length "equivalent fracture length". We assume all other parameters are fixed, the only parameter we changed to obtain the match is the equivalent fracture length that yields the flow capacity from a fracture when multiplied by fracture conductivity. The fixed parameters used in the interpretation are shown in **Table 4.1**.

Table 4.1– Input data in Well EF-1 field case, fixed parameters.

Formation		Fracture/Wellbore	
Permeability (nD)	583	Fracture spacing (ft)	77
Porosity (%)	4.2	Fracture width (in)	0.24
Pore pressure (psi)	4630	Fracture porosity (%)	25
Reservoir Compressibility (1/psi)	1.68E-04	Fracture permeability(md)	1250
Gas specific gravity	0.56	Wellbore pressure (psi)	2860

The fracture treatment for Well EF-1 has 15 stages along the horizontal section. Each stage has 4 perforation clusters and the perforation spacing is 75 ft. The trajectory of horizontal section is shown in **Fig. 4.1** and the stages are numbered. We also marked the perforations along the wellbore (the dots).). The temperature data available are from stage 7 to stage 15. The temperature log has four passes, two up passes and two down passes. The average temperature data from all four passes by PLT is used in interpretation, as shown in **Fig. 4.2**. When the well was put back on production, gas production started about 15 days after flowback, and temperature logging was run about three months after the well was on production. At that time, the water cut became stable and the volumetric fraction is small (<2%), so we assumed single phase gas flow in the interpretation.

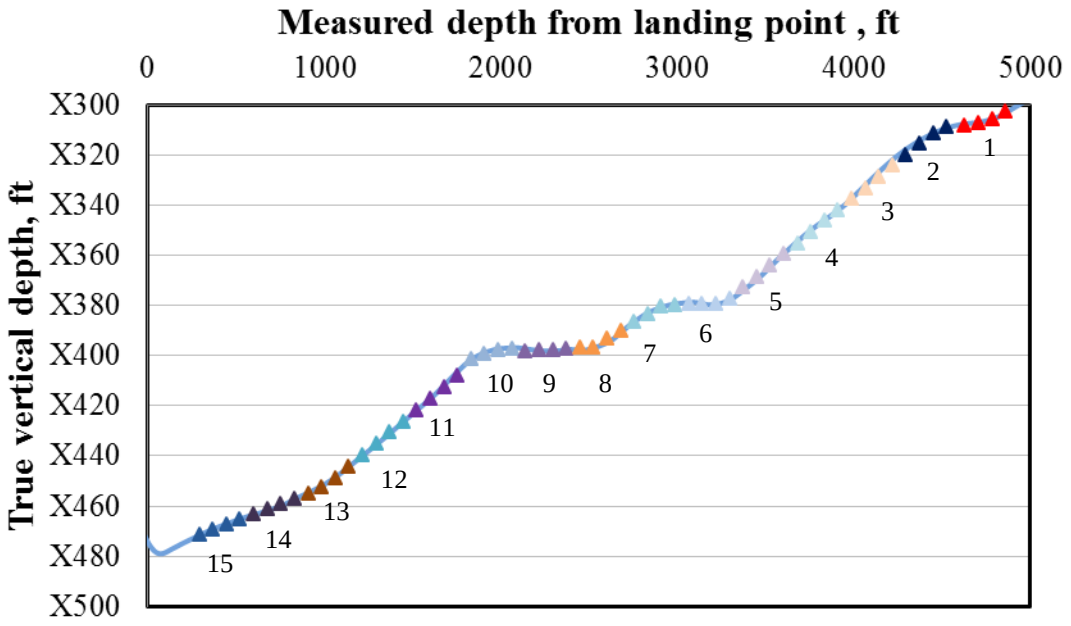

Fig. 4.1– Wellbore trajectory and designed perforation location for Well EF-1.

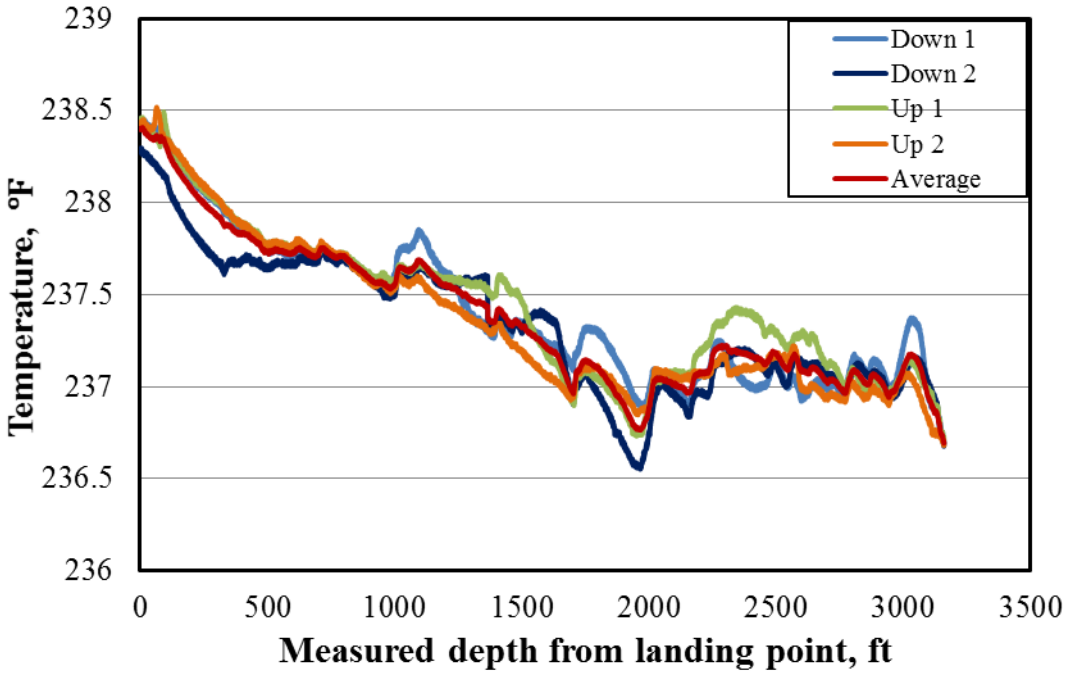

Fig. 4.2– PLT data sets for Well EF-1.

4.2.2 Simulated Results

When a gas enters a wellbore, the Joule-Thomson cooling effect causes temperature drop at the location of entry. Based on this, we can initially identify the possible fracture locations. For perforated and fractured horizontal well, the fractures is more likely be generated at the perforation locations. In this example, we assumed initially the fracturing treatment generated fractures every 77 ft (75 ft spacing plus 2 ft of perforation zone) along the horizontal well according to perforation design.

Figure 4.3 shows the geothermal temperature along horizontal wellbore, the simulated result and the measured data. Because the well is toe-up (**Fig. 4.1**), the geothermal temperature is higher at the heel. The temperature difference between the toe and the heel is about 1.4˚F. Since temperature change caused by the Joule-Thomson effect is usually smaller than 1˚F, accurate estimation of geothermal temperature is crucial and should be calibrated carefully before interpreting temperature data. From **Fig. 4.3**, each sharp-decrease of temperature corresponding to a fracture. The larger the temperature drop, the higher the flow rate into the wellbore from the fracture. This is the theoretical based of interpretation. For same flow rate, the temperature drop at the toe is higher than the drop at the heel. This is because after the fluid enters the wellbore, the upstream fluid inside the wellbore with higher temperature will warm the inflow stream up. At the toe, there is no upstream fluid. Thus a higher temperature drop at the toe does not necessarily mean a higher flow rate. As the wellbore fluid flows towards the heel, the total flow rate increases, and the contribution of the fluid from the fracture become smaller while the upstream wellbore fluid has stronger influence on the mixing temperature. As the cooling effect is masked by the wellbore flow, the wellbore temperature change becomes smaller toward

the heel. It should point out that the mixing procedure takes some distance to stabilize, but the model assumes an instantaneous equilibrium which causes the wellbore temperature to change sharply at fracture locations (**Fig. 4.3**). Since the data is measured by PLT, the movement of the tools used to measure temperature data inside wellbore also cause some thermal dispersion effect which makes the measured data smoother.

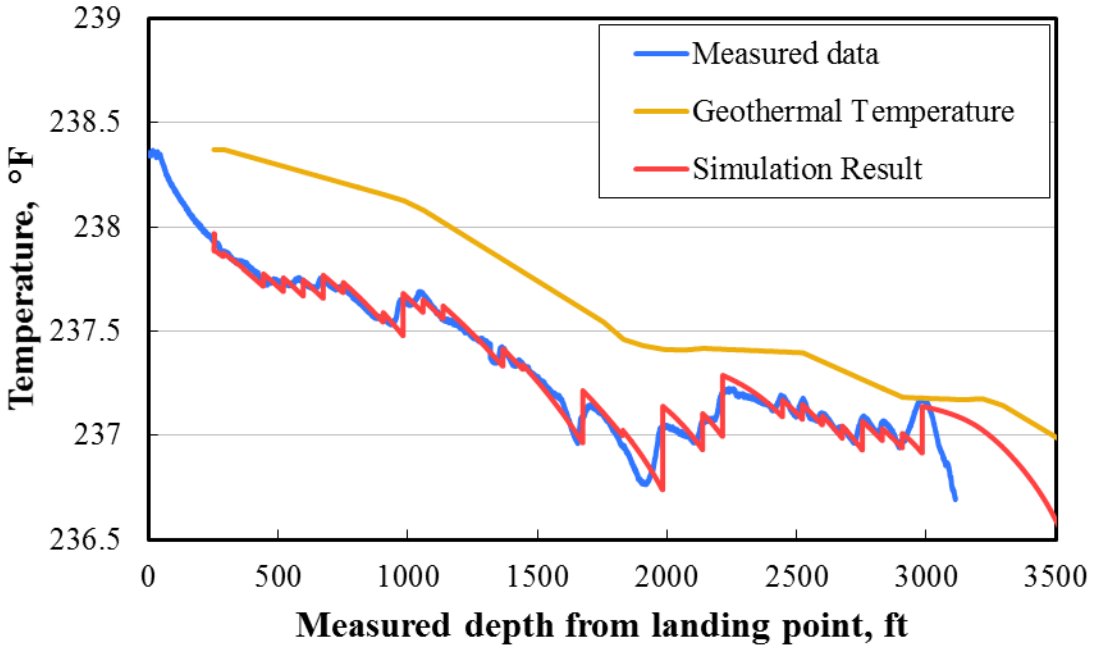

Fig. 4.3– Simulated and measured temperature data match for Well EF-1.

The temperature continuously increases from 1753 ft to 1984 ft in the entire Stage 10. This indicates no gas production in this section, and the fracture is not generated productively at this stage. The same thing happens from 1444 ft to 1598 ft. If there is smooth minor temperature drop in a section instead of sharply drop, it could mean that small fracture network might be generated instead of one primary fracture. This phenomenon usually happens where there is no perforation.

Figure 4.4 shows an enlarged section of measured and calculated temperature against the perforations. From **Fig. 4.4** we can see clearly how the temperature changes corresponding to the perforation locations. Each temperature change of increasing and then decreasing (generating a temperature peak) indicates an existing fracture. The magnitude of the peak indicates the size of the fracture. Large fractures could happen at 2200 ft and 2760 ft, and it is also possible that at the location of the measured depth from 2291 ft to 2370 ft, there is no fracture generated. The wellbore fluid temperature continues increasing over this section because of the heat conduction between the wellbore fluid and the outside formation.

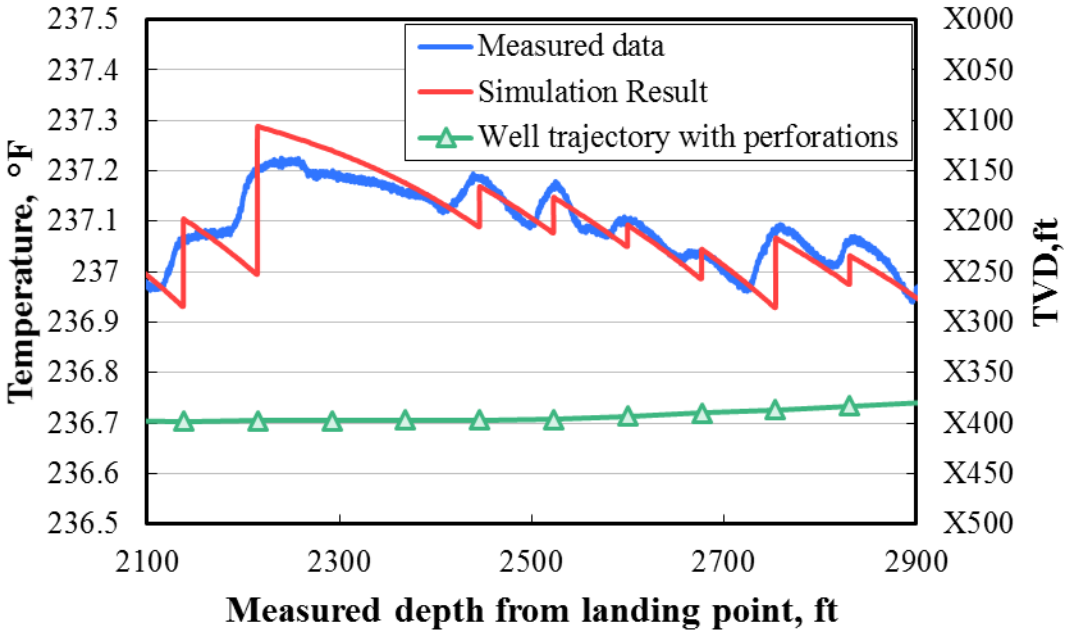

Fig. 4.4– Compare a portion of perforation design with temperature data.

Using the thermal model developed, we can estimate the flow rate distribution along horizontal wellbore. **Fig. 4.5** shows that the flow rate calculated from the temperature

model increase continuously from 3224 ft to the heel. The increase slope is relatively flat from 1521 ft to 1829 ft, indicating there is no production from this stage. The result is compared with the flow distribution from other methods, including using spinner meter interpretation (Liao, et al., 2013), and commercial software of Plato and Emeraude (KAPPA, Inc.). Plato is only temperature data interpretation. In Emeraude, it can run both spinner and temperature data interpretation. The spinner measurement and interpretation are highly influenced by the wellbore flow regime, which causes more uncertainty in gas flow. The temperature interpretation is straightforward: as long as there is temperature drop along wellbore (Joule-Thomson cooling for gas well), there is fluid entering into the wellbore. Combined with other tools method, the temperature interpretation helps to reduce the uncertainty of the flow profile. The Emeraude result summarizes the flow rate from stage 1 to 10 as a whole, and from stage 11 to 15 it shows the closest agreement with temperature interpretation. **Table 4.2** lists the numerical results of the interpretation with all methods.

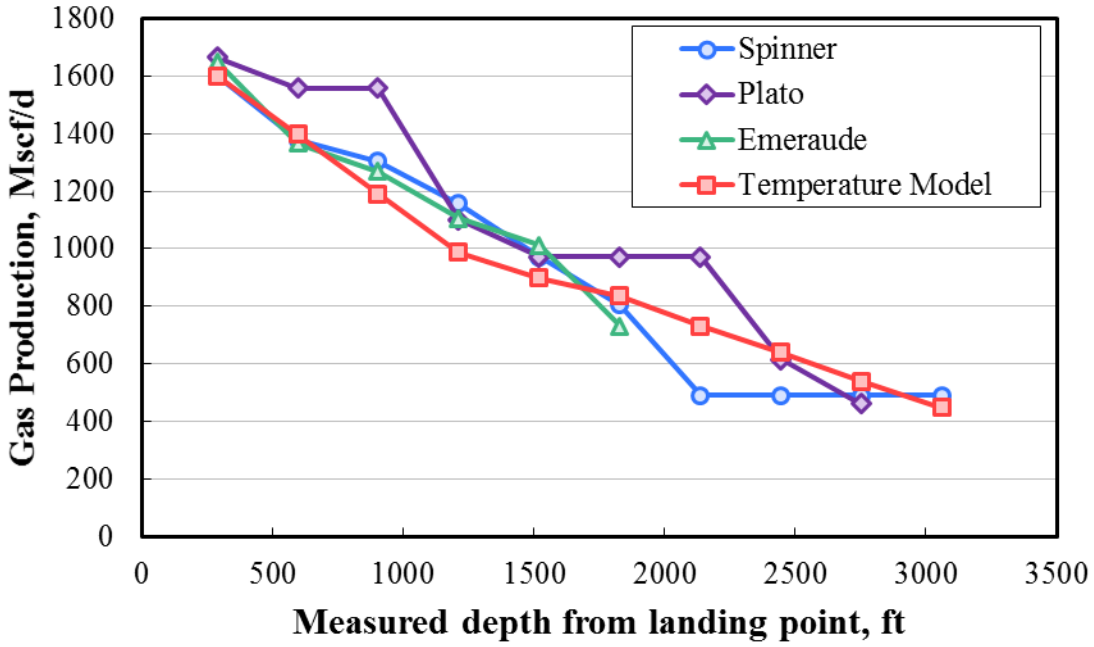

Fig. 4.5– Well EF-1 flow rate estimation along horizontal wellbore compare with other methods.

Table 4.2– Input data in Well EF-1 field case, numerical results.

Depth from landing point	**Stage**	**Spinner**		**Plato**		**Emeraude**		**Temperature model**	
ft		Mscf/d	%	Mscf/d	%	Mscf/d	%	Mscf/d	%
3061-4858	1-6	491	30.69	461	27.69			449	28.05
2753-3061	7	0	0					90.88	5.68
2445-2753	8	0	0	154	9.25	732	44.39	100.5	6.28
2137-2445	9	0	0	356	21.38			91.84	5.74
1829-2137	10	314	19.63	0	0			104.9	6.55
1521-1829	11	166	10.38	0	0	279	16.92	60.73	3.79
1213-1521	12	185	11.56	131	7.87	94	5.70	88.53	5.53
905-1213	13	148	9.25	455	27.33	163	9.88	204.07	12.75
597-905	14	74	4.63	0	0	99	6.00	207.66	12.97
289-597	15	222	13.88	108	6.49	282	17.10	202.67	12.66
	Total	1600	100	1665	100	1649	100	1600.78	100.00

The flow rate distribution of each stage is shown in **Fig. 4.6**. The fracture numbering start from the toe to the heel. We only have the temperature data from stage 7 to 15, corresponding fracture number 25 to 60, and that is the result presented in this paper.

If there are additional information about fracture half-length distribution (from fracture propagation model based on injection or/and from microseismic information), this flow rate could be further interpreted to fracture conductivity, especially if the temperature behavior is simulated during injection and shut-in periods. On the other hand, if assume that fracture conductivity is relatively constant for each fracture, we also can calculate the half-length of each fracture. This interpreted half-length can be compared with the fracture model prediction or microseismic data to better evaluate the created fractures. Further investigation is needed to isolate the effect of specific parameters if the temperature transient behavior is sensitive to the parameter.

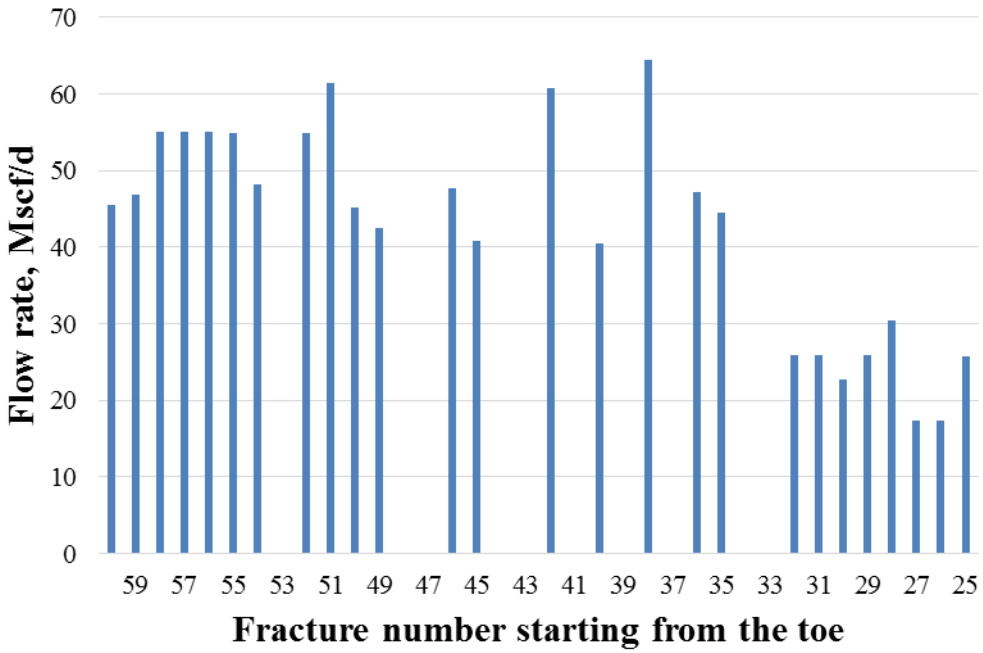

Fig. 4.6– Flow profile for Well EF-1 from stage 7 to 15.

4.3 Well EF-2

4.3.1 Well Information

Well EF-2 is a gas well that produces 1700 Mscf/d at the time of production logging. The water rate is 60 stb/d and the oil rate is 125 stb/d. Similar with Well EF-1, there is gas condensate in the wellbore. Since the Joule-Thomson effect of the oil and water is quiet small compared with gas phase, and also well EF-2 only produce a small amount of water and gas condensate, the single phase model was applied to the interpretation. The fluid heat conductivity as a volume-averaged value. The wellbore trajectory and perforation distribution are shown in **Fig. 4.7**. Notice that the wellbore was generally toe up, with a toe-down section around 3500 ft measured depth, and a sump at the location around 4500 ft measured depth, from the landing point. This can cause difficulty for PLT interpretation for a two phase flow well. There are six sets of production logging data (three up passes and three down passes) acquired during operation, as shown in **Fig. 4.8**. The average temperature is used to interpret flow profile.

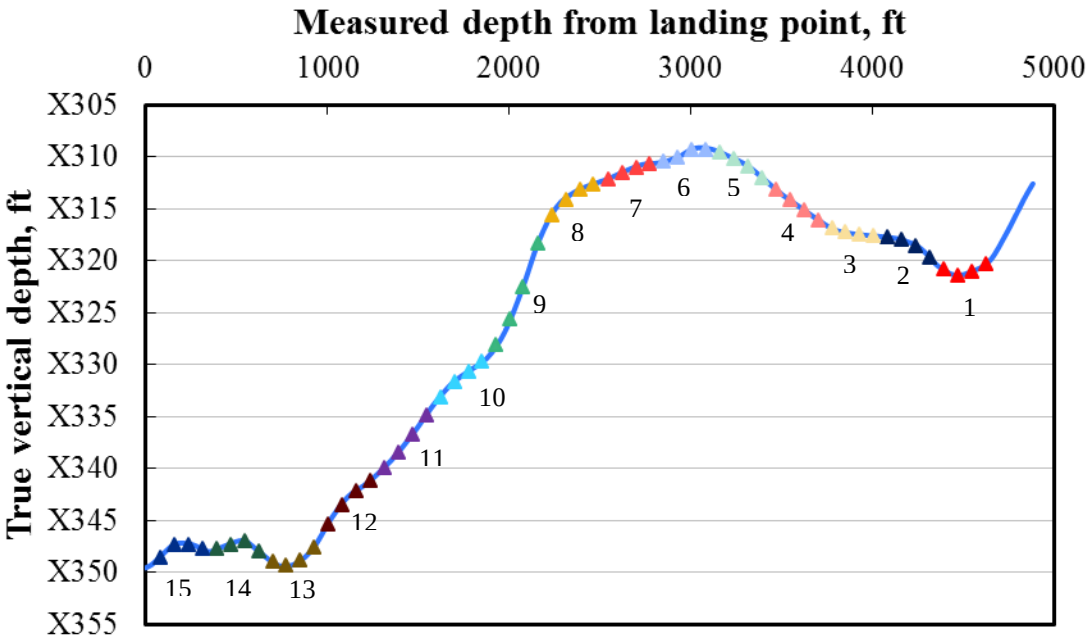

Fig. 4.7– Wellbore trajectory and designed perforation location for Well EF-2.

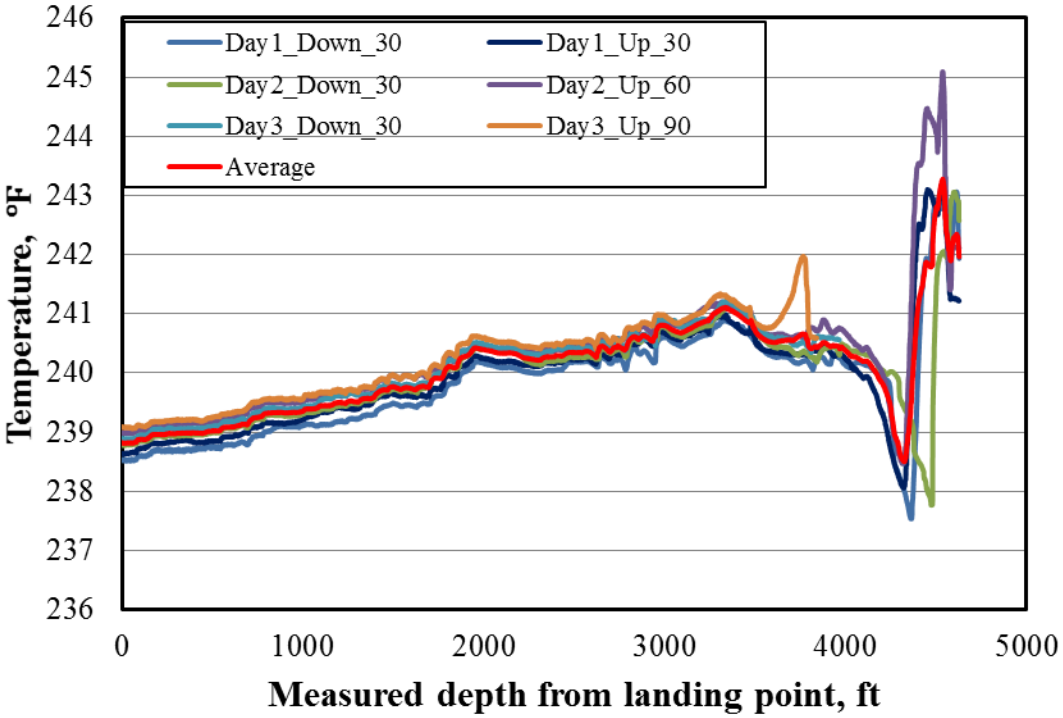

Fig. 4.8– PLT data sets for Well EF-2.

4.3.2 Simulated Results

Figure 4.9 shows the geothermal temperature, the observed temperature from PLT, and the matched temperature results from the temperature model. Notice that towards the toe, there is a sharp temperature change. The measured temperature is higher than the predicted geothermal temperature and drops quickly within stage 1 to below the geothermal temperature. Towards the toe, there are two phenomena happen; the end of the tool traveling may generate some temperature disturbing and well trajectory change (sump) will also contribute to the temperature change. The model does not consider the effect of the tool traveling towards the toe, but does include the trajectory/geothermal effect. To avoid the uncertainty caused by the tool traveling effect we started the interpretation from the point which has the temperature close to or lower than the geothermal temperature (4300 ft from the landing point). The large cooling effect may also be caused by a large fracture/more production at the location. It is believed that the wellbore fluid may flow backwards here because of the sump, water accumulation happens according to the logging analysis by the spinner array tool (Liao, et al., 2013). Combining all effects, the interpretation shows a relatively higher production at fracture 5, which is in stage 2.

The measured data near the heel is smooth but we can still observe small drops at fracture locations. Because the temperature keep decreasing towards the heel while the geothermal temperature is relatively flat in this case, it indicates a continuous gas inflow happening along the wellbore if the water inflow temperature is close to geothermal temperature (reasonable assumption). The heat conduction from formation is not enough to warm up the wellbore fluid, so the overall trend is downward.

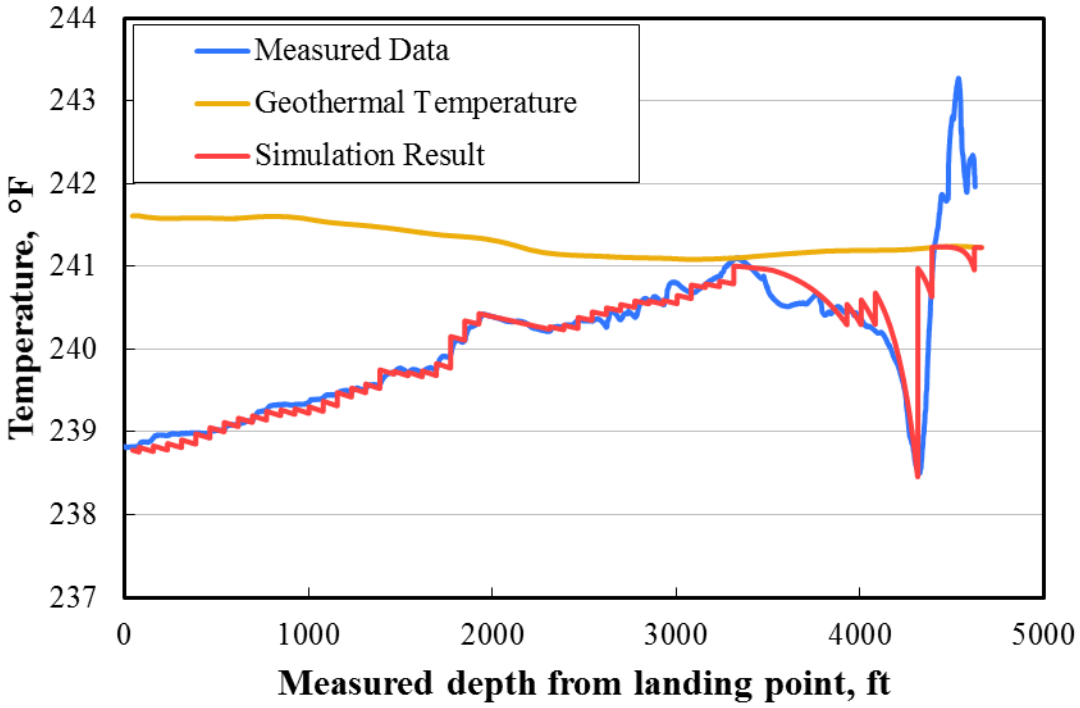

Fig. 4.9– Simulated and measured temperature data match for Well EF-2.

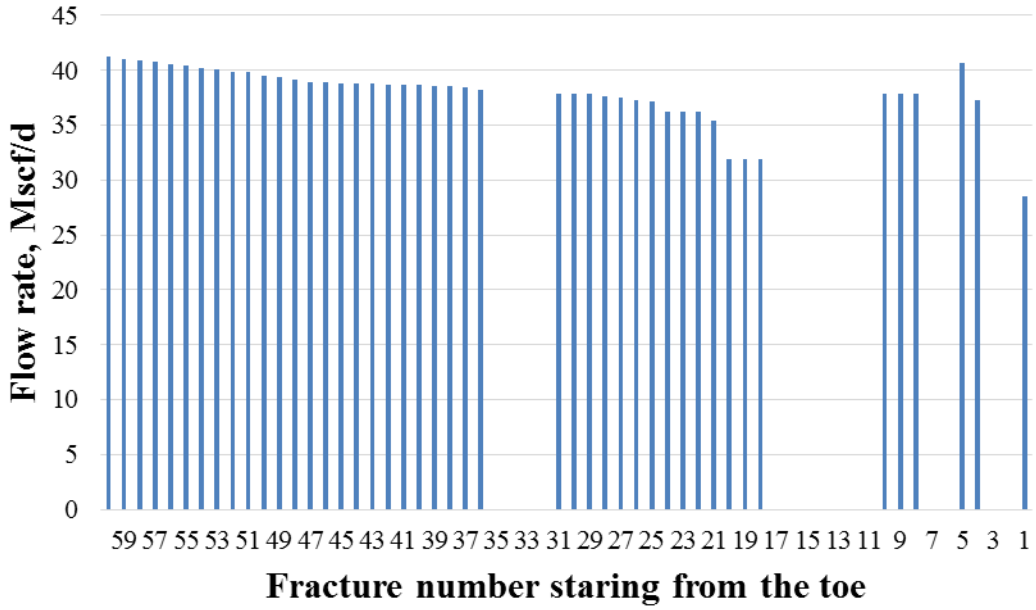

Fig. 4.10– Flow profile for Well EF-2.

The flow rate interpretation results by the developed temperature model and by the commercial software Emeraude are shown in **Fig. 4.11**. The Emeraude interpretation has both spinner data and temperature data, and for this well it is mainly based on spinner data. The results are overall consistent. The significant discrepancy happens at around 1000 ft and around 3500 ft. These are the two locations that the well trajectory has a down-slope. Because of the small bump at the location of around 1000 ft depth from the landing point, the interpretation by the PLT spinner becomes difficult. The existence of water sump may mask the effect of gas inflow and lead to a different interpretation as shown in **Fig. 4.11**. At 3500-ft location, the effect becomes more significant because the trajectory change is more pronounced than at 1000-ft location. The principle we used to interpret temperature measurement is to first detect if the fracture is existing from the sharp drop in temperature curve at each perforation location. If we ruled out the possibility of fracture existence, the heat convection from the reservoir to the wellbore is not considered. A critical mistake could happen when the combined subtle effects cancels the temperature change, resulting in a conclusion of no fracture. When the wellbore trajectory change is in one direction (either up or down), the interpretation is less uncertain. **Table 4.3** lists the numerical results of the interpretation from different methods.

The temperature interpretation method for fracture diagnosis has bigger advantage when the temperature is measured outside the producing liners by DTS than inside the wellbore by either DTS or PLT. The interpretation in such a case is less dependent on complex wellbore flow behavior caused by wellbore trajectory.

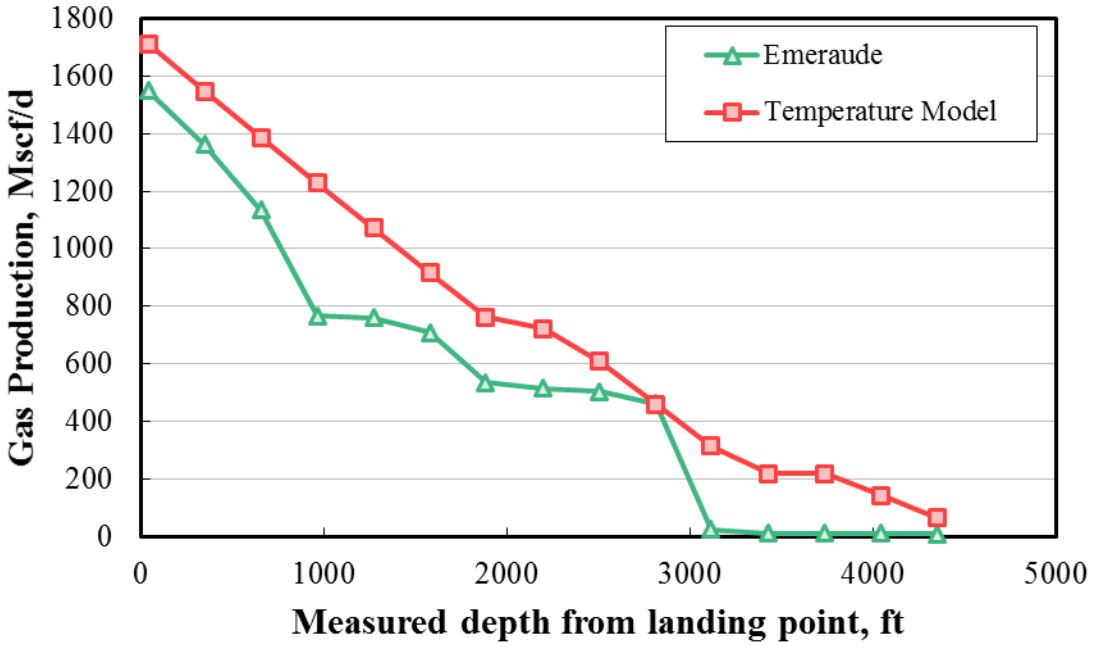

Fig. 4.11– Well EF-2 flow rate estimation along horizontal wellbore compare with other methods.

Table 4.3– Well EF-2 flow rate estimation by different methods.

Depth from landing point	**Stage**	**Emeraude**		**Temperature Model**	
ft		Mscf/d	%	Mscf/d	%
4624-4355	1	10	0.65	65.76	3.84
4355-4047	2	1.2	0.08	78.57	4.59
4047-3739	3	0.2	0.01	75.83	4.43
3739-3431	4	0.4	0.03	0.00	0.00
3431-3117	5	13.1	0.85	95.85	5.60
3117-2815	6	437.5	28.27	144.24	8.43
2815-2507	7	42.3	2.73	149.62	8.75
2507-2199	8	11.5	0.74	113.57	6.64
2199-1886	9	20.2	1.31	38.23	2.23
1886-1583	10	171.6	11.09	154.30	9.02
1583-1275	11	51.4	3.32	154.98	9.06
1275-967	12	7.6	0.49	155.87	9.11
967-659	13	367.2	23.73	158.69	9.28
659-351	14	227.4	14.69	161.19	9.42
351-43	15	186	12.02	163.93	9.58
	Total	1547.6	100	1710.6	100

4.4 Section Summary

In this study we have presented the application of a 2D semi-analytical model to two field cases. By matching the measured temperature data, we estimated the flow rate distribution along the wellbore, which is in good agreement with the estimated flow profile in most sections by other methods, and we discussed the reason for the discrepancy due to the flow pattern and well trajectory influence. The fracture locations are identified based on the measured temperature. The fracture diagnosis can help us to evaluate the effectiveness of fracture treatments and improve completion and fracture design. The advantage of the semi-analytical model is its efficiency when avoiding numerical simulation.

Based on the interpretation results we can conclude that the temperature drop when gas entering wellbore is more obvious at the toe with the same inflow rate. This is because after the fluid enters the wellbore, the upstream fluid inside the wellbore with higher temperature will warm the inflow stream up. At the toe, there is no upstream fluid. The upstream fluid inside the wellbore and the geothermal temperature will noticeably influence the wellbore temperature behavior.

5 FAST MARCHING METHOD IN THERMAL MODELING*

This section investigates the feasibility of applying Fast Marching Method (FMM) to solve the reservoir thermal model, which is an efficient way to handle reservoir heterogeneity and complex fracture geometry.

5.1 Introduction

In the past, models and methodologies have been developed for fracture diagnosis for multiple-stage fractured horizontal wells. They are based on either semi-analytical approach for simplicity or reservoir simulation for generality. The challenges are that semi-analytical models are not robust enough to describe complex fracture systems, while numerical simulation is computational expensive and impractical for inversion. To develop a comprehensive approach to translate temperature to flow profile, we adopted Fast Marching Method in simulating both heat transfer and velocity/pressure field in the interested domain (heterogeneous reservoir with multiple fractured horizontal wells). Fast Marching Method (FMM) is a new approach which is efficient in front tracking. Previous studies show a significant success in the investigation of pressure depletion behavior and shale gas production history match. By the nature of heat transfer in porous media, the thermal front propagation would lag behind pressure and the noticeable temperature change

* Reproduced with permission from "Fracture Diagnosis in Multiple Stage Stimulated Horizontal Well by Temperature Measurements Using Fast Marching Method." by Cui, J., Yang, C., Zhu, D., & Datta-Gupta, A. Paper SPE 174880 presented at the SPE Annual Technical Conference and Exhibition in Houston, Texas, 28-30 September. Copyright 2015 by the Society of Petroleum Engineers.

in reservoir only happens near hydraulic/natural fractures. FMM can be used to efficiently track the heat front that is associated with flow field.

The concept of FMM thermal modeling is based on the fast drainage volume calculation, followed by pressure approximation in terms of drainage volume derivative. Since the method already has a good application to predict transient pressure behavior and integrate shale gas production data (Xie, et al. 2015a, 2015b; Zhang et al. 2014), here we first review the approach of FMM and the pressure approximation, and then focus on the derivation of the thermal model. As the diffusive time of flight (DTOF, τ) incorporates the heterogeneity, we assume that the pressure gradient and the temperature gradient all align the same direction with the diffusive time of flight gradient.

5.2 Reservoir Flow Equation by FMM

The transient pressure response in a heterogeneous porous medium is governed by the diffusivity equation

$$\nabla \cdot \left(k(x,y,z)\nabla p(x,y,z,t)\right) = \phi(x,y,z)\mu c_t \frac{\partial p(x,y,z,t)}{\partial t} \tag{5.1}$$

where $p(x,y,z,t)$ is reservoir pressure, t is time, ϕ is porosity, $k(x,y,z)$ is permeability, μ is gas viscosity, and c_t is reservoir total compressibility. The following derivations use x for the (x,y,z) coordinate. Vasco et al. (2000) showed that the pressure front follows the propagation equation given by an Eikonal equation. By applying Fourier transform, the pressure wave in the frequency domain has a format of

$$\tilde{p}(x,\omega) = \frac{1}{\sqrt{2\pi}} \int_{-\infty}^{\infty} p(x,t) e^{i\omega t} d\omega \tag{5.2}$$

Combining **Eqs. 5.1** and **5.2**, the diffusivity equation in the frequency domain becomes

$$\nabla \cdot k(x)\nabla \tilde{p}(x,\omega) + i\omega\phi(x)\mu c_t \tilde{p}(x,\omega) = 0 \tag{5.3}$$

The above equation can be solved using an asymptotic approach, considering a solution format in terms of inverse powers of $\sqrt{-i\omega}$ (Vasco et al. 2000), the solution of **Eq. 5.3** is

$$\tilde{p}(x,\omega) = e^{-\sqrt{-i\omega}\tau(x)} \sum_{k=0}^{\infty} \frac{A_k(x)}{\left(\sqrt{-i\omega}\right)^k} \tag{5.4}$$

where $\tau(x)$ is the propagation time of the pressure front, and $A_k(x)$ is the pressure amplitude at kth order frequency which is still unknown and needs to be determined. Since we are only interested in the pressure front propagation which is captured by the highest frequency wave, and the solution is in terms of inverse power of $\sqrt{-i\omega}$, we are only interested in solving the first term of the asymptotic series (k=0 term), which is

$$\tilde{p}(x,\omega) = A_0(x) e^{-\sqrt{-i\omega}\tau(x)} \tag{5.5}$$

Taking 2nd derivatives of **Eq. 5.5**, substituting the derivative and **Eq. 5.5** into **Eq. 5.3**, and only collecting terms of the highest order in $\sqrt{-i\omega}$, we can arrive at a type of Eikonal equation for the pressure propagation front in terms of diffusive time of flight (DTOF), τ, as

$$\sqrt{\alpha(x)}\left|\nabla \tau(x)\right| = 1 \tag{5.6}$$

where α is the diffusivity, defined as

$$\alpha(x) = \frac{k(x)}{\phi(x)\mu c_t} \tag{5.7}$$

and $\tau(x)$ can be calculated by the following integral along the flow path

$$\tau(x) = \int_{x_0}^{x} \frac{1}{\sqrt{\alpha}} dx' \tag{5.8}$$

The detailed derivation of **Eq. 5.6** is in Appendix D. The above equation can be used to calculate $\tau(x)$. The key of fast speed calculation is that the solution at each node in the interested domain only depends on the smallest adjacent values of τ. Reservoir heterogeneity in permeability and porosity is expressed through the diffusivity α in **Eq. 5.7**.

To reduce the 3D equation to one dimensional equation, we assume that the pressure only depends on τ in space, which means that the contour surfaces of pressure are also the contour surfaces of τ. Based on this assumption, we have

$$\nabla p \approx \frac{\partial p}{\partial \tau} \nabla \tau = \frac{\partial p}{\partial \tau} \frac{1}{\sqrt{\alpha}} \hat{n}_\tau \tag{5.9}$$

where $\hat{n}_\tau$ is the unit normal vector to the contour of τ. Substituting **Eq. 5.9** into **Eq. 5.1**, we have

$$\nabla \cdot \left(\phi c_t \sqrt{\alpha} \frac{\partial p}{\partial \tau} \hat{n}_\tau \right) = \phi c_t \frac{\partial p}{\partial t} \tag{5.10}$$

According to the coordinate transform

$$\nabla \cdot \vec{F} = \frac{\partial F_x}{\partial x} + \frac{\partial F_y}{\partial y} + \frac{\partial F_z}{\partial z} = \frac{1}{h_\tau h_\varphi h_\chi} \left(\frac{\partial \left(h_\varphi h_\chi F_\tau \right)}{\partial \tau} + \frac{\partial \left(h_\tau h_\chi F_\varphi \right)}{\partial \varphi} + \frac{\partial \left(h_\tau h_\varphi F_\chi \right)}{\partial \chi} \right) \tag{5.11}$$

Where h_τ, h_φ and h_χ are the length of the covariant vectors. In case that pressure is independent to φ and χ then $h_\varphi = h_\chi = 1$ and h_τ can calculated by

$$h_\tau = \sqrt{\left(\frac{\partial x}{\partial \tau} \right)^2 + \left(\frac{\partial y}{\partial \tau} \right)^2 + \left(\frac{\partial z}{\partial \tau} \right)^2} = \sqrt{\alpha} \tag{5.12}$$

This leads to

$$\frac{1}{h_\tau h_\varphi h_\chi}\frac{\partial}{\partial\tau}\left(\phi c_t h_\varphi h_\chi\sqrt{\alpha}\frac{\partial p}{\partial\tau}\right)=\phi c_t\frac{\partial p}{\partial t} \tag{5.13}$$

using the Jacobian $J= h_\tau h_\varphi h_\chi$, the above equation can be written as

$$\frac{\partial}{\partial\tau}\left(J\phi\frac{\partial p}{\partial\tau}\right)=J\phi\frac{\partial p}{\partial t} \tag{5.14}$$

At particular values of DTOF, τ, the drainage volume of the pressure propagation can be easily measured by adding up all the pore volume of cells which has been visited at that moment

$$V_p(\tau)=\int_{\tau_0}^{\tau}\left(\iint\phi J(\tau,\varphi,\chi)d\varphi d\chi\right)d\tau \tag{5.15}$$

Then the derivative of the drainage volume, $w(\tau)$, is

$$w(\tau)=\frac{dV_p(\tau)}{d\tau}=\iint\phi J(\tau,\varphi,\chi)d\varphi d\chi \tag{5.16}$$

Combining **Eqs. 5.14** and **5.16**, the pressure equation becomes a 1D equation as

$$\frac{\partial}{\partial\tau}(w(\tau)\frac{\partial p}{\partial\tau})=w(\tau)\frac{\partial p}{\partial t} \tag{5.17}$$

At any given time, we calculate DTOF, τ, from **Eq. 5.8**, then drainage volume, $V_p(\tau)$, from **Eq. 5.15**. This will give us $w(\tau)$ by **Eq. 5.16**. With $w(\tau)$ value, **Eq. 5.17** can be solved numerically to generate the profile of pressure wave front in the domain.

For gas reservoir, starting from the diffusive equation considering reservoir compressibility (Zhang et al., 2014),

$$\nabla\cdot(\frac{p}{\mu Z}k\nabla p)=\phi\frac{p}{Z}c_t\frac{\partial p}{\partial t} \tag{5.18}$$

where the total compressibility is defined as

$$c_t=c_g+c_r=\frac{1}{\rho}\frac{\partial\rho}{\partial p}+\frac{1}{\phi}\frac{d\phi}{dp} \tag{5.19}$$

Similarly, we can obtain the following transformed equation

$$\frac{\partial}{\partial \tau}(w(\tau)\frac{p}{\tilde{\mu}Z}\frac{\partial p}{\partial \tau}) = w(\tau)\frac{p\tilde{c}_t}{Z}\frac{\partial p}{\partial t} \tag{5.20}$$

where Z is gas compressibility factor, $\tilde{\mu}$ and $\tilde{c}_t$ are the dimensionless viscosity and total compressibility defined by the ratio of the local value to the initial value. **Eq. 5.17** or **Eq. 5.20** is then solved numerically. Because this formula is in 1D domain, the computation is extremely fast, compared to solving fluid flow in fully 3D domain.

5.3 Reservoir Thermal Equation by FMM

Starting with the energy balance equation in the porous media derived in Section 2, which is

$$\overline{\rho\hat{C}_p}\frac{\partial T}{\partial t} - \phi\beta T\frac{\partial p}{\partial t} = \rho\frac{k}{\mu}\cdot\hat{C}_p\nabla p\nabla T - \frac{k}{\mu}(\beta T - 1)\cdot(\nabla p)^2 + K_T\nabla^2 T \tag{5.21}$$

where T is temperature, ρ is fluid density, $\hat{C}_p$ is fluid heat capacity, β is gas expansion coefficient, and K_T is thermal conductivity of the media.

Using the same concept as presented in the pressure equation **Eq. 5.6**, we have

$$|\nabla\tau| = \frac{1}{\sqrt{\alpha}} \tag{5.22}$$

Here we assume that DTOF, τ, for the pressure wave calculated by the reservoir diffusivity can be used for the temperature wave also. This assumption is reasonable for convectional heat transfer in heterogeneous reservoirs because convective heat is caused by flow, which is directly controlled by reservoir properties. The flow velocity will be the highest at the highest permeability/porosity path, resulting the highest temperature change along the same path. This assumption may not be accurate for conductive heat transfer because if assume that solid rock has higher heat capacity than the fluids filled in the porous

medium, then conductive heat flows slower in the high porosity path. Permeability does not impact the heat conduction. For flow dominated thermal problem, the assumption is acceptable. With the assumption that the pressure gradient and temperature gradient align with τ gradient direction, the pressure and temperature derivative can be written as

$$\nabla p \approx \frac{\partial p}{\partial \tau}\nabla \tau = \frac{\partial p}{\partial \tau}\frac{1}{\sqrt{\alpha}}\hat{n}_\tau \tag{5.23}$$

$$\nabla T \approx \frac{\partial T}{\partial \tau}\nabla \tau = \frac{\partial T}{\partial \tau}\frac{1}{\sqrt{\alpha}}\hat{n}_\tau \tag{5.24}$$

where $\hat{n}_\tau$ is the unit normal vector to the contour of τ.

Substituting **Eqs. 5.12**, **5.13** and **5.7** into **Eq. 5.11**, we have

$$\begin{aligned}&\overline{\rho\hat{C}_p}\frac{\partial T}{\partial t} - \phi\beta T\frac{\partial p}{\partial t}\\ &= \rho\phi c_t \cdot \hat{C}_p\left(\frac{\partial p}{\partial \tau}\hat{n}_\tau\right)\left(\frac{\partial T}{\partial \tau}\hat{n}_\tau\right) - \phi c_t(\beta T - 1)\cdot\left(\frac{\partial p}{\partial \tau}\hat{n}_\tau\right)^2 + K_T\nabla\cdot\left(\frac{\partial T}{\partial \tau}\cdot\frac{1}{\sqrt{\alpha}}\hat{n}_\tau\right)\end{aligned} \tag{5.25}$$

Transforming the coordinate system from (x,y,z) to (τ, φ,χ), realizing that temperature is function of τ only, following the same derivation in the pressure equation, we can rewrite the temperature equation as

$$\begin{aligned}&\overline{\rho\hat{C}_p}\frac{\partial T}{\partial t} - \phi\beta T\frac{\partial p}{\partial t}\\ &= \rho\hat{C}_p\phi c_t\frac{\partial T}{\partial \tau}\frac{\partial p}{\partial \tau} - (\beta T - 1)\phi c_t\left(\frac{\partial p}{\partial \tau}\right)^2 + \frac{K_T\phi}{w(\tau)}\frac{\partial}{\partial \tau}\left(\frac{w(\tau)}{\phi\alpha}\frac{\partial T}{\partial \tau}\right)\end{aligned} \tag{5.26}$$

The boundary conditions are constant bottomhole pressure constraint, and convection boundary condition at the wellbore. In the new coordinate system, they have the expression

$$p\big|_{\tau=\tau_w} = p_{wf} \tag{5.27}$$

$$K_T\frac{1}{\sqrt{\alpha}}\frac{\partial T}{\partial \tau} + h(T - T_w) = 0 \tag{5.28}$$

where h is heat transfer coefficient, T_w is the wellbore temperature and p_{wf} is bottomhole pressure.

The outer boundary is no-flow boundary condition with constant initial reservoir temperature T_i, which are

$$\left(w(\tau) \frac{p}{\tilde{\mu} Z} \frac{\partial p}{\partial \tau} \right)_{\tau \to \infty} = 0 \tag{5.29}$$

$$T\big|_{\tau \to \infty} = T_i \tag{5.30}$$

Equation 5.26 is solved numerically after calculate $w(\tau)$ at each time step with τ calculated by **Eq. 5.22**.

5.4 Model Validation

We use a single fracture, homogeneous formation case to validate the method comparing with a semi-analytical method to solve pressure and rate, then a finite difference method to solve the reservoir 2D thermal model (Cui and Zhu, 2014). **Fig. 5.1** shows the fracture geometry, and **Fig. 5.2** shows the gridding system of fracture. We assumed that the horizontal well does not contribute to flow, only the fracture does. **Tables 5.1** shows the parameters need in the example, and fluid/rock properties are the same as **Table 2.2** shows.

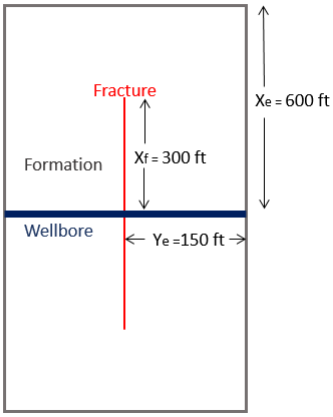

Fig. 5.1– Fracture geometry in 2D.

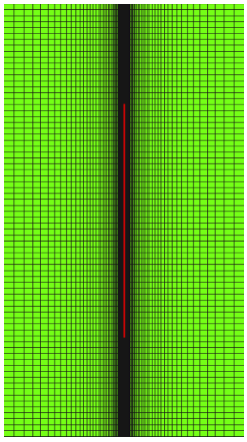

Fig. 5.2– Fracture gridding system.

Table 5.1– Key parameters for model validation.

Formation		Fracture	
Net Pay Thickness, ft	160	Fracture width, in	0.24
Permeability, nD	580	Fracture permeability, Darcy	1
Porosity, %	5	Fracture porosity, %	0.2
Pore pressure, psi	4400	Fracture half-length, ft	300
Initial temperature, °F	238.4		
Total compressibility, 1/psi	1.74E-04		
Bottomhole pressure, psi	2600		

In FMM modeling, starting from fracture locations, we use logarithmic grid along the wellbore direction and uniform grid along the fracture direction, comparing with local-refined grid in finite difference method. We define an arriving temperature as the fluid temperature at the intersection of fracture and wellbore before entering wellbore, and thus the mixing with wellbore fluid can be neglected. If temperature sensors are installed outside casing, we can measure the arriving temperature. This is only for DTS application when the cable is installed outside the casing. When the sensors are inside the wellbore, a wellbore energy balance equation need to be considered. **Fig. 5.3** shows the comparison of

the arriving temperature results by FMM and conventional numerical simulation (the solution of thermal equation). **Fig. 5.4** shows the corresponding flow rates calculated by FMM and the semi-analytical model (the solution of the flow equation). The FMM predicts a slightly faster flow rate decline, but a slower temperature increase at early time. This difference is attributed to the grid discretization effect in calculating drainage volume, and the accumulated inaccuracy in pressure estimation. Since we are interested in long-term temperature and flow rate prediction, the early-time error is insignificant. In general, FMM calculated the arriving temperature matches the results from the finite difference method, and the computational time for the one-fracture case is about 20 times faster comparing with the conventional simulation.

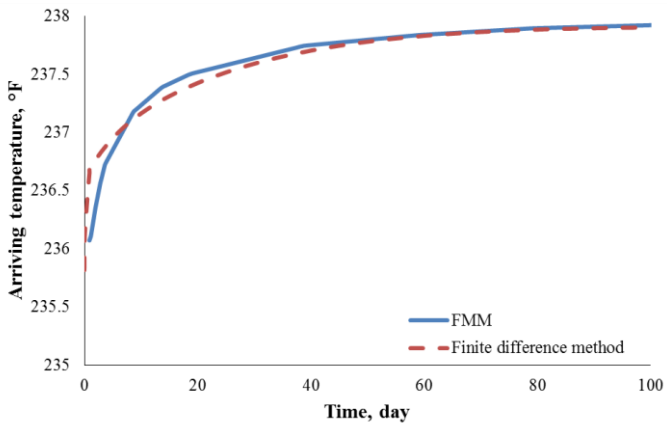

Fig. 5.3– Arriving temperature with time.

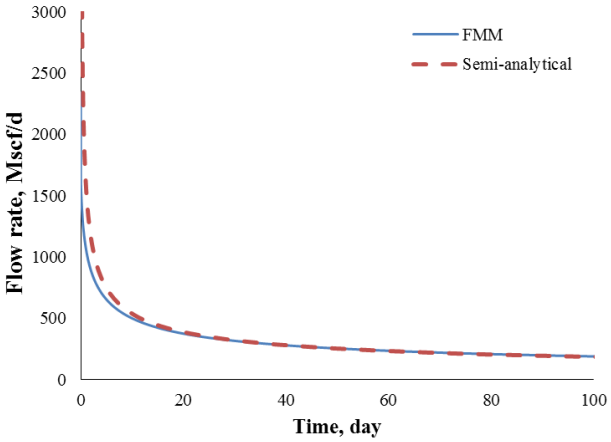

Fig. 5.4– Production rate with time.

5.5 Model Application

We use several examples to show the calculated transient temperature behavior during production for a horizontal well with multiple fractures. The base-case example has 10 uniform hydraulic fractures along a horizontal wellbore in a homogeneous reservoir. We then change some of the fracture half-lengths to illustrate how the arriving temperature responds to non-uniform fractures. Finally, we consider the reservoir heterogeneity and add nature fractures around the hydraulic fractures.

With multiple fractures in a homogeneous reservoir, we need to calculate τ and the drainage volume for each fracture. Starting from the first fracture, we calculate τ_1 and therefore V_{p1}. This is the volume that contributes to Fracture 1 flow. Then we calculate τ_2 from the second fracture, and identify V_{p2}. If there is a common volume for both Fracture 1 and Fracture 2, we need to distribute the flow of these common grids to the two fractures. At this time, we compare τ_1 and τ_2 of each grid. If $\tau_1 > \tau_2$, then the grid contributes to Fracture 2, otherwise the grid contributes to Fracture 1. Notice this is not necessary for homogeneous reservoir with uniform fractures because the drainage volume for each

fracture is identical. For the common grids, the flow rate is splitted between the two fractures equally. Repeat this procedure until the τ propagates from the last fracture is calculated. The pressure and temperature behaviors are solved within the drainage volume dominated by each corresponding fracture.

5.5.1 Uniform Hydraulic Fractures

The schematic of the example is shown in **Fig. 5.5**. There are 10 uniform fractures with 300-ft half-length along a horizontal wellbore. We assume that only the fractures contribute to gas production. The hydraulic fractures are assumed fully penetrating in the vertical direction. The horizontal wellbore is 3700 ft long, and the fracture spacing is 300 ft. All other parameters are the same as the ones in the model validation section. Since the fractures all have the same geometry, for a homogeneous formation, the fractures should produce at same rate when assume that there is no pressure drop in the wellbore (a reasonable assumption for low-perm gas reservoir). The flow rate distribution for such a well at 10 days, 30 days, 60 days and 90 days are shown in **Fig. 5.6**.

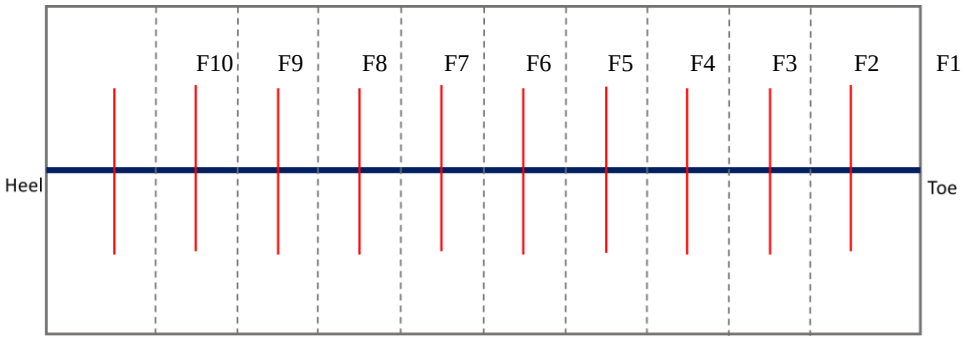

Fig. 5.5– Uniform hydraulic fractures along horizontal wellbore.

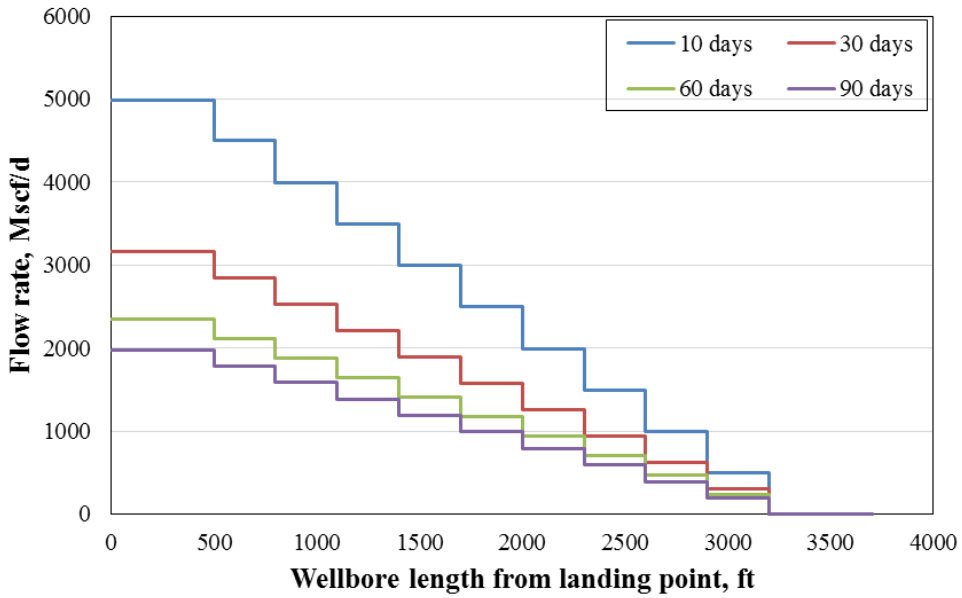

Fig. 5.6– Flow rate distribution along horizontal wellbore for uniform fractures.

With the flow rate distribution, we used FMM to predict arriving temperature at each specified time along the well, and **Fig. 5.7** shows the results. The two dominated heat transfer effects are Joule-Thomson cooling caused by pressure drawdown, and conduction heating by the temperature difference between formation and fracture. At early-time production, the arriving temperature at the fracture locations is dominated by Joule-Thomson cooling because of higher drawdown. As the flow rate declines, the effect of conduction heating becomes more announced on the arriving temperature, the temperature decreasing becomes less. **Fig. 5.8** shows the τ, pressure and temperature distribution after one year production. The thermal front is lagging behind the pressure front (compare **Fig. 5.8b** with **Fig. 5.8c**).

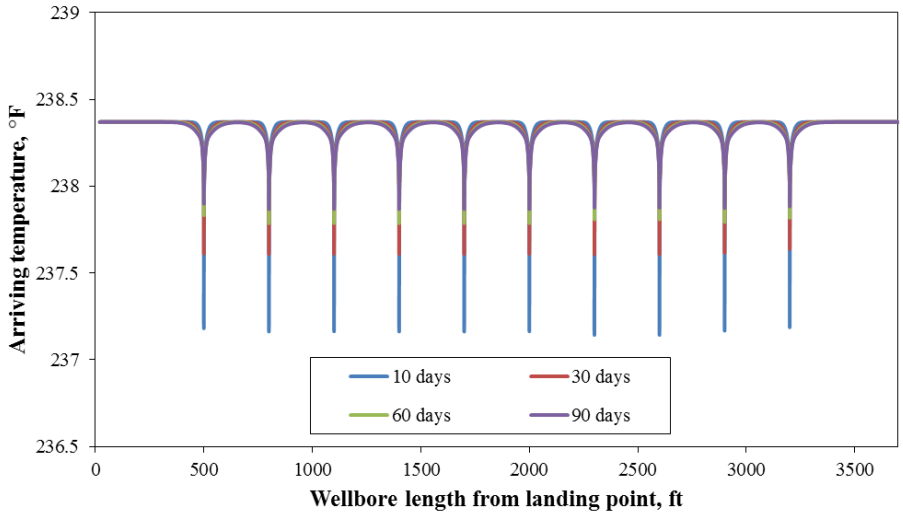

Fig. 5.7– Arriving temperature distribution along horizontal wellbore at different time (uniform fractures).

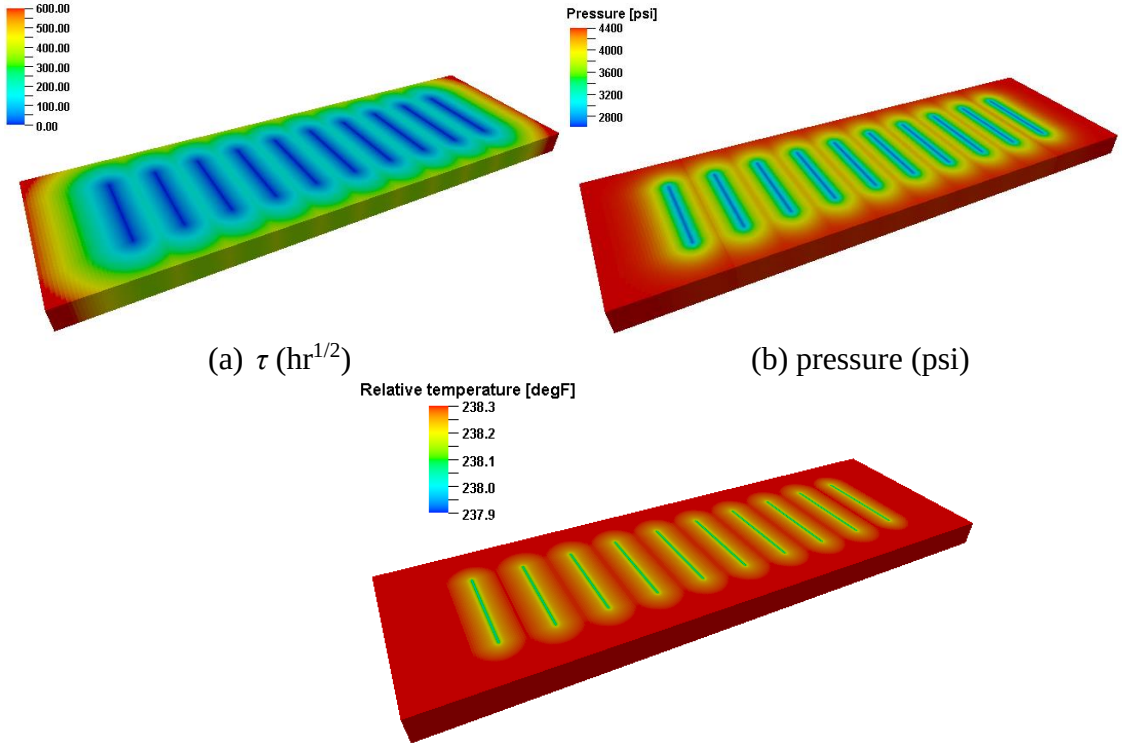

(a) τ ($hr^{1/2}$) (b) pressure (psi)

(c) temperature (°F)

Fig. 5.8– Simulation results for uniform fractures after one year production.

5.5.2 Non-uniform Hydraulic Fractures

For non-uniform fractures, the schematic of modeled system is shown in **Fig. 5.9**. The longer fracture half-lengths are 320 ft and the shorter ones are 250 ft. All other parameters are kept the same as in the previous example. For the fractured well, the flow rate distribution at different time is shown in **Fig. 5.10**. The corresponding arriving temperature for the system is shown in **Fig. 5.11**. **Fig. 5.12** shows the diffusive time of flight, pressure, and temperature distribution after one year of production. In shale gas reservoirs, fracture half-length is critical for gas production. When it changes, the arriving temperature at the wellbore changes correspondingly. But there are many other parameters which also influence the arriving temperature, such as formation permeability and thermal properties of rock/fluid. The combination and uncertainty of all these parameters causes the solution of arriving temperature non-unique, interpretation of fracture half-length from the temperature measurements is extremely challenge. From temperature distribution, we can see the overall response of temperature to the flow rate distribution. Separating the effect of fracture half-length by temperature measurements alone from all other parameters is impossible. Comparing **Fig. 5.11** to **Fig. 5.7**, at least that temperature does respond to fracture half-length change. This is also observed from **Fig. 5.12 c**.

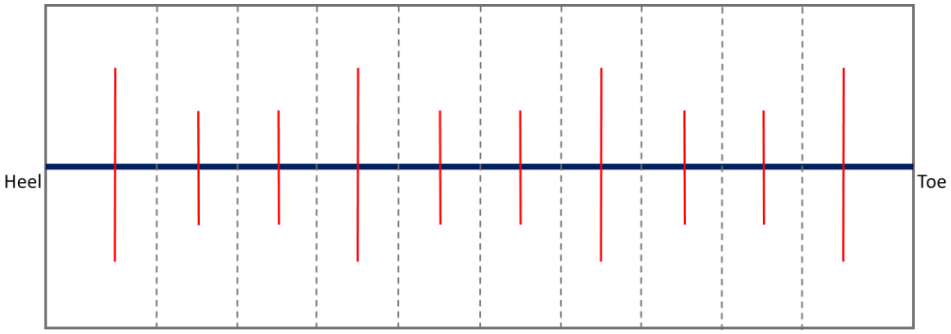

Fig. 5.9– Non-uniform hydraulic fractures along horizontal wellbore.

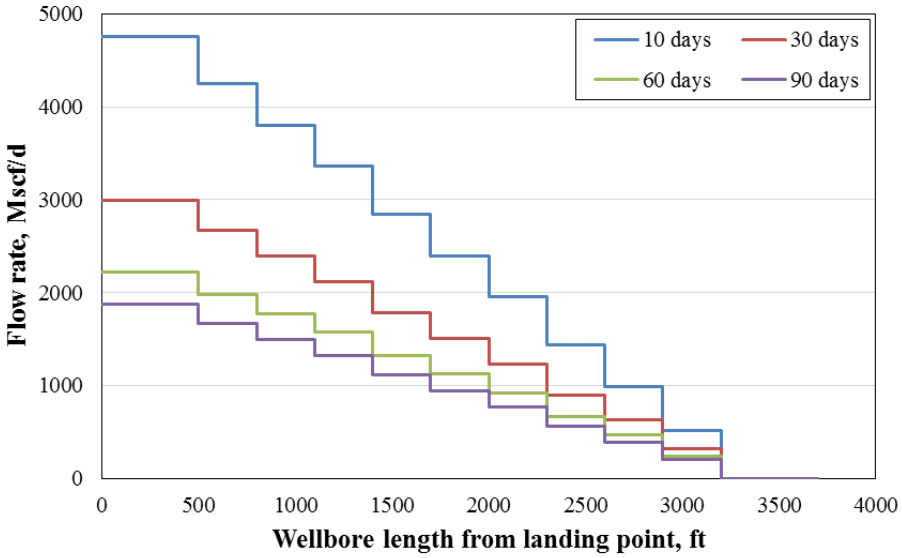

Fig. 5.10– Flow rate distribution along horizontal wellbore at different time (non-uniform fractures).

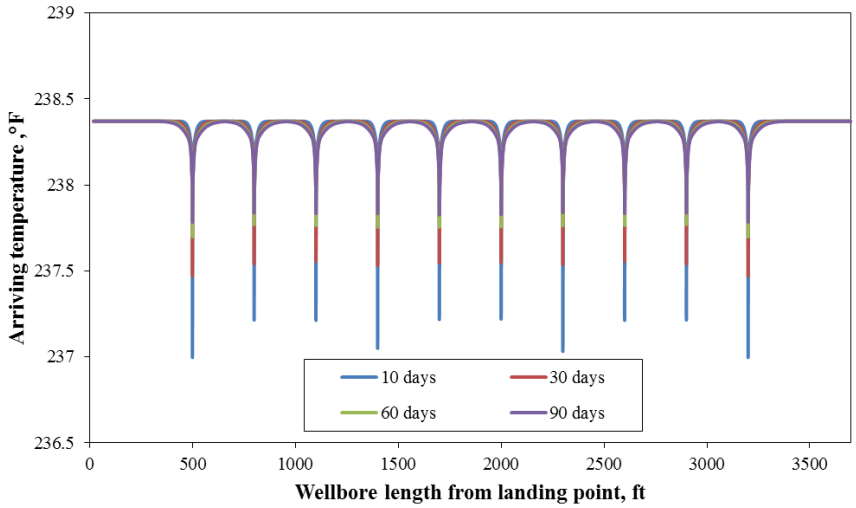

Fig. 5.11– Arriving temperature distribution along horizontal wellbore at different time (non-uniform fractures).

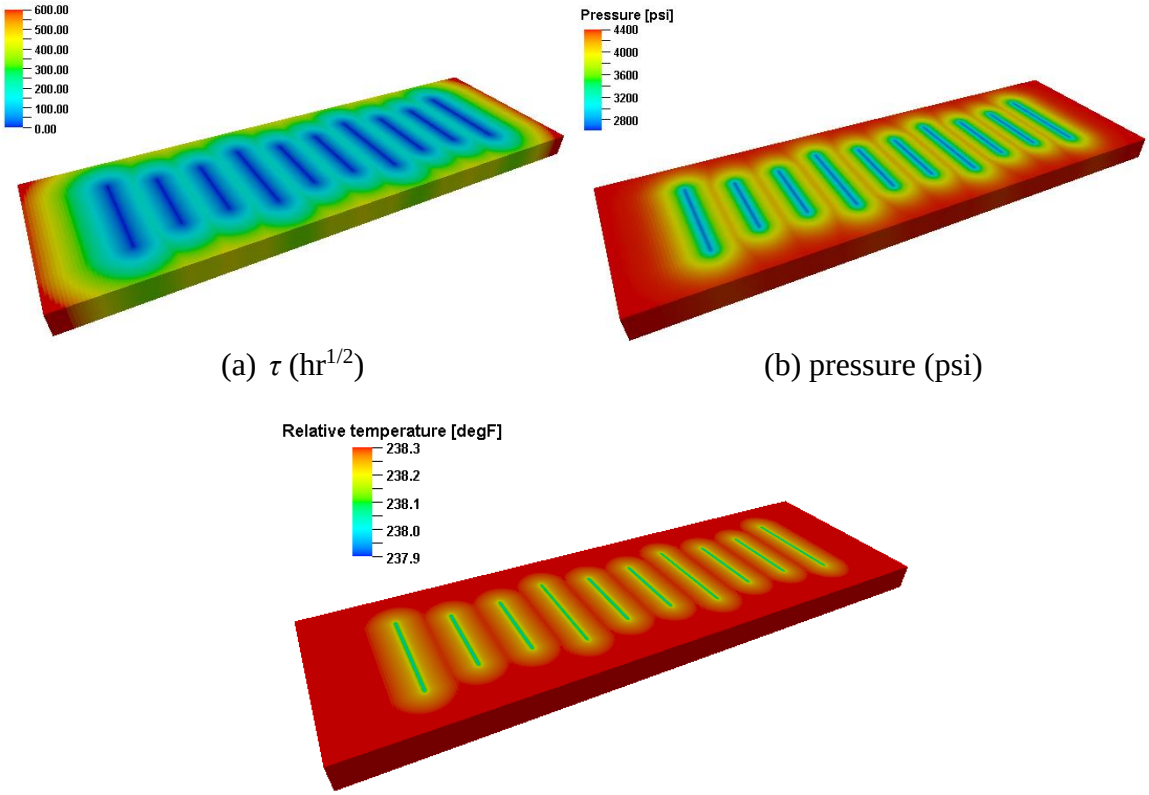

(a) τ ($hr^{1/2}$) (b) pressure (psi)

(c) temperature (°F)

Fig. 5.12– Simulation results for non-uniform fractures after one year production.

5.5.3 Heterogeneous Reservoir with Uniform Hydraulic Fractures

We apply FMM combined with the temperature solution to a heterogeneous reservoir with an arithmetic average permeability about 580 nD. The model contains (about 4.4 million) grids to give high resolution, the uniform grid size is 1 ft in both the *x* and *y* directions, and 160 ft in the *z* direction. The horizontal well has 10 fractures as described in the first example. The well produces with a constant bottomhole pressure at 2600 psi. Additional fracture and fluid properties are the same with the uniform fractures case. **Fig. 5.13** shows the permeability map for this heterogeneous case.

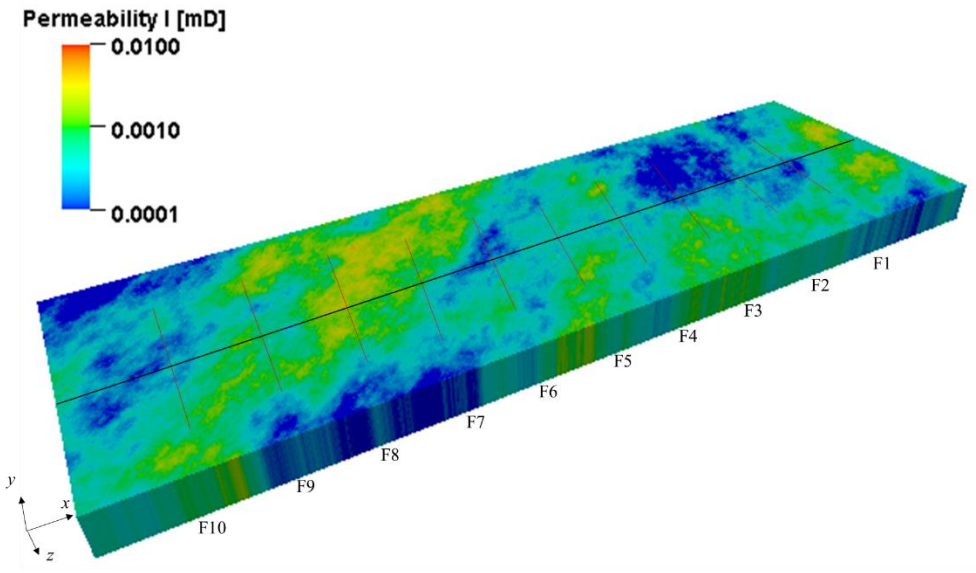

Fig. 5.13– Reservoir permeability distribution in FMM modeling.

Figure 5.14 shows the flow rate distributions along horizontal wellbore, and **Fig. 5.15** is the corresponding temperature distributions at different times. There are distinct higher formation permeability region around the 8th fracture (1100 ft in the *x*-direction). With higher flow rate, the arriving temperature is lower because of more cooling. Also noticed is that the temperature front propagates into the formation faster in the high permeability zone.

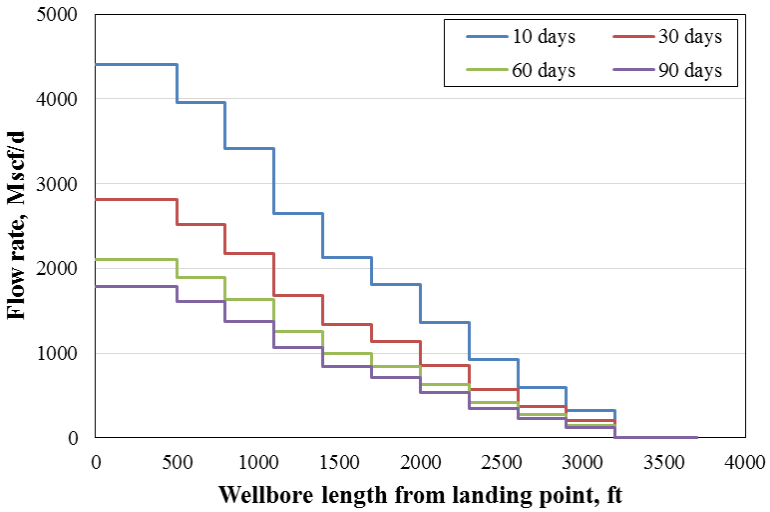

Fig. 5.14– Arriving temperature distribution along horizontal wellbore at different time (uniform fractures, heterogeneous reservoir).

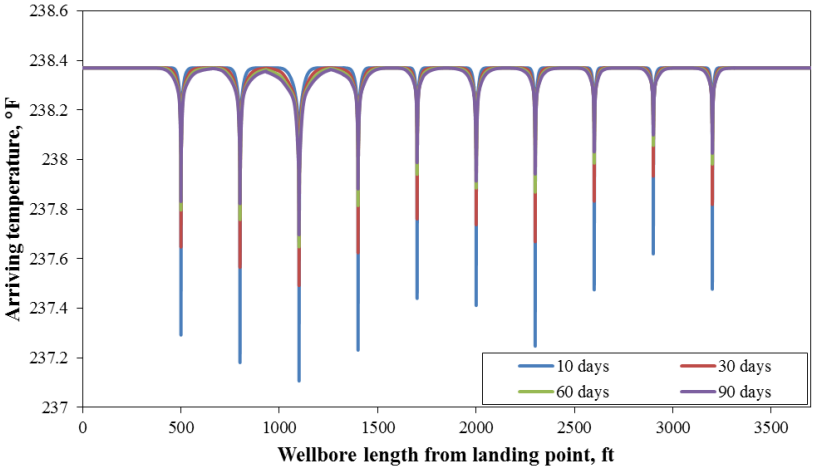

Fig. 5.15– Flow rate distribution along horizontal wellbore at different time (uniform fractures, heterogeneous reservoir).

Figure 5.16 illustrates the τ and pressure distribution after one year of production. **Fig. 5.17** is the temperature distribution at one month (**Fig. 5.17a**) and one year (**Fig. 5.17b**) of production. Notice that when reservoir is heterogeneous, low temperature band is wider at the higher permeability locations (Fracture 8 compare with others, for example). 2D

temperature distribution helps to identify the parameters that causes temperature change. As production goes on, the temperature variation from the original reservoir temperature becomes more announced.

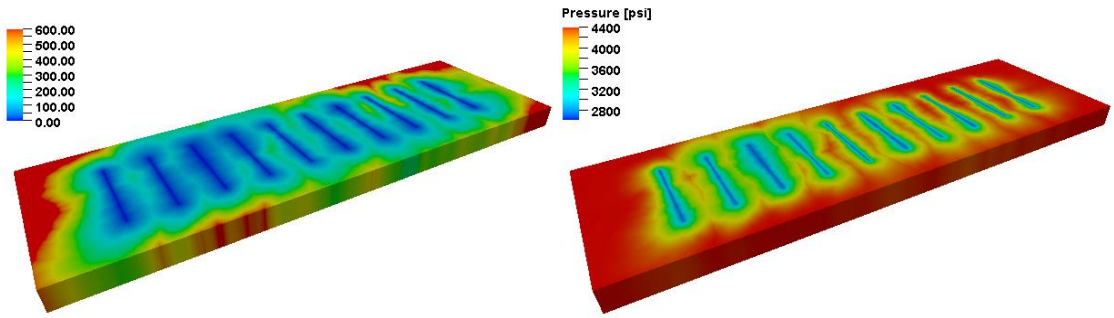

(a) τ ($hr^{1/2}$) (b) pressure (psi)

Fig. 5.16– Simulation results for heterogeneous reservoir.

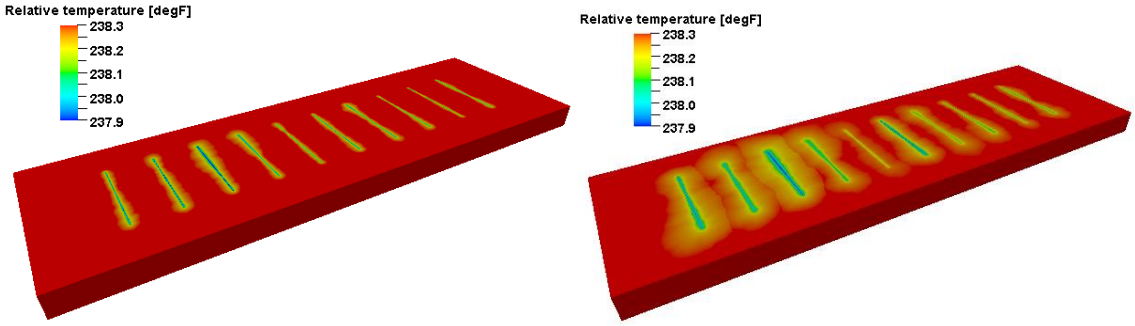

(a) temperature (°F) at one month (b) temperature (°F) at one year

Fig. 5.17– Temperature for heterogeneous reservoir.

5.5.4 Heterogeneous Reservoir with Random Natural Fractures and Uniform Hydraulic Fractures

In this case, we add 10 natural fractures in additional to the primary hydraulic fractures. The non-orthogonal natural fractures are represented by zig-zag grids, and the conductivity of the natural fractures is 0.2 md-ft. We use the same rock and fluid properties

as before. **Fig. 5.18** shows the geometry of the system simulated. From the picture, we can see that most of the natural fractures are directly connected to the hydraulic fractures while few natural fractures (NF1, NF2 and NF6) are not connected to hydraulic fractures.

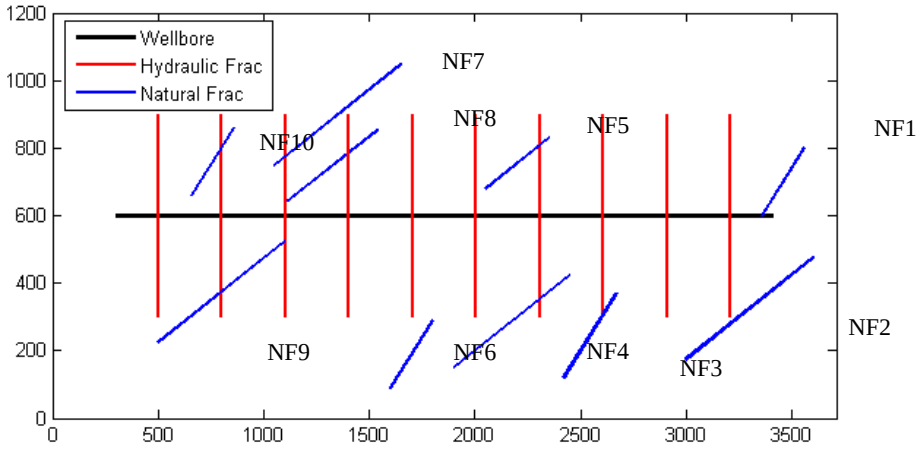

Fig. 5.18– Geometry of hydraulic fractures and natural fractures in FMM modeling.

Figure 5.19 shows the flow rate and **Fig. 5.20** is the temperature distributions at different time steps. **Fig. 5.21** illustrates the τ and pressure distributions after one year production. Large flow rate occurs at the hydraulic fractures at the beginning of production, causing the quick temperature drop inside the hydraulic fractures. Later in the production, the temperature drop spreads gradually in the regions near both hydraulic and natural fractures, indicating more reservoir volume is involved in flow. Fracture 8 has the highest temperature respond (**Fig. 5.20**), caused by both high-permeability location and near-by natural fractures (NF7, NF8 and NF9). **Fig. 5.22** shows the temperature profile for one month and one year of production. Eventhough both τ plot (**Fig. 5.21 a**) and pressure plot (**Fig. 5.21 b**) show the unconnected natural fractures effect (NF1 and NF6), the effect of these unconnected natural fractures do not show up on the temperature plot (**Fig. 5.22**).

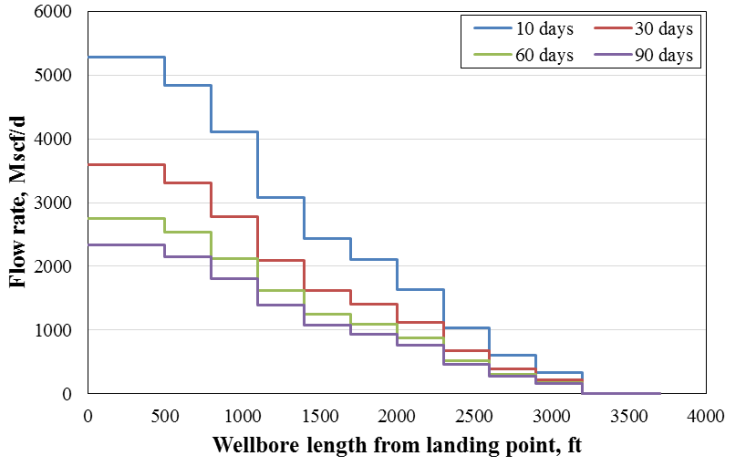

Fig. 5.19– Flow rate distribution along wellbore at different time (uniform fractures with nature fractures, heterogeneous reservoir).

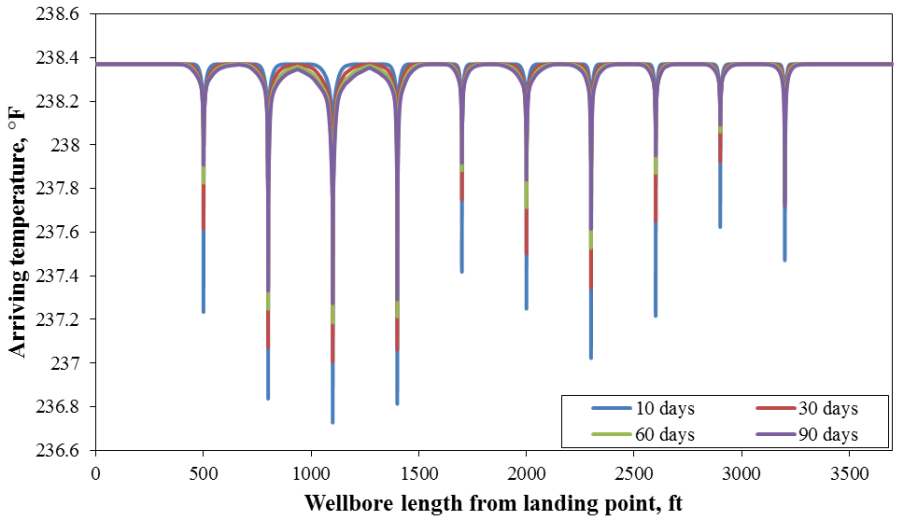

Fig. 5.20– Arriving temperature distribution along wellbore at different time (uniform hydraulic fractures with nature fractures, heterogeneous reservoir).

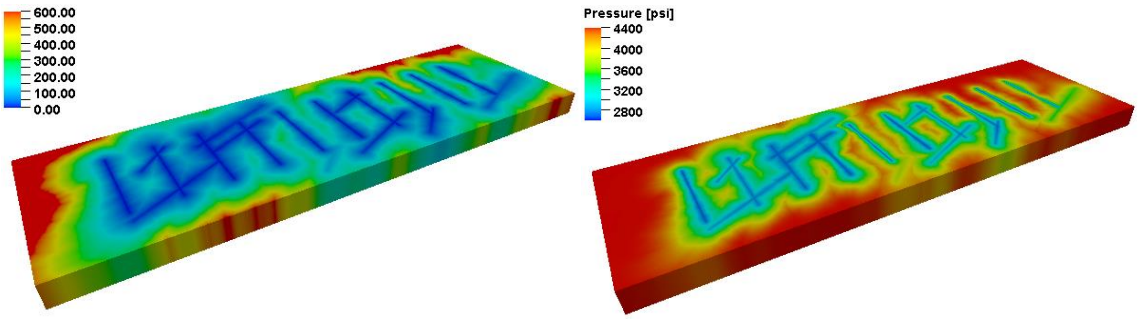

(a) τ ($hr^{1/2}$) (b) pressure (psi)

Fig. 5.21– Simulation results for heterogeneous reservoir nature fractures.

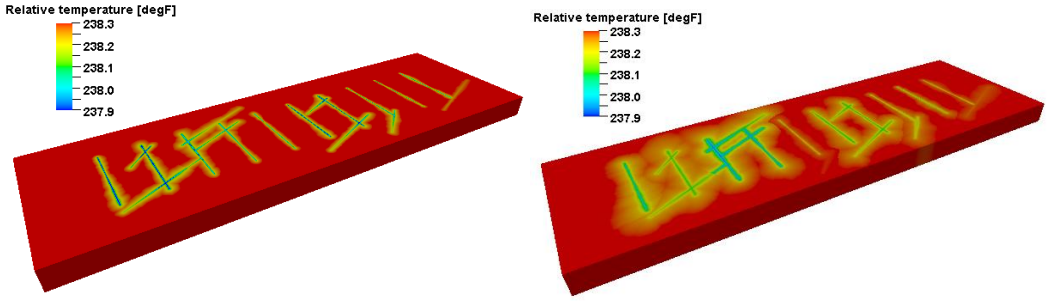

(a) temperature (°F) at one month (b) temperature (°F) at one year

Fig. 5.22– Temperature for heterogeneous reservoir with nature fractures.

Figures 5.23 and **5.24** show the comparison of the gas production rate and arriving temperature with or without natural fractures at 8th hydraulic fracture location. There are three natural fractures connected with this fracture, NFs 7, 8 and 9. Also noticed that Fracture 8 is located in a high-permeability zone. With natural fractures, the flow rate is higher, so the temperature drop is faster. The arriving temperature is directly related to the production rate at the locations where temperature is measured. From the arriving temperature alone, it is hard to tell if the production is from a larger hydraulic fracture or from the connected natural fractures. The temperature contour in **Fig. 5.22** illustrates the temperature changes caused by both hydraulic fractures and natural fractures. Even this contour is not generated directly from the downhole sensor measurements, the model and

methods developed from this section have the ability to generate such a temperature profile. This is a useful information in the inversion process to help identifying the connectivity of natural fractures.

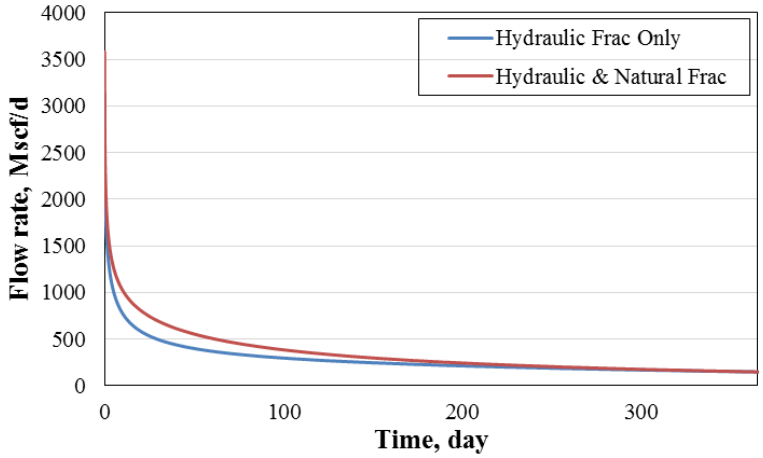

Fig. 5.23– Comparison of gas production rate with and without natural fractures.

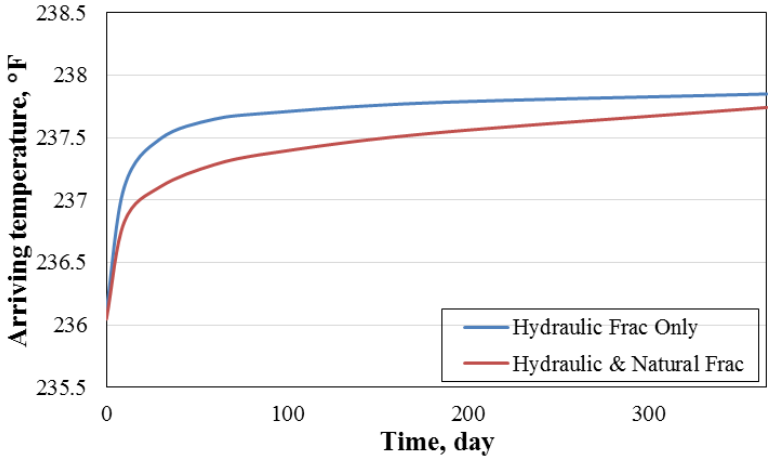

Fig. 5.24– Comparison of arriving temperature at wellbore with and without natural fractures.

5.6 Section Summary

In this section we present the derivation of reservoir thermal model in 1D coordinate using the concept of diffusive time-of-flight, and apply FMM to obtain the dynamic pressure and temperature distribution in fractured horizontal well system. By the examples in a homogeneous reservoir, we illustrated that the arriving temperature at the intersection of fracture and wellbore is related to the fracture inflow and the volume size of the fracture. The fracture locations can be identified by temperature measurement along horizontal wellbore. When flow rate is high, Joule-Thomson cooling effect is more obvious, and the temperature arriving at the wellbore is low. As flow rate decline with production time, the arriving temperature increases gradually. This helps us to accurately evaluate the efficiency of hydraulic fracture treatment and give suggestion for re-frac design if applicable. For the heterogeneous reservoir and nature fractures example, we just indicate the influence of the formation permeability variation and nature fractures on the arriving temperature. Accurate geologic information of the reservoir makes the temperature interpretation more practical.

The power and intuition of fast marching method have been illustrated by generating the temperature map during production. The advantage of FMM is its versatility to handle heterogeneous reservoir and complex fracture geometry, at the same time it only needs several minutes to simulate the pressure and temperature behavior. This section is just a fundamental study of the FMM application to thermal modeling, and further research is important to get solid understanding in this area.

6 CONCLUSIONS AND RECOMMENDATIONS

6.1 Conclusions

In this dissertation a coupled fracture/formation/wellbore model was established to predict the transient temperature behavior in multiple-fractured horizontal well during long-term production period. The main purpose of the research is to diagnose the efficiency of hydraulic fracture stimulation by estimating the production flow profile along the wellbore.

In the mathematical modeling part, first the tri-linear model is adopted to semi-analytically solve the fluid flow domain in a fracture system in shale/tight reservoirs. This model could be applied for single phase oil or gas wells. For gas well, the non-Darcy effects could be considered by permeability alteration using minimum permeability plateau. Then the fracture/formation flow model is coupled with a 1D wellbore model to obtain the velocity and pressure distribution along wellbore considering sectional inflow from fractures. After we get a converged flow field, the thermal model calculates the heat transfer in the fracture/formation/wellbore system considering subtle temperature changes caused by heat convection, heat conduction, the Joule-Thomson effect and viscous dissipation. Both the simplified semi-analytical solution and the finite difference solution are presented to solve the transient thermal equation in porous media.

In this study, synthetic examples are illustrated to investigate the transient temperature behavior under different inner boundary constraints. The mechanisms for the temperature variation are discussed in detail. By varying some key parameters, we showed

how the key parameters would affect the flow rate thus change the temperature distribution inside wellbore.

The established model is applied to match the field data and demonstrate the feasibility of using temperature data to diagnose fractured well performance during production. We estimate the flow rate distribution and compare it with the flow profile interpreted by PLT measurements (spinner meter) and commercial software. This practical study helps us to test the established model and shows a promising way to reduce the uncertainty of flow profiling when combined with other interpretation methods.

A new approach (Fast Marching Method) to simulate reservoir temperature is proposed to consider the reservoir heterogeneity and complex fracture geometry with high efficiency. The modeling process would enhance the understanding of temperature behavior when we can access to more detailed reservoir information. Further study is needed on this topic.

Based on the mathematical modeling and the discussions in this research, the important conclusions are summarized below:

(1) The coupled fracture/formation and wellbore model is able to capture the major characteristics of the flow and thermal behavior during the transient production period. The temperature change happens near and inside the fractures, and the decisive phenomenon is Joule-Thomson cooling effect due to gas expansion.

(2) When the production begins, we could consider the situation as constant flow rate case first then gradually transit to constant bottom hole pressure case during long-term period. For constant flow rate constraint, the transient pressure behavior would dominate the temperature variation at the wellbore since the convection/conduction

ratio do not change in the reservoir. For constant bottomhole pressure constraint, the flow rate decline with production time makes the temperature increases gradually. Based on this, we could use the temperature signal to interpret flow profile along the wellbore.

(3) The fracture properties such as conductivity and effective fracture half-length would have significant influence on the transient pressure behavior or the flow rate contribution, and the transient temperature behavior is sensitive to these key parameters. Combined with other fracture diagnosis technologies, this modeling work may help to reduce the uncertainty of the key parameters, but cannot determine them until now.

(4) For field temperature data interpretation, the model can interpret the flow profile along the wellbore when the flow rate decline stabilized during long-term production. The geothermal temperature variation due to wellbore trajectory is critical for the accurate interpretation result.

(5) Compared with the interpretation result by spinner meter, the temperature method shows a more continuous flow distribution, since it is less influenced by the flow pattern in the wellbore. Based on the flow rate distribution, we could diagnose the hydraulic fracture stimulation efficiency along the wellbore, thus helps the re-fracturing design.

(6) Fast Marching Method shows high efficiency in reservoir flow/thermal modeling, further study are needed to validate and improve the model considering complex fracture geometry.

6.2 Limitations and Recommendations

Further studies are needed to extend the scope of this work. Limitations of this study are summarized and recommendations for future study are also listed as follow:

(1) In order to do the history matching of the wellbore temperature based on the production rate and pressure variation at the wellbore, the superposition method should be adopted for the transient pressure simulation. The semi-analytical solution for the reservoir thermal model would be efficient for the history matching if the solution can be extended to dynamic flow rate production.

(2) For the finite difference method to solve the formation thermal model, logarithmic grid system is recommended along the flow direction in order to improve the accuracy and efficiency of the computation.

(3) For the inversion problem (known the wellbore temperature distribution to determine the flow profile), the mixing effect after the fluid coming into the wellbore would cause the difficulty for the data matching. It is recommended that select the data points where the mixing effect is already diminished for the inversion.

REFERENCES

Al-Hadhrami, A.K., Elliott, L., Ingham, D.B. and Wen, X. 2003. Flows through horozontal channels of porous materials. *International Journal of Energy Research*, 27(10): 875-889.

App, J.F., and Yoshioka, K. 2011. Impact of Reservoir Permeability on Flowing Sandface Temperatures. Paper SPE 146951 presented at the SPE Annual Technical Conference and Exhibition, Denver, Colorado, U.S.A.

Arthur, A., Michael, W., Abdullah, A., and Sergey, A. 2013. Evaluating Injection Performance with High-precision Temperature Logging and Numerical Temperature Modeling. Paper SPE 166007 presented at the SPE Reservoir Characterization and Simulation Conference and Exhibition, Abu Dhabi, UAE.

Barree, R.D., Fisher, M.K., and Woodroof, R.A. 2002. A Practical Guide to Hydraulic Fracture Diagnostic Technologies. SPE 77442 presented at the SPE Annual Technical Conference and Exhibition, San Antonio, Texas.

Bird, R.B., Stewart, W.E., and Lightfoot, E.N. 1960. *Transport Phenomena*. First Edition. Wiley, New York.

Cui, J., and Zhu, D. 2014. Diagnosis of Multiple Fracture Simulation in Horizontal Wells by Downhole Temperature Measurements. Paper IPTC 17700 presented at the International Petroleum Technology Conference, Doha, Qatar.

Cui, J., Zhu, D., and Jin, M. 2014. Diagnosis of Multi-Stage Fracture Simulation in Horizontal Wells by Downhole Temperature Measurements. Paper SPE 170874 presented at the SPE Annual Technical Conference and Exhibition, Amsterdam, The Netherlands.

Cui, J., Yang, C., Zhu, D. and Datta-Gupta, A. 2015. Fracture Diagnosis in Multiple Stage Stimulated Horizontal Well by Temperature Measurements Using Fast Marching Method. Paper SPE 174880 presented at the SPE Annual Technical Conference and Exhibition held in Houston, Texas.

Davis, E.R., Zhu, D., and Hill, A.D. 1995. Interpretation of Fracture Height from Temperature Logs-The Effect of Wellbore/Fracture Separation. Paper SPE 29588 presented at the Rocky Mountain Region/Low-Permeability Reservoirs Symposium, Denver, Colorado, U.S.A.

Emeraude Tutorial, Edition 02. 2012. KAPPA Inc., Sophia Antipolis, France.

Hasan, A.R. and Kabir, C.S. 1991. Heat Transfer During Two-Phase Flow in Wellbores: Part I – Formation Temperature. Paper SPE 22866 presented at the SPE Annual Technical Conference and Exhibition, Dallas.

Hill, A.D. 1990. *Production Logging–Theoretical and Interpretive Elements*. Monograph Series, SPE, Richardson, Texas.

Holley, E.H., Molenaar, M.M., Fidan, E., and Banack, B. 2013. Interpreting Uncemented Multistage Hydraulic-Fracturing Completion Effectiveness By Use of Fiber-Optic DTS Injection Data. *SPE Drilling & Completion*, 28(3): 243-253.

Holley, E.H., Jones, T.A., Dodson, J., and Salazar, J. 2014. Using Distributed Optical Sensing to Constrain Fracture Models and Confirm Reservoir Coverage in Permian Basin. Paper SPE 168610 presented at the SPE Hydraulic Fracturing Technology Conference, The Woodlands, Texas.

Kabir, C.S., Izgec, B., and Hason, A.R. 2008. Real-Time Estimation of Total Flow Rate and Flow Profiling in DTS-Instrumented Wells. Paper IPTC 12343 presented at the International Petroleum Technology Conference, Kuala Lumpur, Malaysia.

Lee, S. and Brockenbrough, J.R. 1986. A New Approximate Analytic Solution for Finite-Conductivity Vertical Fractures. *SPE Formation Evaluation*, 1(1): 75-88.

Li, Z., and Zhu, D. 2009. Predicting Flow Profile of Horizontal Well by Downhole Pressure and DTS Data for Water-Drive Reservoir. Paper SPE 124873 presented at the SPE Annual Technical Conference and Exhibition, New Orleans, Louisiana, U.S.A.

Meyer, B.R., Bazan, L.W., Jacot, R.H., and Lattibeaudiere, M.G. 2010. Optimization of Multiple Transverse Hydraulic Fractures in Horizontal Wellbores. Paper SPE 131732 presented at the SPE Unconventional Gas Conference, Pittsburgh, Pennsylvania, U.S.A.

Muradov, K.M. and Davies, D.R. 2011. Novel Analytical Methods of Temperature Interpretation in Horizontal Wells. Paper SPE 131642 presented at the SPE EUROPEC/EAGE Annual Conference and Exhibition, Barcelona, Spain.

Obinna, O.D. and Roland, N.H. 2008. Modeling Reservoir Temperature Transients and Reservoir-Parameter Estimation Constrained to the Model. Paper SPE 115791 presented at the SPE Annual Technical Conference and Exhibition, Denver, Colorado, U.S.A.

Peacock, D.R. 1965. Temperature Logging. Paper presented at Society of Professional Well Log Analysis Annual Logging Symposium, Dallas, Texas.

Plato Tutorial, Edition 01. 2008. Interpretive Software Products Inc., Houston, TX.

Ramey, H.J.Jr. 1962. Wellbore Heat Transmission. *Journal of Petroleum Technology*, 14(4): 427-435.

Sagar, R., Doty, D.R., and Schmidt, Z. 1991. Predicting Temperature Profiles in a Flowing Well. *SPE Production Engineering*, 6(04): 441-448.

Sethian, J. A. 1999. *Level Set Methods and Fast Marching Methods*. New York City: Cambridge University Press.

Stehfest, H. 1970. Numerical Inversion of Laplace Transform. *Communication of the ACM*, 13(01): 47-49.

Sui, W., Ehlig-Economides, Zhu, D., and Hill, A.D. 2010. Determining Multilayer Formation Properties from Transient Termperature and Pressure Measurements in Commingled Gas Wells. Paper SPE 131150 presented at CPS/SPE International Oil & Gas Conference and Exhibition, Beijing, China.

Sui, W., Zhu, D., Hill, A.D., and Ehlig-Economides 2008. Determining Multilayer Formation Properties from Transient Temperature and Pressure Measurements. Paper SPE 116270 presented at the SPE Annual Technical Conference and Exhibition, Denver, Colorado, U.S.A.

Xie, J., Yang, C., Gupta, N., King, M., & Datta-Gupta, A. 2015. Depth of Investigation and Depletion in Unconventional Reservoirs With Fast-Marching Methods. *SPE Journal*, 20(04): 831-841.

Xie, J., Yang, C., Gupta, N., King, M. J., & Datta-Gupta, A. 2014. Integration of Shale-Gas-Production Data and Microseismic for Fracture and Reservoir Properties With the Fast Marching Method. *SPE Journal*, 20(02): 347-359.

Zhang, Y., Yang, C., Gupta, N., King, M. J. et al. 2013. Fast Marching Methods for Complex Grids and Anisotropic Permeabilities: Application to Unconventional Reservoirs. Paper SPE 163637 presented at the SPE Reservoir Simulation Symposium held in the Woodlands, Texas.

Yoshida, N., Zhu, D., and Hill, A. D. 2014. Temperature-Prediction Model for a Horizontal Well with Multiple Fractures in a Shale Reservoir. *SPE Production & Operation*, 29 (04): 261-273.

Yoshioka, K., Zhu, D., Hill, A.D. Dawkrajai, P., and Lake, L.W. 2005. A Comprehensive Model of Temperature Behavior in a Horizontal Well. Paper SPE 95656 presented at the SPE Annual Technical Conference and Exhibition, Dallas, Texas.

Yoshioka, K., Zhu, D., Hill, A.D., Dawkrajai, P., and Lake, L.W. 2007. Prediction of Temperature Changes Caused by Water or Gas Entry into a Horizontal Well. *SPE Production & Operation*, 22(04): 425-433.

APPENDIX A

Finite Difference Equation for Wellbore Model

The wellbore mass, momentum and energy balance equations are all solved numerically by finite difference method. The gridding system is shown as **Fig 2.1**.

Since the fluid inside wellbore starts flowing from the toe towards the heel, we could use backward difference method. The mass balance equation can be discretized as

$$\frac{\rho_i^{n+1}-\rho_i^n}{\Delta t}=\frac{2\gamma}{R}\left(\rho_I v_I\right)_i-\frac{\rho_i^{n+1}v_i^{n+1}-\rho_{i-1}^{n+1}v_{i-1}^{n+1}}{\Delta z_{i-1/2}} \tag{A-1}$$

Thus the velocity at the i^{th} grid could be obtained by

$$v_i^{n+1}=\frac{\rho_{i-1}^{n+1}v_{i-1}^{n+1}}{\rho_i^{n+1}}-\frac{\Delta z_{i-1/2}}{\rho_i^{n+1}}\left(\frac{\rho_i^{n+1}-\rho_i^n}{\Delta t}-\frac{2\gamma}{R}\left(\rho_I v_I\right)_i\right) \tag{A-2}$$

The momentum equation after discretization is

$$\begin{aligned}\frac{p_i^{n+1}-p_{i-1}^{n+1}}{\Delta z_{i-1/2}}=&-\frac{\left(\rho f v^2\right)_i^{n+1}}{R}-\left(\rho v\right)_{i-1/2}^{n+1}\frac{v_i^{n+1}-v_{i-1}^{n+1}}{\Delta z_{i-1/2}}-\frac{2\gamma}{R}\left(\rho_I v_I v\right)_{i-1/2}^{n+1}\\&-\left(\rho g\sin\theta\right)_{i-1/2}-\frac{\left(\rho v\right)_i^{n+1}-\left(\rho v\right)_i^n}{\Delta t}\end{aligned} \tag{A-3}$$

So the pressure can be calculated as

$$\begin{aligned}p_i^{n+1}=p_{i-1}^{n+1}-\Delta z_{i-1/2}\Bigg[&\frac{\left(\rho f v^2\right)_i^{n+1}}{R}+\left(\rho v\right)_{i-1/2}^{n+1}\frac{v_i^{n+1}-v_{i-1}^{n+1}}{\Delta z_{i-1/2}}\\&+\frac{2\gamma}{R}\left(\rho_I v_I v\right)_{i-1/2}^{n+1}+\left(\rho g\sin\theta\right)_{i-1/2}+\frac{\left(\rho v\right)_i^{n+1}-\left(\rho v\right)_i^n}{\Delta t}\Bigg]\end{aligned} \tag{A-4}$$

The energy balance equation can be written as

$$\begin{aligned}
&\frac{1}{v_i^{n+1}}\frac{T_i^{n+1}-T_i^{n}}{\Delta t}-\frac{\beta_i^{n}T_i^{n+1}}{v_i^{n+1}\left(\rho\hat{C}_p\right)_i^{n}}\frac{p_i^{n+1}-p_i^{n}}{\Delta t}\\
&=\frac{2\gamma}{R}\frac{\left(\rho_I v_I\right)_i^{n+1}}{\left(\rho v\right)_i^{n+1}}\left(T_I-T\right)_i^{n+1}+\frac{2\left(1-\gamma\right)}{Rv_i^{n+1}\left(\rho\hat{C}_p\right)_i^{n}}U_T\left(T_I-T\right)_i^{n+1}\\
&-\frac{T_i^{n+1}-T_{i-1}^{n+1}}{\Delta z_{i-1/2}}+\frac{\beta_i^{n}T_i^{n+1}-1}{\left(\rho\hat{C}_p\right)_i^{n}}\frac{p_i^{n+1}-p_{i-1}^{n+1}}{\Delta z_{i-1/2}}-\frac{\left(g\sin\theta\right)_i}{\hat{C}_p}
\end{aligned}\tag{A-5}$$

Solve the temperature we could get

$$\begin{aligned}
T_i^{n+1}=&\left[\frac{1}{v_i^{n+1}\Delta t}+\frac{2\gamma}{R}\frac{\left(\rho_I v_I\right)_i^{n+1}}{\left(\rho v\right)_i^{n+1}}+\frac{2\left(1-\gamma\right)}{Rv_i^{n+1}\left(\rho\hat{C}_p\right)_i^{n}}U_T+\frac{1}{\Delta z_{i-1/2}}\right.\\
&\left.-\frac{\beta_i^{n}}{\left(\rho\hat{C}_p\right)_i^{n}}\frac{p_i^{n+1}-p_{i-1}^{n+1}}{\Delta z_{i-1/2}}-\frac{\beta\left(p_i^{n+1}-p_{i-1}^{n+1}\right)}{v_i^{n+1}\left(\rho\hat{C}_p\right)_i^{n}\Delta t}\right]^{-1}\cdot\left\{\frac{1}{\Delta z_{i-1/2}}T_{i-1}^{n+1}\right.\\
&+\left[\frac{2\gamma}{R}\frac{\left(\rho_I v_I\right)_i^{n+1}}{\left(\rho v\right)_i^{n+1}}+\frac{2\left(1-\gamma\right)}{Rv_i^{n+1}\left(\rho\hat{C}_p\right)_i^{n}}U_T\right]T_{I,i}^{n+1}+\frac{1}{v_i^{n+1}\Delta t}T_i^{n}\\
&\left.-\frac{1}{\left(\rho\hat{C}_p\right)_i^{n}}\frac{p_i^{n+1}-p_{i-1}^{n+1}}{\Delta z_{i-1/2}}-\frac{\left(g\sin\theta\right)_i}{\hat{C}_{p\,i}^{\;n}}\right\}
\end{aligned}\tag{A-6}$$

APPENDIX B

Derivation of Fracture/Formation Flow Model

Because of symmetry, only a quadrant of the flow domain is considered. Assuming the linear flow exists in the reservoir and fracture system, the flow equation with dimensionless variables in the outer formation is:

$$\frac{\partial^2 p_{OD}}{\partial x_D^2} = \frac{1}{\eta_{OD}} \frac{\partial p_{OD}}{\partial t_D} \tag{B-1}$$

In Laplace domain '*l*', **Eq. B-1** can be written as

$$\frac{\partial^2 \bar{p}_{OD}}{\partial x_D^2} - \frac{l}{\eta_{OD}} \bar{p}_{OD} = 0 \tag{B-2}$$

The general solution of **Eq. B-2** is given by

$$\bar{p}_{OD} = A\exp\left(-\sqrt{\frac{l}{\eta_{OD}}} x_D \right) + B\exp\left(\sqrt{\frac{l}{\eta_{OD}}} x_D \right) \tag{B-3}$$

The outer boundary condition is constant reservoir pressure at x_e. In shale gas reservoirs, the effect of the outer boundary will not be felt during the long-term production because of long transient period. The outer boundary can be given as

$$\bar{p}_{OD}\Big|_{x_D = x_{eD}} = 0 \tag{B-4}$$

Solving for *B* yields

$$B = -A\exp\left(-2\sqrt{\frac{l}{\eta_{OD}}} x_{eD} \right) \tag{B-5}$$

At the inner boundary of the outer formation, the pressure of the inner and outer formation is equal, which is

$$\bar{p}_{OD}\Big|_{x_D=1} = \bar{p}_{ID}\Big|_{x_D=1} \tag{B-6}$$

$$A\exp\left(-\sqrt{\frac{l}{\eta_{OD}}}\right) - A\exp\left(-2\sqrt{\frac{l}{\eta_{OD}}}x_{eD}\right)\exp\left(\sqrt{\frac{l}{\eta_{OD}}}\right) = \bar{p}_{ID}\Big|_{x_D=1} \tag{B-7}$$

$$A = \frac{\bar{p}_{ID}\Big|_{x_D=1}}{\exp\left(\sqrt{\frac{l}{\eta_{OD}}}\right)\left[1-\exp\left(-2\sqrt{\frac{l}{\eta_{OD}}}x_{eD}\right)\right]} \tag{B-8}$$

Substituting **Eqs. B-8** and **B-5** into **Eq. B-3**

$$\begin{aligned}\bar{p}_{OD} = &\frac{\bar{p}_{ID}\Big|_{x_D=1}}{\exp\left(\sqrt{\frac{l}{\eta_{OD}}}\right)\left[1-\exp\left(-2\sqrt{\frac{l}{\eta_{OD}}}x_{eD}\right)\right]}\exp\left(-\sqrt{\frac{l}{\eta_{OD}}}x_D\right)\\ &-\frac{\bar{p}_{ID}\Big|_{x_D=1}}{\exp\left(\sqrt{\frac{l}{\eta_{OD}}}\right)\left[\exp\left(2\sqrt{\frac{l}{\eta_{OD}}}x_{eD}\right)-1\right]}\exp\left(\sqrt{\frac{l}{\eta_{OD}}}x_D\right)\end{aligned} \tag{B-9}$$

Considering $x_{eD} \to \infty$, we have the pressure solution for the outer formation

$$\bar{p}_{OD} = \bar{p}_{ID}\Big|_{x_D=1}\exp\left(-\sqrt{\frac{l}{\eta_{OD}}}(x_D-1)\right) \tag{B-10}$$

The inner formation solution starts from

$$\frac{\partial^2 p_I}{\partial x^2} + \frac{\partial^2 p_I}{\partial y^2} = \frac{1}{\eta}\frac{\partial p_I}{\partial t} \tag{B-11}$$

Integrating both sides of **Eq. B-11** as follows

$$\int_0^{x_f}\frac{\partial^2 p_I}{\partial x^2}dx + \int_0^{x_f}\frac{\partial^2 p_I}{\partial y^2}dx = \frac{1}{\eta}\int_0^{x_f}\frac{\partial p_I}{\partial t}dx \tag{B-12}$$

The second term in LHS and the term in RHS is not a function of *x*, results in

$$\frac{1}{x_f}\frac{\partial p_I}{\partial x}+\frac{\partial^2 p_I}{\partial y^2}=\frac{1}{\eta}\frac{\partial p_I}{\partial t} \tag{B-13}$$

Because of the continuity of flux at the boundary of the inner and outer formation, we have

$$kh\frac{\partial p_I}{\partial x}\bigg|_{x=x_f}=k_O h\frac{\partial p_O}{\partial x}\bigg|_{x=x_f} \tag{B-14}$$

Thus **Eq. B-13** can be modified as

$$\frac{\partial^2 p_I}{\partial y^2}+\frac{k_O}{kx_f}\frac{\partial p_O}{\partial x}\bigg|_{x=x_f}=\frac{1}{\eta}\frac{\partial p_I}{\partial t} \tag{B-15}$$

Converting the above equation into dimensionless form and simplifying, we have

$$\frac{\partial^2 p_{ID}}{\partial y_D^2}+\frac{k_O}{k}\frac{\partial p_{OD}}{\partial x_D}\bigg|_{x_D=1}=\frac{\partial p_{ID}}{\partial t_D} \tag{B-16}$$

In Laplace domain, it can be written as

$$\frac{\partial^2 \bar{p}_{ID}}{\partial y_D^2}+\frac{k_O}{k}\frac{\partial \bar{p}_{OD}}{\partial x_D}\bigg|_{x_D=1}-l\bar{p}_{ID}=0 \tag{B-17}$$

Assuming that the pressure gradient in *x* direction is quiet small compared with it in *y* direction in inner formation, which means the pressure has a weak *x* dependence in inner formation. From **Eq. B-10**, we can get the pressure derivative which connect the outer formation to the inner formation,

$$\frac{\partial \bar{p}_{OD}}{\partial x_D}\bigg|_{x_D=1}=-\sqrt{\frac{l}{\eta_{OD}}}\bar{p}_{ID}\big|_{x_D=1} \tag{B-18}$$

Substituting **Eq. B-18** into **Eq. B-17**, we have

$$\frac{\partial^2 \bar{p}_{ID}}{\partial y_D^2}-\left(\frac{k_O}{k}\sqrt{\frac{l}{\eta_{OD}}}+l\right)\bar{p}_{ID}=0 \tag{B-19}$$

Defining

$$\alpha_o = \frac{k_O}{k}\sqrt{\frac{l}{\eta_{OD}}} + l \tag{B-20}$$

Thus **Eq. B-19** can be simplified as

$$\frac{\partial^2 \bar{p}_{ID}}{\partial y_D^2} - \alpha_o \bar{p}_{ID} = 0 \tag{B-21}$$

The general solution for **Eq. B-21** is given by

$$\bar{p}_{ID} = A\exp\left(-\sqrt{\alpha_o}\, y_D\right) + B\exp\left(\sqrt{\alpha_o}\, y_D\right) \tag{B-22}$$

Considering the outer boundary condition

$$\bar{p}_{ID}\Big|_{y_D \to \infty} = 0 \tag{B-23}$$

Solving for B yields

$$B = 0 \tag{B-24}$$

Considering skin factor *S* in the inner formation, the inner boundary of the outer formation, the pressure of the inner and outer formation is equal, which is

$$\bar{p}_{ID}\Big|_{y_D=0} = \bar{p}_{FD}\Big|_{y_D=0} \tag{B-25}$$

Solving for *A* yields

$$A = \bar{p}_{FD}\Big|_{y_D=0} \tag{B-26}$$

The solution for **Eq. B-22** is

$$\bar{p}_{ID} = \bar{p}_{FD}\Big|_{y_D=0} \exp\left(-\sqrt{\alpha_O}\, y_D\right) \tag{B-27}$$

The solution for the inner reservoir can be solved by **Eq. B-27**. The properties of inner and outer formation are carried in the definition of α_o.

In fracture, the diffusion equation is

$$\frac{\partial^2 p_F}{\partial x^2}+\frac{\partial^2 p_F}{\partial y^2}=\frac{1}{\eta_F}\frac{\partial p_F}{\partial t} \tag{B-28}$$

The flow from formation to fracture is in the *y*-direction, and flow along fracture is in x-direction. Integrating both side of the above equation,

$$\int_0^{w/2}\frac{\partial^2 p_F}{\partial x^2}dy+\int_0^{w/2}\frac{\partial^2 p_F}{\partial y^2}dy=\frac{1}{\eta_F}\int_0^{w/2}\frac{\partial p_F}{\partial t}dy \tag{B-29}$$

The first term in LHS and the term in RHS are not a function of y, results in

$$\frac{\partial^2 p_F}{\partial x^2}+\frac{2}{w}\frac{\partial p_F}{\partial y}\bigg|_{y=w/2}=\frac{1}{\eta_F}\frac{\partial p_F}{\partial t} \tag{B-30}$$

Because of the continuity of flux at the boundary of fracture and formation, we have

$$k_F h\frac{\partial p_F}{\partial y}\bigg|_{y=w/2}=kh\frac{\partial p_I}{\partial y}\bigg|_{y=w/2} \tag{B-31}$$

The governing equation becomes

$$\frac{\partial^2 p_F}{\partial x^2}+\frac{2}{w}\frac{k}{k_F}\frac{\partial p_I}{\partial y}\bigg|_{y=w/2}=\frac{1}{\eta_F}\frac{\partial p_F}{\partial t} \tag{B-32}$$

Converting the above equation into dimensionless form, we have

$$\frac{\partial^2 p_{FD}}{\partial x_D^2}+\frac{2}{w}\frac{kx_F}{k_F}\frac{\partial p_{ID}}{\partial y_D}\bigg|_{y_D=w_D/2}=\frac{1}{\eta_{FD}}\frac{\partial p_{FD}}{\partial t_D} \tag{B-33}$$

Substituting **Eq. 2.46** the definition of dimensionless fracture conductivity, we have

$$\frac{\partial^2 p_{FD}}{\partial x_D^2}+\frac{2}{F_{CD}}\frac{\partial p_{ID}}{\partial y_D}\bigg|_{y_D=w_D/2}=\frac{1}{\eta_{FD}}\frac{\partial p_{FD}}{\partial t_D} \tag{B-34}$$

Recalling the solution for the linear flow in formation **Eq. B-27**, and taking the derivative of the solution, we get

$$\frac{\partial p_{ID}}{\partial y_D}=-\sqrt{\alpha_o}\,p_{FD}\exp\left(-\sqrt{\alpha_o}\,y_D\right) \tag{B-35}$$

Assuming that $y_D = w_D/2 \approx 0$, we have

$$\left.\frac{\partial p_{ID}}{\partial y_D}\right|_{y_D=0} = -\sqrt{\alpha_o}\, p_{FD} \tag{B-36}$$

Substituting the above equation into **Eq. B-34**, the equation can be written as

$$\frac{\partial^2 p_{FD}}{\partial x_D^2} - \frac{2\sqrt{\alpha_o}}{F_{CD}} p_{FD} = \frac{1}{\eta_{FD}} \frac{\partial p_{FD}}{\partial t_D} \tag{B-37}$$

In Laplace domain, the equation is

$$\frac{\partial^2 \bar{p}_{FD}}{\partial x_D^2} - \left(\frac{2\sqrt{\alpha_o}}{F_{CD}} + \frac{l}{\eta_{FD}} \right) \bar{p}_{FD} = 0 \tag{B-38}$$

Defining

$$\alpha_F = \frac{2\sqrt{\alpha_o}}{F_{CD}} + \frac{l}{\eta_{FD}} \tag{B-39}$$

Then **Eq. B-38** can be simplified as

$$\frac{\partial^2 \bar{p}_{FD}}{\partial x_D^2} - \alpha_F \bar{p}_{FD} = 0 \tag{B-40}$$

The general solution for **Eq. B-40** is

$$\bar{p}_{FD} = A \exp\left(-\sqrt{\alpha_F}\, x_D\right) + B \exp\left(\sqrt{\alpha_F}\, x_D\right) \tag{B-41}$$

The outer boundary condition is no-flow at the fracture tip, we have

$$\left.\frac{\partial p_{FD}}{\partial x_D}\right|_{x_D=1} = -\sqrt{\alpha_F} A \exp\left(-\sqrt{\alpha_F}\, x_D\right) + \sqrt{\alpha_F} B \exp\left(\sqrt{\alpha_F}\, x_D\right) = 0 \tag{B-42}$$

Solving the above equation yields

$$A = B \exp\left(2\sqrt{\alpha_F}\right) \tag{B-43}$$

So we have

$$\bar{p}_{FD} = B \exp\left[\sqrt{\alpha_F}\left(2 - x_D\right)\right] + B \exp\left(\sqrt{\alpha_F}\, x_D\right) \tag{B-44}$$

The coefficient *B* can be determined by inner boundary condition for the fracture. The volumetric velocity crossing the wellbore surface from fracture is given by Darcy's law

$$v_x = -\frac{k_F}{\mu}\frac{\partial p_F}{\partial x}\bigg|_{x=0} \tag{B-45}$$

Flow rate passing through the wellbore surface can be calculated by evaluating the surface integral as follows

$$\int_0^{w/2}\int_0^{h/2} v_x\,dzdy = -\frac{k_F}{\mu}\int_0^{w/2}\int_0^{h/2}\frac{\partial p_F}{\partial x}\bigg|_{x=0} dzdy \tag{B-46}$$

Because the total flow rate crossing the wellbore surface is the sum of the flux coming from both sides of the rectangular-shaped fracture, and only one-quarter of the fracture is modeled due to the symmetry. The above equation can be related to flow rate *q* as follows

$$\frac{q}{8} = -\frac{k_F}{\mu}\frac{w}{2}\frac{h}{2}\frac{\partial p_F}{\partial x}\bigg|_{x=0} \tag{B-47}$$

Converting the above equation into dimensionless form, and recalling the definition of dimensionless conductivity, it can be written as

$$1 = -\frac{k_F w}{\pi k x_F}\frac{\partial p_{FD}}{\partial x_D}\bigg|_{x_D=0} \tag{B-48}$$

Substituting the definition of dimensionless fracture conductivity, we have

$$\frac{\partial p_{FD}}{\partial x_D}\bigg|_{x_D=0} = -\frac{\pi}{F_{CD}} \tag{B-49}$$

Applying Laplace transform to the above equation, we have the constant flow rate inner boundary condition for hydraulic fracture.

$$\left.\frac{\partial \bar{p}_{FD}}{\partial x_D}\right|_{x_D=0} = -\frac{\pi}{lF_{CD}} \tag{B-50}$$

Then solving the coefficient *B* we get

$$B = -\frac{\pi}{lF_{CD}\sqrt{\alpha_F}\left[1-\exp\left(2\sqrt{\alpha_F}\right)\right]} \tag{B-51}$$

Also we get *A* from **Eq. B-43**

$$A = B\exp\left(2\sqrt{\alpha_F}\right) = -\frac{\pi\exp\left(2\sqrt{\alpha_F}\right)}{lF_{CD}\sqrt{\alpha_F}\left[1-\exp\left(2\sqrt{\alpha_F}\right)\right]} \tag{B-52}$$

Substituting *A* and *B* into the general solution and rearranging we have

$$\bar{p}_{FD} = \frac{\pi}{lF_{CD}\sqrt{\alpha_F}}\frac{\cosh\left[\sqrt{\alpha_F}\left(1-x_D\right)\right]}{\sinh\left(\sqrt{\alpha_F}\right)} \tag{B-53}$$

The wellbore pressure can be solved as

$$\bar{p}_{wD} = \bar{p}_{FD}\Big|_{x_D=0} = \frac{\pi}{lF_{CD}\sqrt{\alpha_F}\tanh\left(\sqrt{\alpha_F}\right)} \tag{B-54}$$

For constant pressure at the bottomhole, the flow rate is:

$$\bar{q}_D(l) = \frac{1}{l^2\bar{p}_{wD}(l)} \tag{B-55}$$

Similarly, the pressure distribution inside fracture can be expressed as:

$$\bar{p}_{FD} = \frac{1}{l}\cosh(\sqrt{\alpha_F}(1-x_D))/\cosh\sqrt{\alpha_F} \tag{B-56}$$

APPENDIX C

Finite Difference Equation for Reservoir Thermal Model

To illustrate the finite difference procedure in reservoir, we use the inner formation equation **Eq. 2.57** as an example. The accumulation terms at the left-hand side are approximated by backward difference, and the derivatives at the right-hand side are using central differences.

The thermal equation in the inner formation is

$$\overline{\rho\hat{C}_p}\frac{\partial T}{\partial t}-\phi\beta T\frac{\partial p}{\partial t}=\frac{k\rho\hat{C}_p}{\mu}\frac{\partial p}{\partial y}\frac{\partial T}{\partial y}-\frac{(\beta T-1)}{\mu}k\left(\frac{\partial p}{\partial y}\right)^2+K_T\left(\frac{\partial^2 T}{\partial x^2}+\frac{\partial^2 T}{\partial y^2}\right) \tag{C-1}$$

The discretization of the terms are

$$\frac{\partial T}{\partial t}=\frac{T_{i,j}^{n+1}-T_{i,j}^{n}}{\Delta t} \tag{C-2}$$

$$\frac{\partial p}{\partial t}=\frac{p_{i,j}^{n+1}-p_{i,j}^{n}}{\Delta t} \tag{C-3}$$

$$\frac{\partial^2 T}{\partial x^2}=\frac{T_{i+1,j}^{n+1}-2T_{i,j}^{n+1}+T_{i-1,j}^{n+1}}{\Delta x^2} \tag{C-4}$$

$$\frac{\partial^2 T}{\partial y^2}=\frac{T_{i,j+1}^{n+1}-2T_{i,j}^{n+1}+T_{i,j-1}^{n+1}}{\Delta y^2} \tag{C-5}$$

$$\frac{\partial T}{\partial y}=\frac{T_{i,j+1}^{n+1}-T_{i,j-1}^{n+1}}{2\Delta y} \tag{C-6}$$

$$\frac{\partial p}{\partial y}=\frac{p_{i,j+1}^{n+1}-p_{i,j-1}^{n+1}}{2\Delta y} \tag{C-7}$$

where *i, j* denote the grid number and *n* denotes the time step.

Therefore, the discretized reservoir thermal equation is shown as

$$a_S T_{i-1,j}^{n+1} + a_W T_{i,j-1}^{n+1} + a_C T_{i,j}^{n+1} + a_N T_{i+1,j}^{n+1} + a_E T_{i,j+1}^{n+1} = a_F \tag{C-8}$$

where the coefficients are given by

$$a_W = \frac{K_T}{(\Delta y)^2} - \frac{k\rho\hat{C}_p}{4\mu(\Delta y)^2}\left(p_{i,j+1}^{n+1} - p_{i,j-1}^{n+1}\right) \tag{C-9}$$

$$a_S = \frac{K_T}{(\Delta x)^2} \tag{C-10}$$

$$a_C = -\frac{\overline{\rho\hat{C}_p}}{\Delta t} + \frac{\phi\beta}{\Delta t}\left(p_{i,j}^{n+1} - p_{i,j}^{n}\right) - \frac{k\beta\left(p_{i,j+1}^{n+1} - p_{i,j-1}^{n+1}\right)^2}{4\mu(\Delta y)^2} - \frac{2K_T}{(\Delta y)^2} - \frac{2K_T}{(\Delta x)^2} \tag{C-11}$$

$$a_N = \frac{K_T}{(\Delta x)^2} \tag{C-12}$$

$$a_E = \frac{K_T}{(\Delta y)^2} + \frac{k\rho\hat{C}_p}{4\mu(\Delta y)^2}\left(p_{i,j+1}^{n+1} - p_{i,j-1}^{n+1}\right) \tag{C-13}$$

$$a_F = -\frac{\overline{\rho\hat{C}_p}}{\Delta t} T_{i,j}^{n} + \frac{k}{4\mu(\Delta y)^2}\left(p_{i,j+1}^{n+1} - p_{i,j-1}^{n+1}\right)^2 \tag{C-14}$$

The initial and boundary conditions are as follows:

$$T_{i,j}^{0} = T_i \text{ at } t = 0 \tag{C-15}$$

$$T_{I,j}^{n+1} = T_O^{n+1} \text{ at } i = I \tag{C-16}$$

$$T_{i,J}^{n+1} = T_{i,J-1}^{n+1} \text{ at } j = J \tag{C-17}$$

$$T_{i,0}^{n+1} = T_f^{n+1} \text{ at } j = 0 \tag{C-18}$$

$$T_{0,j}^{n+1} = \frac{K_T}{K_T + U_T\Delta x} T_{1,j}^{n+1} + \frac{U_T\Delta x}{K_T + U_T\Delta x} T_w \tag{C-19}$$

The boundary conditions couple the fracture, inner formation and outer formation as a whole and continuous system. Also if we consider the heat conduction between wellbore and inner formation, there should be some iterations in calculation. For simplicity, the inner boundary could be treated as no heat flux boundary. The initial condition is geothermal temperature inside fracture and formation. The equation is solved implicitly to reach better accuracy.

APPENDIX D

Derivation of the Eikonal Equation

Starting from the approximate solution of pressure in the frequency domain,

$$\tilde{p}(x,\omega) = A_0(x)e^{-\sqrt{-i\omega}\tau(x)} \tag{D-1}$$

We can obtain the diffusive term of pressure by calculating the first and second derivative as shown below

$$\nabla\tilde{p}(x,\omega) = \nabla A_0(x)e^{-\sqrt{-i\omega}\tau(x)} - \sqrt{-i\omega}\nabla\tau(x)A_0(x)e^{-\sqrt{-i\omega}\tau(x)} \tag{D-2}$$

$$\begin{aligned}
&\nabla\cdot k(x)\nabla\tilde{p}(x,\omega)\\
&= \nabla k(x)\nabla A_0(x)e^{-\sqrt{-i\omega}\tau(x)} + k(x)\nabla\cdot\nabla A_0(x)e^{-\sqrt{-i\omega}\tau(x)} - \sqrt{-i\omega}\nabla\tau(x)k(x)\nabla A_0(x)e^{-\sqrt{-i\omega}\tau(x)}\\
&- \sqrt{-i\omega}\nabla k(x)\nabla\tau(x)A_0(x)e^{-\sqrt{-i\omega}\tau(x)} - \sqrt{-i\omega}k(x)\nabla\cdot\nabla\tau(x)A_0(x)e^{-\sqrt{-i\omega}\tau(x)}\\
&- (i\omega)\nabla\tau(x)k(x)\nabla\tau(x)A_0(x)e^{-\sqrt{-i\omega}\tau(x)} - \sqrt{-i\omega}k(x)\nabla\tau(x)\nabla A_0(x)e^{-\sqrt{-i\omega}\tau(x)}
\end{aligned} \tag{D-3}$$

The pressure expression in the frequency domain is

$$\nabla\cdot k(x)\nabla\tilde{p}(x,\omega) + i\omega\phi(x)\mu c_t\tilde{p}(x,\omega) = 0 \tag{D-4}$$

Substituting Eqs. (D-3) and (D-1) into Eq. (D-4), and only considering the highest order in $\sqrt{-i\omega}$, which is the term contains $(i\omega)$. We have

$$-(i\omega)\left[\nabla\tau(x)k(x)\nabla\tau(x) - \phi(x)\mu c_t\right]A_0(x)e^{-\sqrt{-i\omega}\tau(x)} = 0 \tag{D-5}$$

So that

$$\nabla\tau(x)k(x)\nabla\tau(x) - \phi(x)\mu c_t = 0 \tag{D-6}$$

$$\nabla\tau(x)\frac{k(x)}{\phi(x)\mu c_t}\nabla\tau(x) = 1 \tag{D-7}$$

According to the definition of diffusivity $\alpha(x)$, we finally get

$$\sqrt{\alpha(x)}\left|\nabla\tau(x)\right| = 1 \tag{D-8}$$